ΕΘΝΙΚΟ ΜΕΤΣΟΒΙΟ ΠΟΛΥΤΕΧΝΕΙΟ - ΣΧΟΛΗ ΗΛΕΚΤΡΟΛΟΓΩΝ ΜΗΧΑΝΙΚΩΝ ΚΑΙ ΜΗΧΑΝΙΚΩΝ ΗΛΕΚΤΡΟΝΙΚΩΝ ΥΠΟΛΟΓΙΣΤΩΝ

Κατευθυνση: Ηλεκτρονικη και Συστηματα

Διπλωματικη Εργασια

Προσομοίωση του πειράματος ATLAS στο CERN με το εργαλείο λογισμικού FLUKA για την εκτίμηση της ακτινοβολίας υποβάθρου

Μαρία Μ. Καινουργιάκη

Επιβλέπων
Καθ. Ευάγγελος Γαζης

25 Ιουνίου 2018

ΕΘΝΙΚΟ ΜΕΤΣΟΒΙΟ ΠΟΛΥΤΕΧΝΕΙΟ -
ΣΧΟΛΗΗΛΕΚΤΡΟΛΟΓΩΝ ΜΗΧΑΝΙΚΩΝ ΚΑΙ
ΜΗΧΑΝΙΚΩΝ ΗΛΕΚΤΡΟΝΙΚΩΝ ΥΠΟΛΟΓΙΣΤΩΝ

Κατευθυνση: Ηλεκτρονικη και Συστηματα

Διπλωματικη Εργασια

Προσομοίωση του πειράματος **ATLAS** στο **CERN** με το εργαλείο λογισμικού **FLUKA** για την εκτίμηση της ακτινοβολίας υποβάθρου

Μαρία Μ. Καινουργιάκη

Επιβλέπων
Καθ. Ευάγγελος Γαζης
Επιτροπή:

. . . .

Καθ. Ευάγγελος Γαζης   Καθ. Ηλίας Γλυτσης   Καθ. Ιωάννης Π. Ξανθακης

25 Ιουνίου 2018

. . . .

Μαρία Μ. Καινουργιάκη
Διπλωματούχος Ηλεκτρολόγος Μηχανικός και Μηχανικός Ηλεκτρονικών Υπολογιστών, Ε.Μ.Π.

National Techical University of Athens - School of Electrical and Computer Engineering

Consentration Field: Electronics and Systems

Diploma Thesis

A FLUKA Simulation of the ATLAS Experiment at CERN for Background Radiation Estimation

Maria M. Kainourgiaki

supervised by
Prof. Evangelos Gazis

Monday 25^{th} June, 2018

National Techical University of Athens - School of Electrical and Computer Engineering

Consentration Field: Electronics and Systems

Diploma Thesis

A FLUKA Simulation of the ATLAS Experiment at CERN for Background Radiation Estimation

Maria M. Kainourgiaki

supervised by
Prof. Evangelos Gazis
Committee:

....	....	....
Prof. Evangelos Gazis	Prof. Elias Glytsis	Prof. John P. Xanthakis

Monday 25th June, 2018

. . . .

Maria M. Kainourgiaki
Electrical and Computer Engineer N.T.U.A.

Abstract

Particle interactions at very high energies result in large quantities of radiation emission. This may have negative effects on the detector's materials and electronics as well as on the data signals and create a hostile radiation environment for the personnel working in the detector regions after an experiment run. To limit the background radiation, after excessive study, a shielding layout was designed.

In this thesis an estimation of the radiation background at the ATLAS experiment is attempted. A simplified design of the ATLAS detector at the LHC at CERN was created and the conditions of an experiment run were simulated using the Monte Carlo simulation tool, FLUKA.

Keywords

Detector, Elementary Particles, ATLAS, FLUKA, Radiation Background, Monte Carlo

Περίληψη

Οι αλληλεπιδράσεις σωματιδίων υψηλών ενεργειών έχουν σαν αποτέλεσμα την εκπομπή μεγάλων ποσοτήτων ακτινοβολίας. Η ακτινοβολία αυτή έχει επιδρά αρνητικά στα υλικά και τις ηλεκτρονικές διατάξεις του ανιχνευτή, μπορεί να προκαλέσει αλλοίωση των σημάτων των διάφορων ανιχνευτικών διατάξεων και να καταστήσει το περιβάλλον εργασίας επικίνδυνο για το ανθρώπινο δυναμικό που εργάζεται στον ανιχνευτή. Περιορισμός των αρνητικών συνεπειών αυτών συνεπειών επιτυγχάνεται με προσθήκη τμημάτων θωράκισης, στον ανιχνευτή, τα οποία μειώνουν τα επίπεδα ακτινοβολίας.

Στην παρούσα διπλωματική εργασία παρουσιάζεται ο σχεδιασμός μιας προσομοίωσης του πειράματος ATLAS στο CERN, με χρήση των εργαλείων λογισμικού FLUKA και flair.

Λέξεις Κλειδιά

Ανιχνευτής, ATLAS, Στοιχειώδη Σωματίδια, FLUKA, Ακτινοβολία Υποβάθρου, Monte Carlo

Acknowledgements

First I would like to thank my family, my biggest fans in my life so far. Their help and support, whether it was driving to and from classes or helping me with subjects, has been invaluable and I deeply appreciate every single gesture.

To my father who has been and continues being my teacher and coach: you introduced and guided me into the scientific world, teaching me countless hours and persisting even when I did not seem thankful, providing me with knowledge and moral support. And to my mother: your spiritual support and your example made me want to follow my dreams and become a better person. I love you both and thank you deeply.

I would also like to express my respect and gratitude to my supervisor, Prof. E. Gazis for his support, patience and valuable help and insight for the past years throughout my studies and thesis preparation.

My teachers and professors at the N.T.U.A. for sharing their knowledge and being patient, available and willing to help. And my thesis committee for their time and helpful insight.

Last but not the least many thanks to my friends and my lab partner(s). All-nighters studying before deadlines and exams are better when you share the load and I could not imagine anyone better to share it with! Thank you!

Contents

List of Tables

List of Figures

Chapter 1

Fundamental Constituents of Matter and Interactions

Matter consists of molecules and molecules are made of atoms. Atoms are held together by chemical bonds. Bond mechanisms are mainly due to electromagnetic interactions between the atoms or ions that make up a chemical compound. The molecule is a more stable state of matter than individual atoms, because the energy of the system is lower. Each atom is made of subatomic particles, protons, neutrons and electrons, which are formed by groups of elementary particles.

Matter constituents, in the quarks/leptons level, interact with each other via the strong/weak interactions that exist in nature. They are combined in such a way that the final potential energy of the system is the lowest possible.

1.1 The Atom

The atom is made of a positively charged nucleus, which has a vary small size, of the order of 10^{-14} m inside an electron cloud that is negatively charged and has a size of the order of 10^{-10} m. The electron is an elementary particle, this means it has no internal structure and is considered to have no size. The nucleus contains protons and neutrons and since it has internal structure it is not an elementary particle. Protons and neutrons are not elementary either, they contain quarks that stay bound together via the strong interaction. As far as physics goes today, quarks are elementary in the same sense as electrons are.

1.1.1 The Nucleus

The atomic nucleus contains positively charged protons, with charge +1, with respect to the elementary charge, and neutral neutrons, both of them are referred to as nucleons. The masses of the two types of nucleons is almost equal. To identify a nucleus two numbers are used, the mass number A that is the total number of nucleons, and the atomic number Z that is the number of protons in the nucleus. Sometimes it is useful to use the number of neutrons N. The atomic nucleus of an element X is symbolized as ${}^{A}_{Z}X$. The charge of the nucleus is equal to $+Ze$, where e the elementary charge (absolute value of the charge of an electron). Nuclides that have the same Z are called isotopes, those with the same A are called isobars and those with the same N are isotones.

Protons are positively charged particles and stay bound in the nucleus very close with other protons so they repulse each other strongly due to the electromagnetic force. So another kind of force, much stronger than the electrostatic force, has to be applied to keep the nucleons inside the nucleus. This interaction called strong has very short range ($< 10^{-14}$). It is also completely independent of the nucleon's charge.

The sum of the masses of the nucleons that construct a nucleus is larger than the actual mass of the nucleus. This difference exists due to the fact that the forces that bind the nucleons contribute in the total mass and is called mass deficit ΔM.

$$\Delta M = M(A, Z) - (ZM_p + NM_n).$$

where M_p the proton mass and M_n the neutron mass. The energy that corresponds to the mass difference is the binding energy B of the nucleus and is negative:

$$B = -\Delta M c^2$$

The total energy of the system of individual nucleons is higher than that of the (stable) nuclei system, so to split the nucleus to its constituents additional energy, the nuclear binding energy, must be offered to the system.

As nuclei become heavier the binding energy per nucleon decreases, this causes them to be unstable and thus decay spontaneously. This nuclear process is called radioactive decay. There are three types of radioactive decays, alpha, beta and gamma decay.

- In alpha decay the nucleus produces a helium nucleus, consisting of two protons and two neutrons, the alpha particle.

- There are two kinds of beta decay depending on the charge of the emitted beta particle, β^- decay to an electron ($\beta^- particle$) and an electron antineutrino, β^+ decay to a positron ($\beta^+ particle$) and an electron neutrino. The presence of the electron neutrino or its antiparticle is necessary for the energy and momentum conservation.

Radioactive Decay	Chemical equation
Alpha Decay αDecay	${}^{A}_{Z}X \rightarrow {}^{A-4}_{Z-2}Y + {}^{4}_{2}He$
Beta Decay β^{+}Decay	${}^{A}_{Z}X \rightarrow {}^{A}_{Z-1}Y + \beta^{+} + v_e$
Beta Decay β^{-}Decay	${}^{A}_{Z}X \rightarrow {}^{A}_{Z+1}Y + \beta^{-} + \bar{v}_e$
Gamma Decay γDecay	${}^{A}_{Z}X^{*} \rightarrow {}^{A}_{Z}X + \gamma$

Table 1.1: The Radioactive Decays

- Usually after a radioactive decay takes place, the product nucleus is in excited energy state. Then, it is de-excited to lower energy state, emitting photon(s) with energy equal to the difference between the energies of the final and the initial state. The photons emitted from such decays are called gamma rays, having various energies.

Table 1.1 shows all the radioactive decays. In gamma decay ${}^{A}_{Z}X^{*}$ symbolizes an excited nucleus and γ particle the photon. Table 1.1 shows all the radioactive decays. In gamma decay ${}^{A}_{Z}X^{*}$ symbolizes an excited nucleus and γ particle the photon.

1.1.2 The electron cloud

The atom's electrons fill the space around the nucleus. The position of each electron cannot be predicted but the possibility for an electron to be at a specific place can be calculated. Each electron is characterized by a set of quantum numbers and according to the Pauli exclusion principle two electrons in the same atom cannot have identical sets of quantum numbers.

1.2 Interactions

There are only four types of interactions in nature the strong, the electromagnetic, the weak and the gravitational interaction. All physical phenomena happen due to the action of the above. An interaction can cause a particle to change type, and/or changes in its momentum and energy. Also an interaction on a lone particle can cause spontaneous state transitions. According to quantum mechanical interactions, they are transmitted by the exchange of field carriers. These particles are called gauge bosons.

Interaction	Acts on	Relative Strength	Range	Field Particle (Boson)
Strong	Quarks and particles containing quarks	1	Small ($\approx$10 fm)	Gluon (g)
Electromagnetic	Electrically charged particles	10^{-2}	Large ($\infty, \propto {}^1/_{r^2}$)	Photon (γ)
Weak	All particles	10^{-9}	Small ($\approx 10^{-2}$ fm)	$W^{\pm}$, Z bosons
Gravitational	All particles	10^{-38}	Large $\infty, \propto {}^1/_{r^2}$	Graviton

Table 1.2: Interactions of Matter.

1.2.1 The Strong Interaction

The strong interaction is applied among the quarks of the nucleons; it, also, is responsible for keeping protons and neutrons bound together in the nucleus. It has a very small range that does not extend beyond the radius of the nucleus. It is stronger than the other interactions, if it was not then the Coulomb repulsion between protons would break the nucleus.

In order to interact via the strong interaction, quarks need to have colour charge. This type of charge has three components red (R), green (G) and blue (B). There are also the respective antiparticle colour charges, antired ($\bar{R}$), antigreen ($\bar{G}$) and antiblue ($\bar{B}$). When particles have the same colour charge they repulse, while particles of different or complementary colour charges attract. An important property strong interactions is that they are flavour independent. This means that strong interactions are identical for all particles that carry colour charge.

The gauge bosons mediating these interactions are the gluons, g. They have zero mass, zero electric charge and unitary spin. They also carry colour charge that is the combination of one colour and one anticolour component.

1.2.2 The Electromagnetic Interaction

The electromagnetic interaction is responsible for forming atoms and molecules. Its strength acts even through large distances and is reversely proportional to the distance between the particles that interact. It is about 100 times weaker than the strong interaction.

To interact via electromagnetic interaction particles need to be charged electrically. There are two types of electrical charge, psotove (+) and negative (-). Particles with like charges repel while those with opposite charges attract.

The gauge bosons mediating these interactions are the photons γ. They are massless, spin-1 and electrically neutral particles.

1.2.3 The Weak Interaction

The weak interaction is a nuclear interaction with small range. It is responsible for most of the radioactive decay processes and makes some nuclei unstable. It is about 10^9 times weaker than the strong interaction. Scientists believe that E/M and weak interactions might be two different forms of the same interaction, the electroweak interaction.

The charge connected with this interaction is the weak charge that has two components, the total length (T) and the $3^($rd) component of the particle's weak isospin. A particle has to have nonzero weak isospin in order to emit or absorb a weak interaction's gauge boson.

There are three gauge bosons that mediate the weak interactions,$W^{\pm}$ and Z bosons. The Z boson is electrically neutral, so sometimes the symbol Z^0 is used and has mass $91.188\,{}^{GeV}\!/_{c^2}$. The W^- and W^+ bosons have -1 and +1 electrical charges respectively (with respect to the elementary charge) and both their mass is $80.39\,{}^{GeV}\!/_{c^2}$.

1.2.4 The Gravitational Interaction

The gravitational force, like the E/M interaction acts even through large distances and is reversely proportional to the distance between the bodies that interact. It keeps the galaxies and planetary systems in the state that they are and is responsible for the movement of the planets. It is much weaker than the strong interaction, about 10^{38} times weaker, and can be neglected when studying elementary particles and their interactions.

The graviton, G, is theorised to be the force carrier for the gravitational interaction. Its existence has not yet been proved. It is expected to have zero mass, and be an electrically neutral and spin-2 particle.

1.3 Elementary Particles

Elementary is a particle that has no internal structure. According to the current theory, the Standard Model(SM), all ordinary matter, consists of only two types of particles, quarks and leptons, for each particle there is one antiparticle. In the standard model, elementary particles are assigned to three generations.

1.3.1 Leptons

Leptons are elementary particles of semi integer spin (1/2). There are six known leptons and by pairs they are assigned to the three generations of matter as shown in table 1.3. Each generation has one lepton, with charge -1 (with respect to to electron charge) and one neutral lepton neutrino. In the first generation belong the electron and the electron neutrino, in the second the muon (mu lepton or mu) and the muon neutrino and in the third the tauon (tau lepton or tau) and the the tau neutrino. For each one of them there is a corresponding antiparticle.

Leptons only take part in weak (all of them) and electromagnetic (only the charged ones) interactions. The fact that neutrinos only interact via weak interactions and have very small masses make them very difficult to detect.

One additional quantum number that is used to describe leptons is the lepton number, and it has three components, the electron number (L_e), the muon number (L_μ) and the tau number (L_τ). The value of these numbers for each of the leptons is shown in table 1.4. For all particles other than leptons, lepton numbers are zero.

1.3.2 Quarks

Quarks are also semi integer spin particles. As far as we know there are six distinct types (flavours) of quarks, up(u), down(d), charm(c), strange(s), top(t) and bottom(b). They have no size (point-like particles) and carry fractional electric charge (with respect to the elementary electric charge). Their assignment to generations is as shown in table 1.3, so each generation contains two quarks, one with $+\frac{2}{3}$ charge and one with $-frac13$. In common matter, that is made of protons and neutrons, only quarks of the first generation, i.e. up and down, are present.

So far there has been no observation of free quarks in nature. Because of their colour charge they interact with one another via strong interaction, so they stay in very stable bound states, the hadrons, this is called confinement. Each quark can only carry one type of colour charge. Also there are the corresponding antiparticles, the antiquarks.

Additional quantum numbers for quarks are associated with s, c, b and t quarks, are respectively strangeness, charm, beauty and top. There are also the six quark numbers, which are defined as follows, N_f is the f flavour quark number, $N(f)$ is the number of particles of flavour f and $N(\bar{f})$ the number of antiparticles of flavour f:

$$N_f \equiv N(f) - N(\bar{f}), \text{ where } f = u,\ d,\ s,\ c,\ b,\ t$$

and the total number of quarks:

Generation	Leptons	Quarks
1st	e^- Electron	u up
	v_e Electron neutrino	d down
2nd	μ^- Muon	c charm
	v_μ Muon neutrino	s strange
3rd	τ^- Tau	t top
	v_τ Tau neutrino	b bottom

Table 1.3: Elementary Particles and Generations of Matter

Particle	Antiparticle	Rest Mass (MeV/c^2)	Electic Charge	(L_e)	(L_μ)	(L_τ)	Lifetime(s)	Major Decays
e^- Electron	e^+ Positron	0.511	-1	+1	0	0	Stable	-
v_e Electron neutrino	$\bar{v}_e$	0(?)	0	+1	0	0	Stable	-
μ^- Muon	μ^+	105.7	-1	0	+1	0	2.197×10^{-6}	$e^-\bar{v}_e v_\mu$
v_μ Muon neutrino	$\bar{v}_\mu$	0(?)	0	0	+1	0	Stable	-
τ^- Tau	τ^+	1777.0	-1	0	0	+1	2.906×10^{-13}	$\mu^-\bar{v}_\mu v_\tau, e^-\bar{v}_e v_\tau$
v_τ Tau neutrino	$\bar{v}_\tau$	0(?)	0	0	0	+1	Stable	-

Table 1.4: Leptons and their properties. All leptons have $\frac{1}{2}$ spin. The electric charge is given with respect to the elementary charge ($1.6021766208(98) \times 10^{-19} Coulomb$). The symbolism in "Major Decays" column is described by the following example: in the third row $e^-\bar{v}_e v_\mu$ means that the decy mechanism of the muon is $\mu^- \to e^- + \bar{v}_e + v_\mu$.

$$N_q \equiv N(q) - N(\bar{q})$$

where $N(q)$ the total number of quarks and $N(\bar{q})$ the total number of antiquarks. The quark numbers as well as the total quark number are characteristic quantum numbers not only for individual quarks but for quark systems as well. Table 1.5 contains some of the quarks' properties.

1.4 The Standard Model

The ways elementary particles interact via electromagnetic, strong and weak interactions, and are combined to compose the universe, is described by a theory called the Standard Model (SM). According to the SM particles can be sorted into categories with respect to some of their physical properties.

One way to distinguish particle families is according to their spin, which for each type has a fixed value. Fermions are particles with half integer spin and bosons particles with integer spin. All leptons and quarks have $\frac{1}{2}$ spin so all of them, as well as particles that are an odd number combination of them, are fermions. Gauge bosons along with the Higgs boson and other particles like deuterium (^2H) are

Particle	Mass (GeV/c^2)	Lifetime (s)	Charge	Strangeness	Charm	Beauty	Truth
up (u)	0.002		$+2/3$	0	0	0	0
down (d)	0.005		$-1/3$	0	0	0	0
strange (s)	0.1	$10^{-8} - 10^{-10}$	$-1/3$	-1	0	0	0
charm (c)	1.3	$10^{-12} - 10^{-13}$	$+2/3$	0	+1	0	0
top (t)	173	10^{-25}	$+2/3$	0	0	0	+1
bottom (b)	4.2	$10^{-12} - 10^{-13}$	$-1/3$	0	0	+1	0

Table 1.5: Quarks and their properties. All quarks have $\frac{1}{2}$ spin. The electric charge is given with respect to the elementary charge ($1.6021766208(98) \times 10^{-19} Coulomb$). Antiquarks have sthe same masses and opposite electric charge, strangeness, charm, beauty and truth.

bosons.

Another classification is based on the interactions that each particle participates in. Hadrons are particles that interact via strong interaction and leptons interact via weak and electromagnetic interactions (gauge bosons and the Higgs boson do not belong in either of them). Hadrons are created by quarks that are attracted to each other because of their colour charge. The quarks must combine in such a way that the hadrons they form have integer electric charge and no colour charge (hadrons are white). Colour confinement[1] does not allow any quark combinations but only those that are described by the rule: $(3q)^p(q\bar{q})^n$, where $p, n \geq 0$. Hadrons are divided to mesons and baryons according to their mass and spin. There are no hadrons containing the top quark, because it has such a short lifetime, that it decays before it can form bound states.

Mesons are formed by a quark and an anti quark with complementary colour charges. They have integer spin (0 or 1), as they are a combination of an even number of quarks, so they belong to the category of the bosons. Their mass is greater than that of the electron but smaller the the proton mass. All mesons end up decaying to electrons, muons, neutrinos and photons.

Baryons have half integer spin ($\frac{1}{2}$ or $\frac{3}{2}$) and their mass is equal or bigger than that of the proton. Because of their spin they belong to the category of fermions. They are bound states of three quarks, each of a different colour so the final particle is colourless (white). Protons and neutrons belong to this category and all baryons (except for the proton) decay giving one proton, among other particles.

Having defined baryons another quantum number is added for quarks and hadrons,

[1]Colour confinement is the hypothesis that hadrons can only exist in states called colour singlets, that have zero values for all colour charges, while quarks, which have nonzero colour charges, can exist only confined in them.[13]

called baryon number B. This number can replace the total quark number N_q.

$$B \equiv \frac{N_q}{3} = \frac{N(q)-N(\bar{q})}{3}$$

All leptons and bosons have $B = 0$, all quarks have $B = +1/3$ and all antiquarks have $B = -1/3$.

For every particle there is an antiparticle that has the same mass and spin as the particle but all charges, the lepton number, the baryon number (so the quark numbers as well), charm, strangeness, truth and beauty are the opposite of those of the particle.

As mentioned in 1.2 particles interact by exchanging gauge bosons. For an interaction to be possible a set of rules must be obeyed.

1. Baryon number is conserved in all known interactions, as is the total quark number. So far there have been no experiments that suggest otherwise.

2. The lepton number is conserved.

3. Charges of all types (electric, colour, weak isospin) are rigorously conserved.

4. The flavour of particles is conserved by strong and electromagnetic interactions but can be altered by weak interactions. So the six quark numbers are conserved in strong and electromagnetic interactions but not necessarily in weak interactions. As a result in strong and electromagnetic interactions quarks can be created and destroyed only in particle-antiparticle pairs (quark and antiquark of the same flavour). In weak interactions only the total number of quarks must be conserved irrespective of their flavour. Thus, $N_q \equiv N(q) - N(\bar{q})$, where $N(q)$ the total number of quarks and $N(\bar{q})$ the total number of antiquarks, remains constant in all interactions.

The Higgs boson is a spin-0 particle that creates a field in which a particle gains its mass, so the movement inside a Higgs field is the origin of other particles' masses.

1.5 Issues of the Standard Model and Possible Solutions

The standard model explains particle phenomena accurately and its predictions agree very well with experimental data. Despite the fact that the theory fits with the reality, there are still observed phenomena that can not be explained by the standard model, so there is a need for additional theories that cover what the current one misses. One of the most popular ones is Super Symmetry (SUSY).

1.6 Particle Interactions with Matter

1.6.1 Neutral Particles in Matter

Neutrons

Neutrons are electrically neutral particles and though they have nonzero magnetic moment their electromagnetic interactions can be neglected. So the movement of a neutron in a material is not affected by the E/M fields of the atomic electrons and nuclei, but the particle continues its course until it interacts with a nucleus via strong interaction. The short range of the strong interaction and the small size of the nuclei allow the neutrons to travel long distances in matter without interacting. Depending on their energy neutrons have higher probability of interacting in certain ways. If the neutron has kinetic energy $E_n > 1GeV$ its a high energy neutron, if the energy is $10MeV > E_n > 100keV$ its a fast neutron and if $E_n < 0.5eV$ it is a slow neutron.

High energy neutrons undergo mostly elastic or inelastic scatterings. An elastic scattering changes the direction of motion of the neutron and a part of its energy is transfered to the nucleus with which it collided. Collision with lighter nuclei cause larger energy transfer. When a neutron undergoes inelastic scattering with a nucleus it is bounded by the nucleus with simultaneous emission of gamma photons and a neutron of lower energy.

For fast neutrons the most probable interaction is elastic scattering with an atomic nucleus, they may undergo several elastic scatterings until their energy reaches their environments thermal energy. They can also undergo inelastic scattering leaving the nucleus in an excited state, a spontaneous radioactive decay follows an inelastic scattering. Another possibility is that the neutron is absorbed by the nucleus, in which case a nuclear fission or the emission of photons and/or charged particles is caused.

Slow neutrons are more likely to interact with a nuclei either with elastic scattering or with neutron capture. The neutron capture cross section increases as the energy approaches the thermal energy of the environment. After a neutron capture a nuclear fission with energy and charged particle emission may follow.

Neutrinos

While a neutrino or an anti-neutrino traverses through matter it can interact with other particles via weak interaction. These interactions are mediated by the $W^{\pm}$ and Z bosons and cause the absorption of the neutrino by a nucleon that is either free or bound in a nucleus. Possible neutron interactions with nucleons are:

$$\bar{v}_l + p \to n + l^+, \text{ mediated by a } W \text{ boson,}$$
$$v_l + n \to p + l^-, \text{ mediated by a } W \text{ boson,}$$
$$v_l + n \to v_l + n, \text{ mediated by a } Z \text{ boson,}$$
$$\bar{v}_l + n \to \bar{v}_l + n, \text{ mediated by a } Z \text{ boson,}$$
$$v_l + p \to v_l + p, \text{ mediated by a } Z \text{ boson and}$$
$$\bar{v}_l + p \to \bar{v}_l + p, \text{ mediated by a } Z \text{ boson}$$

in the above reactions, l indicates the lepton flavour, so it can be e for electrons and electron neutrinos, μ for muons and muons neutrinos or τ for tauons and tau neutrinos. In order for such a reaction to take place the neutrino (or antineutrino) has to have energy that exceeds a threshold, for the conservation laws to be satisfied, it also has to come very close to a quark bound in a nucleon (the distance has to be of the order of $10^{-18}m$), because weak interaction is a short range interaction. The cross section for neutrino interactions is very small but increases as the neutrino energy increases. Another phenomenon that can occur while neutrinos travel in matter is called "neutrino oscillations" and causes the particle to change its flavour.

1.6.2 Charged Particles in Matter

The electromagnetic fields of the atomic electrons and nuclei cause a charged particle penetrating matter to interact with them via E/M interaction, and thus lose energy along its track. A short description, of the main phenomena that cause energy loss due to E/M interactions, follows.

Heavy charged particles also interact with nuclei via strong interaction as described in the previous section for neutrons.

Elastic scattering

As a charged particle moves it may collide elastically with a nucleus or an electron. Nuclei have larger mass than electrons, so a collision with a nucleus scatters the particle at a larger angle and causes smaller energy loss than a collision with an electron. Because of that one can understand that changes in direction are caused mainly by interactions with nuclei and changes in energy cause changes in energy.

Collisions may lead to excitation or even ionization of atomic electrons, if the interacting particle has sufficient energy. The ionized electrons usually "leave" the atom with small kinetic energy, but some have acquired enough energy from the collision and can travel long distances in matter ($\delta-$electrons). ($\delta-$electrons) in turn may ionize other atoms of the medium they travel inside.

Multiple scattering occurs when a moving particle undergoes many successive collisions, which causes big deflection from its original course. This affects more particles with larger range, because a particle with small range loses its energy before its initial direction changes.

Cherenkov radiation

In a medium light travels with lower velocity than it does in vacuum, so ,though impossible when matter is not present, a particle of very high velocity can travel in a medium faster than light does in that medium. As a charged particle passes through matter it causes polarization of the atoms in the vicinity of its track, after the particle moves further the previously polarized atoms return to their initial state. If the particle moves faster than light does in a material, its E/M field moves slower. As a result the perturbations of the atoms' polarization focus and form a ”wave front” of conic shape and along which optical photons are emitted.

Transition radiation

If a charged particle crosses the boundary between two materials that have different dielectric constants a portion of its kinetic energy is emitted in the form of photons. The mean value of the total energy emitted in each crossing is proportional to the square of the charge of the particle. The process cross section and the energy loss are small and not important unless the particle track crosses several material boundaries, in which case the phenomenon obviously becomes more perceptible.

Bremsstrahlung

The movement of a charged particle in matter is affected by the electromagnetic fields of the atomic electrons and nuclei. As a result the particle is accelerated, which causes the emission of energy in the form E/M radiation (photons). This process is called bremsstrahlung. High energy electrons and positrons lose energy mainly due to bremsstrahlung. For particles other than electrons and positrons the effects of this process can be neglected.

1.6.3 Photons in Matter

High energy photons, while traversing through a medium, can interact with matter primarily via the interactions described below.

Photoelectric effect

The photoelectric effect is the main interaction between photons and atoms when the photon energy is $E_\gamma < 100keV$.

$$\gamma + {}^A_Z X \rightarrow {}^A_Z X^+ + e^- \tag{1.1}$$

In the photoelectric effect a photon of energy E_γ is completely absorbed by an atom of the medium, increasing the energy of an atomic electron and causing the either its excitation or its emission (photoelectron). If the photon energy is sufficient it is most likely that an electron of the lowest energy shell is emitted. For an electron to be ionized the photon needs to have energy at least equal to the binding energy E_I. After the interaction the photoelecron's kinetic energy is $E_e = E_\gamma - E_I$. The emission of an electron due to the photoelectric effect causes a vacancy in the energy shell it was bound to. This vacancy is filled by an electron of a higher energy shell with the simultaneous emission an X-ray photon with energy equal to the difference between the binding energies of the two shells. This photon is quickly interacts with the atom via photoelectric effect and if it has the appropriate energy it can cause the emission of an electron of a higher energy shell, this electron is called an Auger electron.

Compton scattering

Compton scattering is the main interaction between photons and atoms when the photon energy is $E_\gamma \sim 1MeV$.

$$\gamma + e^- \rightarrow \gamma + e^- \tag{1.2}$$

In Compton scattering a photon with energy E_γ collides elastically with an electron, resulting in energy transfer from the photon to the electron. After the interaction relativistic momentum and energy are conserved, the new photon energy is $E'_\gamma < E_\gamma$ and the electron has additional energy $E_e = E_\gamma - E'_\gamma$. Assuming, for simplicity, a free electron and applying the conservation laws the following equation for the photon wavelengths is extracted,

$$\lambda' - \lambda = \frac{h}{m_e c}(1 - cos\theta), \tag{1.3}$$

where λ' and λ are the photon wavelengths before and after the scattering respectively, h is the Plank constant, m_e the electron mass, c the speed of light and θ the scattering angle of the photon. If the electron is bound by a nucleus then there are deviations from the previous equation. For photons with low initial energy the whole atom absorbs the momentum and energy transferred to the electron (coherent Compton scattering or Rayleigh scattering). High energy photons can result in the release of the electron form the atom (incoherent Compton scattering).

Pair production

Pair production is the main interaction between photons and atoms when the photon energy is $E_\gamma \gg 1MeV$.

$$\gamma + {}^A_Z X \rightarrow {}^A_Z X + e^- e^+ \tag{1.4}$$

A gamma ray traversing the E/M field of a nucleus can be transformed into an electron-positron pair. The presence of a nucleus is necessary for the interaction to happen because a small fraction of energy is transferred to the nucleus in order to conserve the momentum and energy. Also pair production is possible only if the photon has energy at least equal to the rest energy of the electron-positron pair, $E_\gamma \geq 2m_e c^2$.

Photonuclear effect

The photonuclear effect resembles pair productions, but takes place due to a strong interaction between high energy photons and nuclei. Even though photons do not carry colour charge and thus are not sensitive to strong interactions, while in matter, they can be transformed into particle-antiparticle pairs. If the produced particles have colour charge, quark-antiquark pair, they interact via strong interaction with the the nuclei of the material. The cross section of the photonuclear effect changes with energy as follows:

- below $10Mev$ the photons do not carry enough energy to produce a quark-antiquark pair, so the cross section is very small,
- below $1GeV$ the cross section shows strong resonant behaviour and
- above $1GeV$ the cross section is almost energy independent.

1.6.4 Particle Showers

Particle interactions with matter may cause the generation of secondary particles, which will also interact with the material they cross with one, or more, of the ways described previously in this section. This causes a cascade of particle production processes that form a particle "shower".

As described before when a high energy electron, or particle moves in matter the main process that causes energy loss is bremsstrahlung. Because of bremsstrahlung high energy photons are emitted. These photons in turn produce an electron-positron pair (pair production). The new particles interact with matter the same way the initial particle did. This causes a chain of bremsstrahlung and pair production processes. So a large number high energy photons, electrons and positrons, are produced and form an electromagnetic shower. An E/M shower stops when the particle energy is low enough that bremsstrahlung is no longer the main energy loss process for electrons and positrons.

A hadronic shower is similar, but instead of electrons, positrons and photons, a large number of secondary hadrons is produced. In this case the production of the "new" hadrons is due to a number of inelastic processes due to strong interactions of a hadron with matter, that happen one after the other.

Chapter 2

Accelerating Particle Experiments

2.1 Particle Acceleration

When a particle with electric charge q is moving with velocity $\boldsymbol{v}$in an electromagnetic field with electric field $\boldsymbol{E}$ and magnetic field $\boldsymbol{B}$ the Lorentz force acts on it.

$$\boldsymbol{F_L} = \frac{d\boldsymbol{p}}{dt} = q(\boldsymbol{E} + \boldsymbol{v} \times \boldsymbol{B}) \tag{2.1}$$

By manipulating the electric and magnetic fields one can control a charged patricle's movement. So the electric field can be used to accelerate said particle and the magnetic field can deflect it from its original direction.

2.1.1 Electric Field

When an electrically charged particle is in an electric field $\boldsymbol{E}$, a force of electromagnetic nature parallel to the filed acts on the particle. If the particle enters the field while already moving and the field is parallel to the velocity direction then the force causes the particle's momentum to increase.

2.1.2 Magnetic Field

If a particle moves in a magnetic field $\boldsymbol{B}$ with velocity $\boldsymbol{v}$, that is perpendicular to the magnetic field, $\boldsymbol{v} \perp \boldsymbol{B}$ then with simple mathematical operations one can observe that

$$\boldsymbol{v} \times \boldsymbol{B} = v \cdot B \tag{2.2}$$

With zero electric field, the Lorentz force, being the cross product of the magnetic field and the velocity, is perpendicular to both. So it acts as a centripetal force and the particle performs circular motion. Also

$$\boldsymbol{F_L} = q \cdot \boldsymbol{v} \times \boldsymbol{B} \implies F_L = q \cdot v \cdot B \tag{2.3}$$

The centripetal force is:

$$F_c = \frac{m \cdot v^2}{\rho} \tag{2.4}$$

where ρ is the radius of the circular motion and m the particle mass. So

$$F_L = \frac{m \cdot v^2}{\rho} \implies \frac{m \cdot v^2}{\rho} = q \cdot v \cdot B \implies mv = qB\rho \implies p = 0.3QB\rho \tag{2.5}$$

In the last equation the momentum, p, is in GeV, the magnetic field, B, is in Tesla, the particle charge, Q, is in e and the circular track radius is in meters.

2.2 Particle Accelerators and Colliders

The operation of particle accelerators is based on the principles that were explained in sections 2.1.1 and 2.1.2. In the cern accelerator complex linear accelerators and synchrotrons are used to accelerate protons and ions.

2.2.1 Linear Accelerators - LINAC

In linear accelerators a particle passes through a series of metal pipes, drift tubes, that are located in a vacuum vessel and connected successively to alternate terminals of an radiofrequency oscillator. When the particle travels through a drift tube there is no electric field to affect it, because the tube of made of conducting material and forms a Faraday shield/cage. But when it travels in the space between two oppositely charged drift tubes the electric field is non-zero and has direction same as the direction of motion of the particle, as a result the particle is accelerated.

A particle is first accelerated by a pair of tubes as it travels in the space between them. When it reaches the end of this space it enters the second tube of the pair. In order to be accelerated again by the next pair of tubes their polarity must change before the particle exits the tube it has entered. Because of the increase in the particle's velocity the length of the drift tubes must also increase along the accelerator.

Though the particle sources "feed" the accelerator with particles continuously, only a bunch of them that are produced in specific time periods are accelerated, thus they form bunches that travel through the accelerator. To ensure that the particles stay in a tight beam superconducting magnets are used.

2.2.2 Synchrotrons

In a synchrotron the acceleration process takes place in a curved vacuum tube, the beam pipe, while the particles move in a circular or near circular path, along the beam pipe.

On some points of the beam pipe there are RF cavities. The electric filed in these cavities causes the energy of a particle to increase each time it traverses through it.The accelerator ring is accompanied by dipole and quadrupole superconducting magnets.

The dipole magnets are called bending magnets and are responsible for the beam of particles following the curved path that the beam pipe offers. Their operation principle is simple, they create a magnetic field that is always perpendicular to the direction of motion of the particles. The result is that on each particle a force of electromagnetic nature is applied. The force vector is perpendicular to the velocity vector and to the magnetic field. So this force acts as a centripetal force that causes the change in the particle motion direction and as a result the circular path of the beam. As shown in section 2.1.2 the particle momentum is given by equation 2.5. So in order to keep the orbit radius constant while the momentum of the particle increases the magnetic field caused by the bending magnets must also increase. The same equation also shows that there are limitations in the maximum momentum a particle can reach in an accelerator, that are dictated by the beam pipe radius and the maximum field available. With conventional electromagnets, the largest field attainable over an adequate region is about $1.5T$, and even with superconducting coils it is only of the order of $10T$. Hence the radius of the ring must be very large to achieve very high energies.

The quadrupole magnets are used for the transverse focusing of the beam and establish a predetermined cross section for it. This is important in order to have a stable orbit and thus ensure that the particles continue the acceleration process and do not strike the sides of the beam pipe. A quadrupole magnet cannot focus the beam in both vertical and horizontal directions at the same time so two types of these magnets are used. One type that is horizontally focusing but vertically defocussing and the other one is vertically focusing but horizontally defocussing. To be exact the two types are the same but in order to achieve focusing in perpendicular directions, one is rotated by 90^o.

After the the completion of the acceleration in the synchrotron (when the beam has reached the maximum possible energy) the beam is either extracted from the accelerator to be used in an experiment or to promote it to another accelerator, or stays in the current accelerator, that is no longer increasing the beam energy but acts as a storage ring for the beam.

2.2.3 Fixed target and Colliding beam experiments

After achieving the desired energy for the beam, it can be used for experiments. These experiments can either be fixed-target, in which the beam is directed onto a stationary target, or colliding where two particle beams move in opposite directions and collide with each other. Such beam collisions can be achieved by combining two accelerator rings that accelerate particle beams in opposite orbits. In these machines there are points on the rings where the two beams can be directed at each other using magnets, in order to collide some of the beam particles.

2.3 The CERN accelerator complex

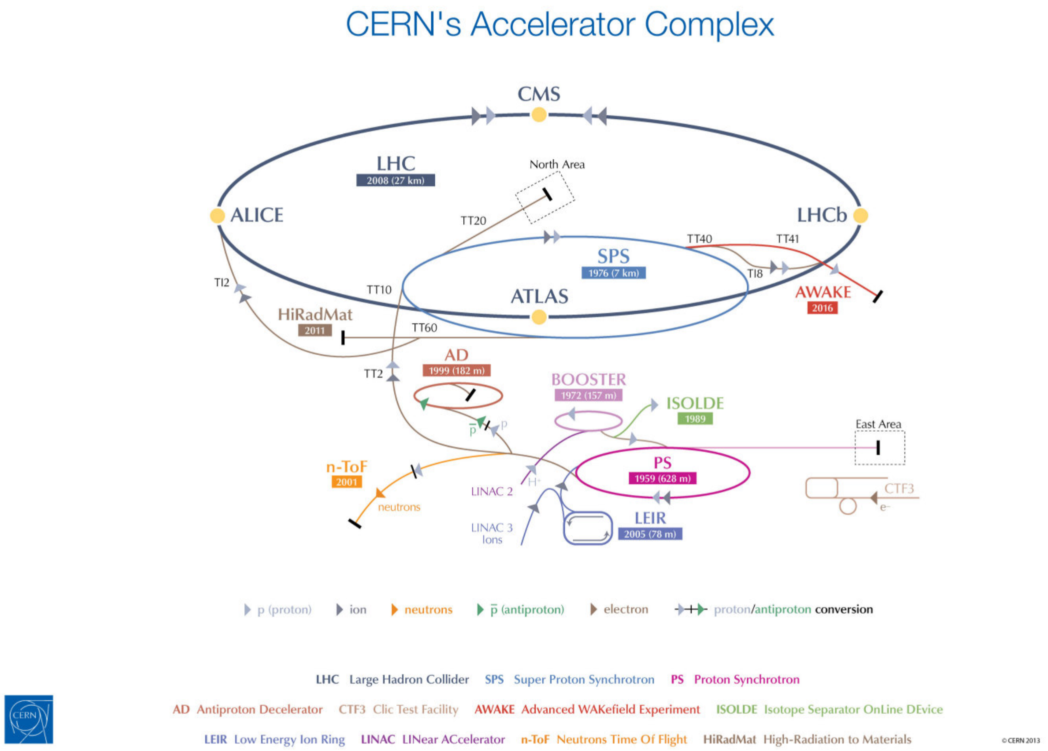

Figure 2.1: Figure of the CERN accelerator complex. [21]

The CERN accelerator complex consists of a combination of LINACs and synchrotrons that accelerate beams of particles until they reach the needed, for experiments, energy. These beams can be used for both fixed-target and colliding experiments. A description of the stages a particle follows from its production up to its use for an experiment is given in this chapter, in the following sections. It also also includes the Antiproton Decelerator and the Online Isotope Mass Separator (ISOLDE) facility, and feeds the CERN Neutrinos to Gran Sasso (CNGS) project and the Compact Linear Collider test area, as well as the neutron time-of-flight facility (nTOF). In figure **??** the accelerator Complex with the experiment nodes is shown.

2.3.1 Particle Sources

The process starts at the particle sources. The proton source is a bottle of hydrogen gas, the hydrogen atoms first pass through an electric field to be striped off of their electrons, leaving only protons to enter the accelerator that follows. For the heavy ions a small sample of solid lead-208 is heated to around $800^o C$ to become vapour. The lead vapour then is ionized and the ions are extracted and enter the accelerator.

2.3.2 1^{st} Acceleration Stage - Linear Accelerators

After their production, the particles enter a linear accelerator, whose operation was described in 2.2.1. For the protons' acceleration LINAC 2 is used and for the lead ions are accelerated by another linear accelerator, LINAC 3. Exiting LINAC 2 the protons have reached the energy of $50 MeV$ and gained 5% in mass.

2.3.3 2^{nd} Acceleration Stage - Low Enegry Ion Ring and Proton Synchrotron Booster

After exiting LINAC 2 the proton bunches enter a second accelerator, the Proton Synchrotron Booster (PSB). There they are accelerated to $1.4 GeV$.

The lead-208 ions after their acceleration in LINAC 3 enter the Low Energy Ion Ring (LEIR). Each bunch form LINAC 3 is split into four shorter bunches and then the new particle bunches are accelerated in groups of two, from $4.2 MeV$ to $72 MeV$.

After completing the first two stages of the acceleration process, the same stages are used for both the protons and the lead-208 ions to achieve the maximum energy.

2.3.4 3^{rd} Acceleration Stage - Proton Synchrotron

The 3^{rd} stage is when the protons and the lead ions exit the PSB and LEIR respectively and enter the proton synchrotron (PS). At the and of the acceleration process in the PS, a proton bean exits with energy $25 Gev$ and an ion beam exits with energy $72 MeV$.

2.3.5 4^{th} Acceleration Stage - Super Proton Synchrotron

In this stage the Super Proton Synchrotron (SPS) boosts the energy of the proton beam exiting the PS up to $450GeV$. LEAD IONS The SPS is also used to accelerate particles for fixed target experiments.

2.3.6 5^{th} Acceleration Stage - Large Hadron Collider

The Large Hadron Colliter (LHC) is a synchrotron type accelerator that, as its name indicates, belongs to the category of colliding beam machines. It is the main, and largest, ring of the CERN accelerator complex. There two particle beams of protons or lead ions are accelerated in opposite orbits, in two separate beam pipes – two tubes kept at ultrahigh vacuum, until they have the maximum possible energy, at which their speed is close to the speed of light. After achieving the maximum energy the two beams collide in one of the four locations around the accelerator ring, where detectors are placed to gather data for each experiment. The detectors are ATLAS, CMS, ALICE and LHCb.

The maximum energy a proton beam can reach in the LHC is $6.5TeV$, so for two beams the total energy is about $13TeV$. The lead-ion beams have a maximum collision energy of $1150TeV$.

2.3.7 Other facilites on the accelerator complex

The accelerator complex includes the Antiproton Decelerator and the Online Isotope Mass Separator (ISOLDE) facility, and feeds the CERN Neutrinos to Gran Sasso (CNGS) project and the Compact Linear Collider test area, as well as the neutron time-of-flight facility (nTOF).

Chapter 3

Particle Detection - ATLAS

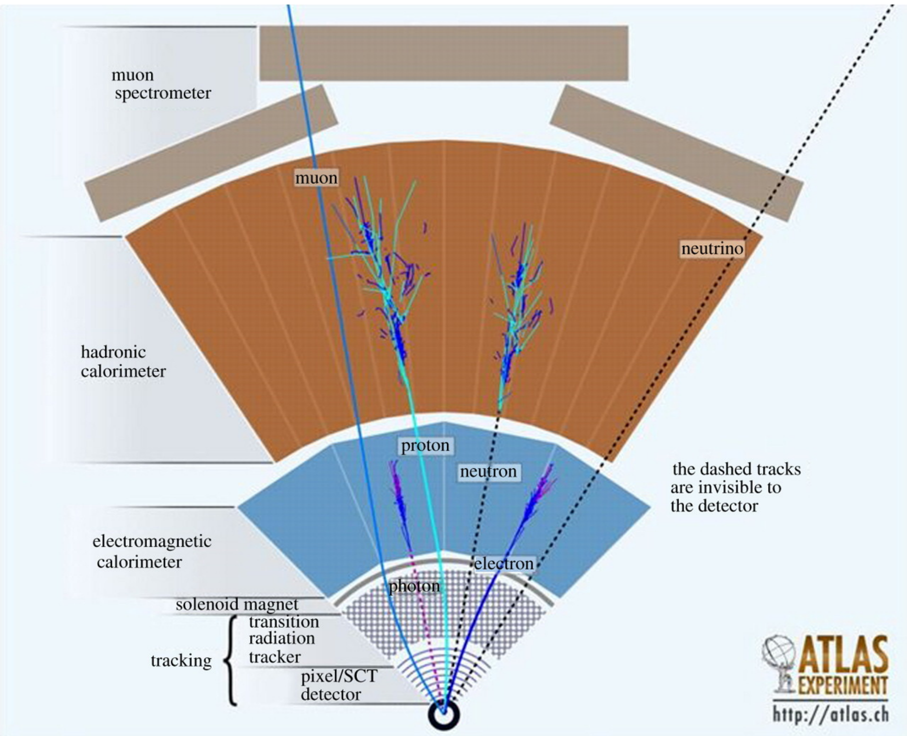

Figure 3.1: Tracks of different particles in the detector.

3.1 Particle Detectors

High energy particle collisions may produce evidence of physics only theorized about or even unknown so far. In order to be able to observe such evidence the invention and constant development of particle detectors is necessary. This chapter is a brief explanation of the operation principles of detector types used in ATLAS.[1]

[1]For in depth explanation of these, as well as other, detecting techniques refer to the corresponding bibliography.

Particle detection is based on the interactions particles undergo while traversing matter. It may refer to the estimation of the time a particular event took place, the particle's track reconstruction, the measurement of a particle's momentum, energy, velocity, spin, mass or charge.

3.1.1 Semiconductor Detectors

ATLAS uses semiconductor detectors for particle tracking. The pixel detector and the silicon microchip tracker (both subsystems of th inner detector) belong to this category.

This type of detectors are not supposed to absorb a substantial amount of the particle energy but recognize it and let it continue its course. As a charged particle passes through the semi-conducting material of the detector a number of electron-hole pairs is created, that are then separated by an electric field and collected by electrodes. This current caused by the passing of the charged particle generates a "*hit*" signal for the readout electronics which results in the information that a charged particle crossed the detector at that particular point. Combination of different "*hits*" leads to an approximate reconstruction of the particle track.

Tracking detectors operate in a magnetic field ($2T$ parallel to the beam line field generated by the solenoid magnet for ATLAS) and the Lorentz force curves the track of the detected particle. The curvature measurement, in a known magnetic field, is essentially the particle's momentum measurement.

3.1.2 Gas chamber detectors

Gas chamber detectors are also used for particle tracking, as well as triggering. In the gas volume an electric field is applied due to voltage difference between an anode and a cathode. As a charged particle crosses the gas volume it causes ionization of the gas atomic electrons, which are accelerated, by the electric field, towards the anode. This creates an electric current-signal and outputs the particle's track.

Wire Chambers

The anode of wire chambers is a thin wire with high voltage potential. The gas chamber may have cylindrical shape (tube), with a cylindrical cathode and a single anode wire stretched along its axis. Drift tubes use the drift time of the ionized gas electrons from their creation to their collection from the anode, for the track reconstruction.[2] The ATLAS TRT (inner detector) and MDT (muon spectrometer) modules are made of drift tube chambers. Another type of wire chambers has planar cathodes and several anode wires at fixed distances between them (MultiWire Proportional Chamber - MWPC), each of which is a separate detector. The ATLAS TGC and CSC modules (muon system) are both made of MWPCs.

Resistive Plate Chambers

The gas volume is between two parallel resistive plates. Between those two plates an electric field directs the ionized electrons towards the anode where they are collected and the signal is generated.[3] On the outer sides of the resistive plates the signal is read out via capacitive coupling to metallic strips. ATLAS has RPCs as a part of its muon system.

3.1.3 Calorimeters

Calorimeters measure a particle's energy by total absorption. High energy photons, electrons/positrons and hadrons when traversing a dense material, cause showers of secondary particles.[4] Depending on the shower the absorbed particle initiates in a calorimeter two different types can be distinguished, the electromagnetic (for photons and electrons) and the hadronic (for hadrons) calorimeters. The energy of the initial particle can be measured by the length of the shower.

Electromagnetic Calorimeters

The main process of energy loss for a high energy photon is pair production and for electrons and positrons is bremsstrahlung. This means that until the products of such interactions reach a critical energy the number of particles rises exponentially with distance, reaching a maximum at the end of the shower.

Electromagnetic Calorimeters can be either homogeneous or sampling. Homogeneous calorimeters are made of materials that have a combination of the properties of detecting and absorbing materials. Sampling calorimeters are made of an array of thin detecting layers mediated by thick layers of dense absorbing materials.

[2]Drift chambers do not necessarily have cylindrical shape. There are also planar drift chambers but ATLAS uses cylindrical ones.

[3]In this type of gas chambers there is no anode wire. On plate is the anode and the other is the cathode.

[4]Calorimetry is also possible for muons but the muon must have initial energy equal or higher than $1TeV$.

Hadronic Calorimeters

As with E/M calorimeters and their respective particles, in a hadronic calorimeter a fast hadron initiates hadronic showers. Strong interaction between the initial particle and the calorimeter material nuclei cause the production of secondary hadrons and so on. In this type of calorimeters a part of the energy is also transformed into electromagnetic showers, because one of the main products of a hadronic shower is the neutral pion (π^0) that decays into two gamma rays, which in turn cause an E/M shower each. Hadronic calorimeters are always sampling.

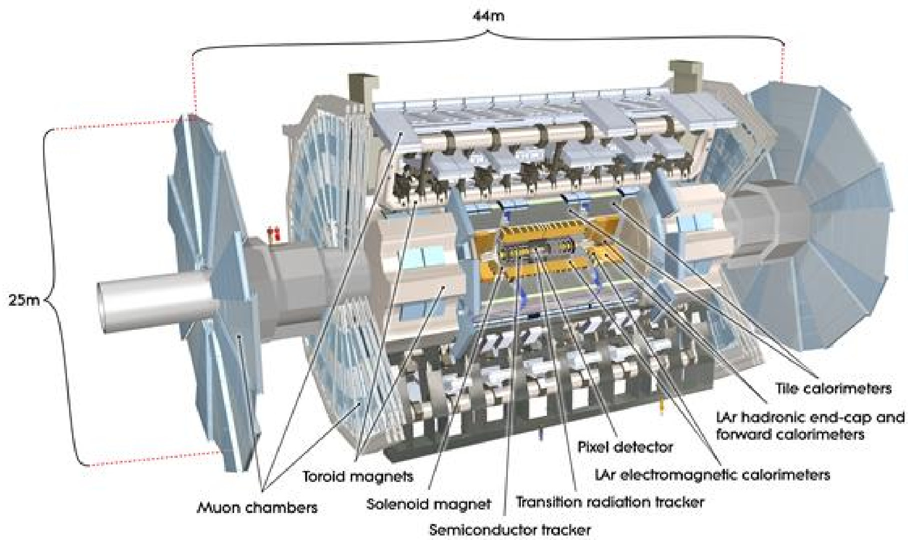

Figure 3.2: The ATLAS detector. [22]

3.2 The ATLAS experiment

ATLAS (A Toroidal LHC ApparatuS) is an experiment detector located at one of the four collision points of the LHC. It is comprised of multiple layers, each with a different role in particle detection. The structure is cylindrically symmetric around the LHC beam pipe and the part on one side of a plane perpendicular to the beam pipe on the interaction point is a mirrored copy of the part on the other side.

The detecting systems, starting at the collision point and moving outward are the following:

- Inner Detector: tracking the trajectories of charged particles
- Calorimeters: measurement of direction and energy of electrons, photons and hadrons by total absorption

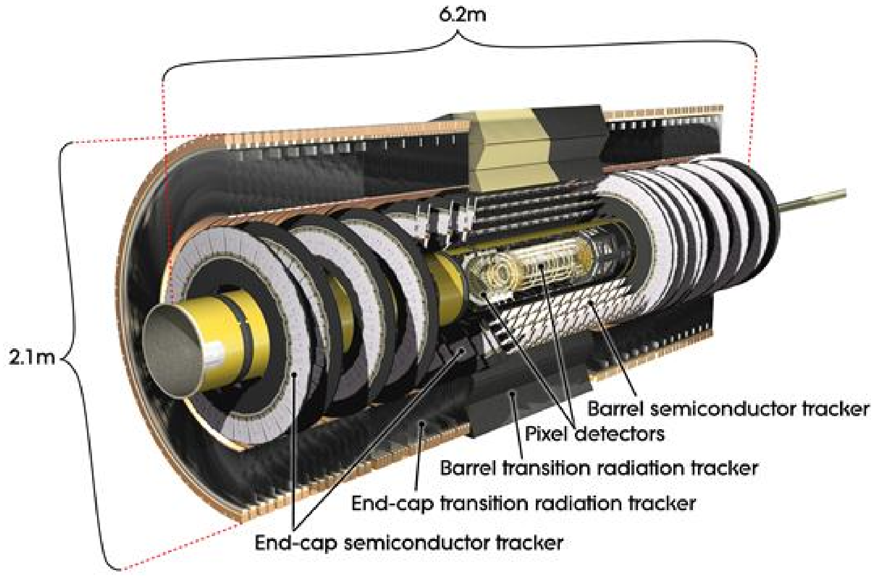

Figure 3.3: The inner detector. [23]

  - Electromagnetic Calorimeter: measurements of electrons and photons
  - Hadronic Calorimeter: measurements for hadrons

- Muon Spectrometer: direction and momentum measurement of muons in a non-destructive manner

After a collision the particles produced travel in all directions and cross the detector layers. All particles pass the inner detector. Electrons and photons reach the electromagnetic calorimeter, where they stop causing electromagnetic showers. Hadrons (protons, neutrons etc.) reach the hadronic calorimeter where they stop causing hadronic showers. Muons pass trough all detection systems, even the muon spectrometer where they are detected, as do neutrinos, which are invisible to the detector.

3.2.1 The Beam Pipe

The beam pipe is a part of both the detector and the accelerator. Inside the beam pipe is the interaction point, where particle beams, accelerated by the LHC, collide. It has cylindrical shape and the wall thickness, as well as the materials vary along the beam pipe, details of the geometry and the materials in chapter 5.

3.2.2 The Inner Detector

The first detection level is the Inner Detector (ID), that measures the direction, momentum, and charge of electrically-charged particles produced in each proton-

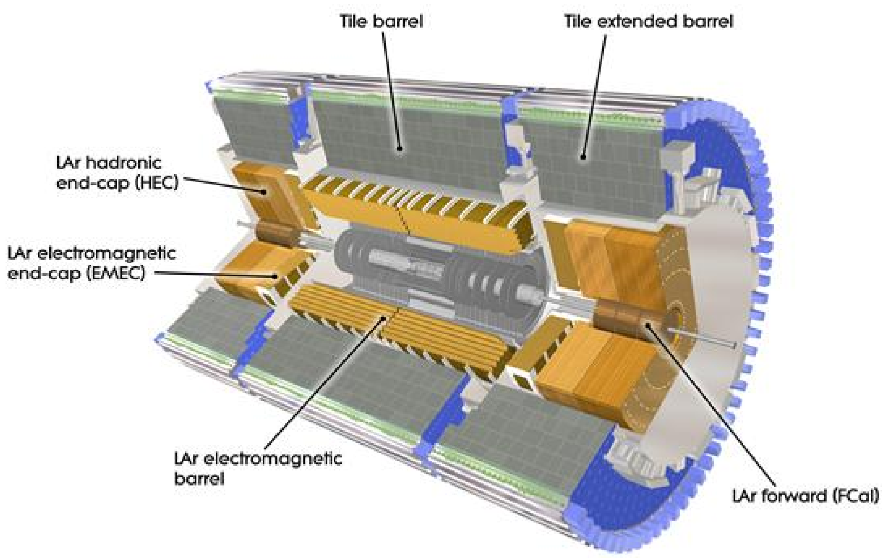

Figure 3.4: The calorimetry system. [24]

proton collision. It operates in a $2T$ magnetic field parallel to the beam line, that is generated by the central solenoid. The I.D. has three subsystems, the pixel detector, the silicon microchip tracker and the transition radiation tracker, each with a barrel and two end-cap regions (one on each side of the barrel).

Pixel Detector

The pixel detector barrel and end-cap regions have three layers of detectors positioned symmetrically around the interaction point, cylindrical for the barrel part and disk-shaped for the end-caps. The detector is semi-conducting, made of silicon wafers with pixel sensors.

Silicon Microchip Tracker (SCT)

The barrel part of the SCT has four cylindrical layers and nine layers of end-cap disks. It is also a semi-conducting detector and is made of silicon microchips.

Transition Radiation Tracker (TRT)

The TRT is a gas detector made of straw tubes containing a gas mixture with $\sim 70\%$ Xenon. It has two barrel parts one on each side of the interaction point that have a very small gap ($\sim 1.5cm$) between the along the $z-$direction. There are three barrel layers with the first one having two parts the inner of which has smaller length than the outer. The end-caps have two different sets of 20 wheels in total. Their difference is the spacing between the tube layers that make one wheel. The

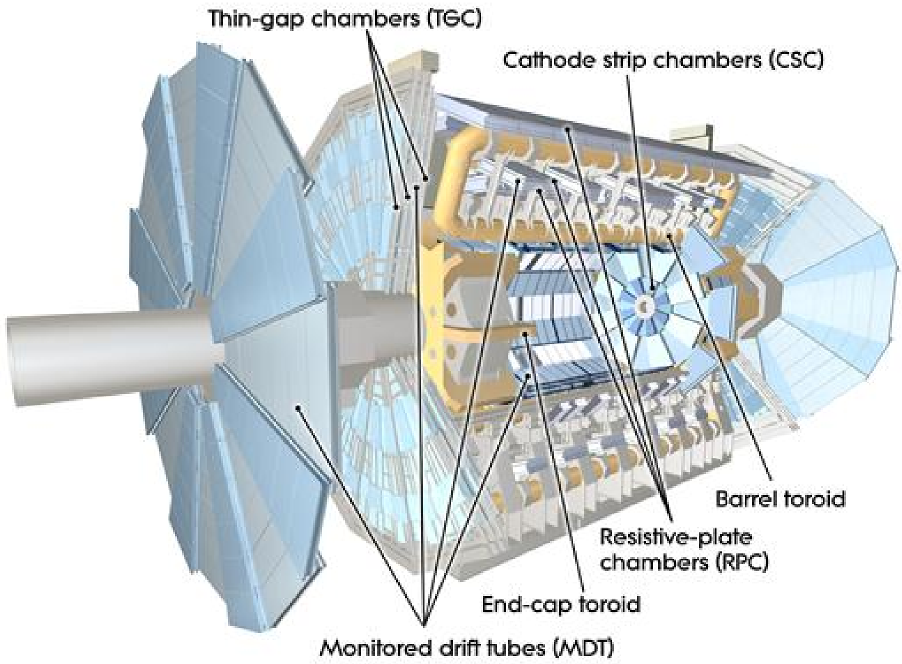

Figure 3.5: The muon system. [25]

first 12 have 8 tube layers placed $8mm$ apart while the latter 8 have 8 tube layers placed $15mm$ apart.

3.2.3 The Calorimeters

The calorimeter system consists of electromagnetic and hadronic calorimeters. In the E/M calorimeters, the energy of electrons and photons is measured and in the hadronic calorimeters the energy of hadrons. All modules are of sampling type with consecutive absorbing material layers intermediating sampling medium layers. The calorimetry system is transparent to muons and neutrinos.

Electromagnetic Calorimeters

The electromagnetic calorimeters have liquid Argon as the sampling material and Lead as the absorber. It has two half barrels separated by a small gap at the interaction point and four end-cap wheels (two on each side). The calorimeters are complemented by the presampler. For the barrels, the presampler is a thin liquid Argon layer covering the inner surface of the cylinders. In the end-cap region, the presampler is a thick liquid Argon layer located in front of the end-cap modules.

Hadronic Calorimeters

There are three levels of hadronic calorimeters, the Tile Calorimeter, the Hadronic End-Cap Calorimeters (HEC) and the Forward Calorimeters (FC).

Tile Calorimeter

The Tile calorimetres has only a barrel section that is made of one central barrel and two extended barrels (one on each side of the central). The active medium is scintillator and the absorbing material is steel.

Hadronic End-cap Calorimeter

The end-caps of the hadronic calorimeter are placed directly behind the E/M calorimeter end-caps. They are made of liquid Argon (active medium) and Copper (absorber). There are two end-cap wheels on each side of the I.P.

Forward Calorimeters

The forward calorimetry system is made of three modules (each module has an identical one positioned symmetrically with respect to the I.P.). All modules have liquid Argon as the active material, the first one uses Copper as the absorber and the other two Tungsten.

3.2.4 Magnet System

The ATLAS magnet system is composed of the central solenoid and the toroid magnets. The central solenoid magnet provides the magnetic field for track bending in the inner detector region. The toroid magnet system has one large barrel toroid and two smaller end-cap toroids. Eight rectangular coils made of superconducting NbTi cables for each magnet, are arranged around the beam line. They create the necessary magnetic field in the muon spectrometer system for momentum calculations.

3.2.5 The Muon Spectrometer

The Muon Spectrometer is the detection layer after the calorimeters. All previous layers are transparent to muons and this one is responsible for the identification of muons and the measurement of their momentum. Four types of detecting chambers are used for the muon system, the Monitored Drift Tubes (MDT), the Cathode Strip Chambers (CSC), the Thin Gap Chambers (TGC) and the Resistive Plate

Chambers (RPC). The muon system operates in the magnetic field created by the superconducting barrel toroid.

Monitored Drift Tubes

The monitored drift tubes measure the curves of muon tracks. These chambers are made of drift tubes filled with a gas mixture of Argon (Ar) and Carbon dioxide (CO_2) and a tungsten-rhenium anode wire. They are arranged in three barrel, Barrel Inner, Middle and Outer and three end-cap, End-Cap Inner, Middle and Outer layers. There is also an additional set that are constructed like barrel chambers but serve in the end-cap system the Barrel End-Cap Extra layer. The modules of each layer spread azimuthally around the beam pipe in 16 sectors. With some exceptions the design is symmetrical around the $z-$axis and the interaction point.

Cathode Strip Chambers

The CSCs are gas chambers filled with an Ar/CO_2 gas mixture and have gold-plated tungsten anode wires. They segmented in small and large chambers and are arranged azimuthally around the beam axis in 16 sectors, the large chambers are in odd-numbered sectors and small chambers in even-numbered sectors. They are used to measure precision coordinates at the ends of the detector.

Resistive Plate Chambers

Each RPC chamber is made of two parallel phenolic-melaminic plastic laminate plates the space between which is filled with a $C_2H_2F_4/Iso{-}C_4H_{10}/SF_6$ gas mixture. The outer small MDT modules are complemented by one RPC layer under the module, the outer large modules by one RPC layer over the module and all the middle MDT modules have one RPC layer under and one over the module. They are part of the triggering system and measure the 2^{nd} coordinate in the central region of the detector.

Thin Gap Chambers

The TGCs are gas chambers filled with a $CO_2/n - C_5H_12$. They complement the end-cap MDT modules and can have either two gas gaps (doublets) or three gas gaps (triplets). The inner end-gap layer MDT modules are complemented by two layers of doublet TGCs, the middle end-gap layer MDT modules by one layer of triplet TGCs and the outer end-gap layer of MDT modules by two layers of doublet TGCs. They are needed for triggering and for 2^{nd} coordinate measurements (non-bending direction) at the ends of the detector.

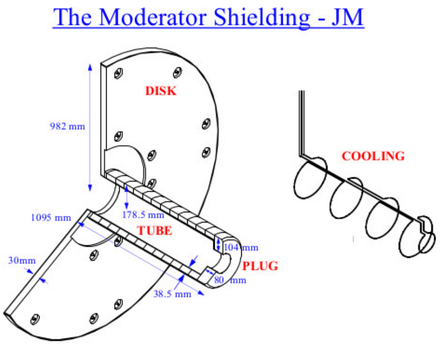

Figure 3.6: JM shield. [26]

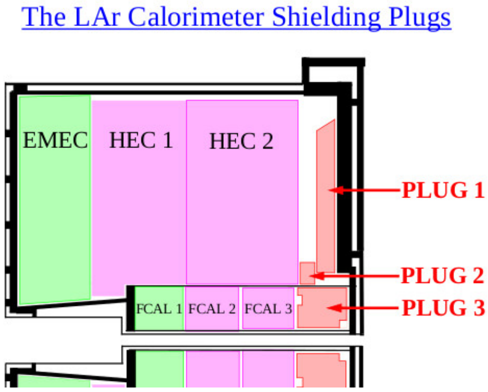

Figure 3.7: Plugs. [26]

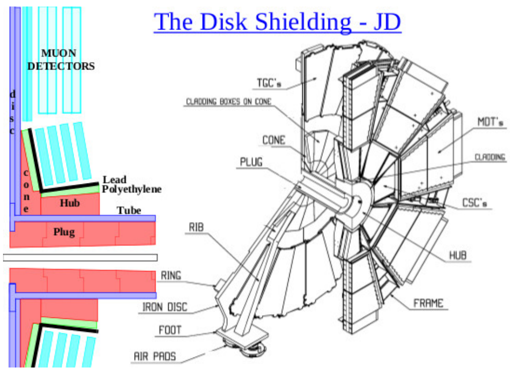

Figure 3.8: JD shield. [26]

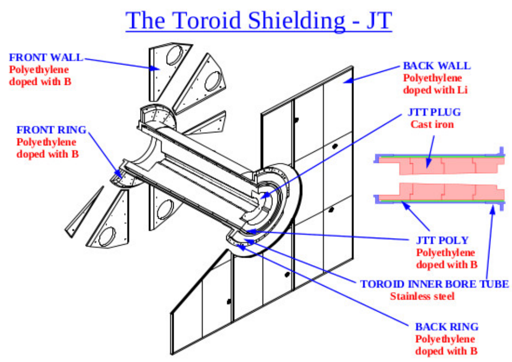

Figure 3.9: JT shield. [26]

3.2.6 Shielding

The Moderator Shield - JM shield

The moderator shielding covers the front face of the end-cap electromagnetic calorimeter and the alcove infront of the forward calorimeters. It is composed br three parts a disk followed by a tube and then a plug as can be seen in figure 3.6. All parts are made of boron carbide doped polyethylene and are covered by a thin aluminum layer. The main role of this shielding region is to protect the inner detector from back-splash neutrons from the calorimeters.

Calorimeter Shielding Plugs

At the back end of the end-cap and forward calorimeters are three brass plugs that can be seen in figure 3.7.

Disk Shielding - JD Shield

The JD shield, figure 3.8, starts with a steel disk followed by a stainless steel tube filled with a brass plug. In the region over the steel tube and under the CSCs and

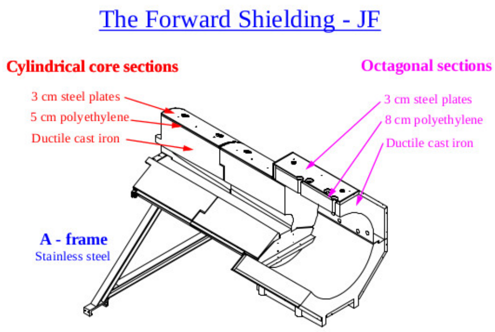

Figure 3.10: JF shield. [26]

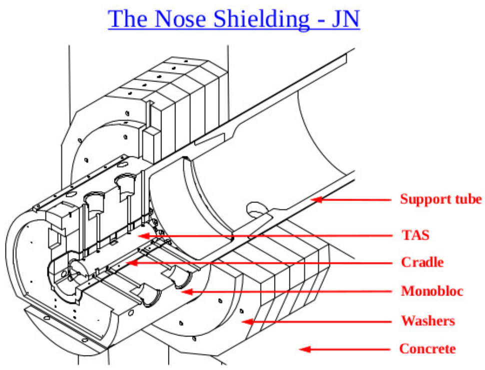

Figure 3.11: JN shield. [26]

there are a cone and a hub made of brass and cladded by one polyethylene and one lead layer. The disk shielding protects the first muon chambers from radiation while offering them support and returning the magnetic field from the solenoid.

Toroid Shielding - JT shield

The toroid shield, figure 3.9, can be divided into two main parts the JTT and the JTV shielding. The JTV shielding consists of the front wall made of polyethylene doped with boron carbide, a front and back ring of doped polyethylene, a back wall made of polyethylene doped with lithium. The JTT shielding is a cylindrical structure made of ductile cast iron, with a polyethylene cladding layer which acts as neutron shielding. The JTV moderates the neutron radiation and then stops the low-energy neutrons.

Forward Shield - JF shield

The purpose of the two Forward Shielding assemblies (JF) is to protect the big muon wheel and the muon EO chambers from background particles created in secondary interactions in the beampipe, the calorimeters and the TAS collimators. There are two parts, the cylindrical core and the octagonal back, both made of ductile iron with two cladding layers, the inner made of boron doped polyethylene and the outer of steel. The layout is shown in figure 3.10.

Nose Shielding - JN shield

The nose (JN) shielding supports the TAS collimator and protects the detector from the radiation created in the TAS. The purpose of the TAS collimator is to prevent the first LHC quadrupole from quenching due to the heat created by the particles from the interactions in ATLAS. The JN monobloc is made of cast iron and it is supported by a cast iron tube in a concrete structure (washers). In the monobloc is the copper TAS collimator and its iron cradle. The layout is shown in figure 3.11.

Cavern

The detector is inside an approximately rectangular cavern made of thick concrete walls.

3.2.7 p-p Interactions at the I.P.

In the LHC ring there are two proton beams one moving clockwise and one counter-clockwise. In reality those beams are about 3550 bunches of $\sim 1.15 \cdot 10^1 1$ protons, with a $\sim 25ns$ time spacing from each other. At the center of the detector, the Interaction Point (I.P.), beams meet resulting in the crossing of proton bunches and the collision of protons, thus producing new particles that travel in all directions. The protons in a bunch are tightly squeezed in a $16\mu m \times 16\mu m \times 7.5cm$ volume by E/M fields to increase the probability that during a crossing protons will come close enough to collide.

The velocity of the particle beams is close to 99.9% of the velocity of light before they meet. This leads to interactions with $14TeV$ center of mass energy, approximately $7TeV$ momentum for each beam.

The two beams cross at an angle, so the the overlapping area between two crossing bunches depends on the crossing angle as well as the rms of each size dimension of a beam bunch. The crossing angle at the LHC is $\theta_c = 285\mu rad$.

During a bunch crossing at the I.P. some protons of one beam undergo elastic or inelastic interactions with protons from the other beam. The interesting, for high energy phisics experiments, are the inelastic p-p interacions. At LHC energies the cross sections of protons interacting in an inelastic way is about $60.3mb$ [1]. At luminocity $L = 10^3 4cm^{-2}s^{-1}$ about 20 such interactions happen every time two bunches meet at the I.P. which results to approximately 6×10^8 collisions every second.

Chapter 4

FLUKA

FLUKA is a fully integrated particle physics MonteCarlo simulation package. It is a general purpose tool for calculations of particle transport and interactions with matter, covering an extended range of applications spanning from proton and electron accelerator shielding to target design, calorimetry, activation, dosimetry, detector design, Accelerator Driven Systems, cosmic rays, neutrino physics, radiotherapy etc.

flair is an advanced user friendly interface for FLUKA to facilitate the editing of FLUKA input files, execution of the code and visualization of the output files. It is based entirely on python and Tkinter.

In order to understand the detailed description of the simulation setup in chapter 5, this chapter contains definitions of terms and explanations of the process followed to design and create the final detector geometry.

4.1 The Monte Carlo Method

"The (Monte Carlo) method is, essentially, a statistical approach to the study of differential equations, or more generally, of integro-differential equations that occur in various branches of the natural sciences."[27]

The core idea of Monte Carlo is to learn about a system by simulating it with random sampling. That approach is powerful, flexible and very direct. It is often the simplest way to solve a problem, and sometimes the only feasible way. The Monte Carlo method is used in almost every quantitative subject of study: physical sciences, engineering, statistics, finance, and computing, including machine learning and graphics. Monte Carlo is even applied in some areas, like music theory, that are not always thought of as quantitative.

In general Monte Carlo is an integration tool. It uses random numbers generated by a random number generator (RNG) that follow a normal distribution to calculate function integrals. Particle interactions have a stochastic nature and the probability of an event occurrence is related to a quantity called cross section. Using the Monte Carlo method

4.2 Terminology

Terminology of the simulator is used in this chapter as well as in chapter 5 to describe the simulation design.

1. Body: Any solid figure (three-dimensional figure) or surface used to simulate the detector. closed solid bodies (spheres, parallelepipeds, etc.) or semi-infinite portions of space (half-spaces, infinite cylinders) delimited by surfaces of first or second degree.

2. Region: Portions of space with specific properties. combine bodies by boolean operations (addition, intersection and subtraction) to perform a complete partition of the space of interest into regions, namely cells of uniform material composition.

3. Zone: Substractions of space that are defined by their relative position to one or more bodies.

4. Source: Initial (primary) particles that have predefined momentum/energy and direction and starting position.

4.3 Body definitions

To simulate the ATLAS detector geometry, cylinders, planes and cones were used[1]. This section contains general description of these bodies along with some details for their definition in the simulation.

4.3.1 Right Circular Cylinders. Code: RCC

A right circular cylinder is a solid cylinder with circular ends perpendicular to its axis. Each RCC, pictured in figure 4.1, is defined by 7 numbers: V_x, V_y, V_z (coordinates of the centre of one of the circular plane faces), H_x, H_y, H_z (x-, y- and z-components of a vector corresponding to the cylinder height, pointing to the other

[1]Not all bodies defined in the simulation correspond to a real detector part or boundary. Some are used as a tool to segment the area and work in one part without the changes affecting the rest.

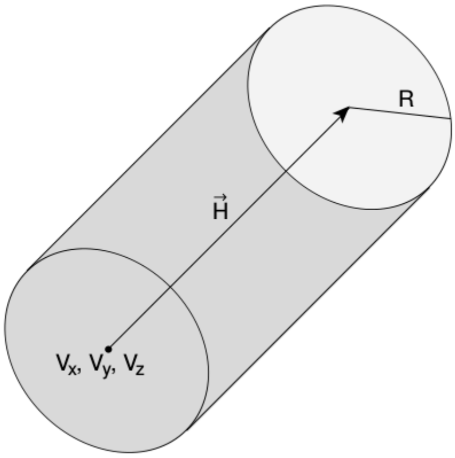

Figure 4.1: Right Circular Cylinder (RCC). [28]

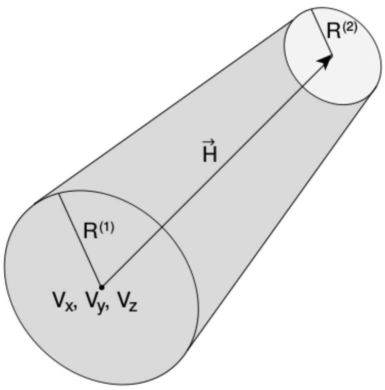

Figure 4.2: Truncated Right Angle Cone (TRC). [28]

plane face), R (cylinder radius). In the simulation all cylinders defined had axes parallel to the z- coordinate axis and were centred around z, so for all cylinders:

- The position of the centre of the circular planes lies on the z-axis,$V_x = V_y = 0$.
- The cylinder height vector is parallel to the z-axis, $H_x = H_y = 0$.
- The z-component of the height vector equals the length, or thickness of the detector component simulated (length for barrel parts and thickness for end-cap parts).
- The V_z coordinate is referred to as the "face position" of the cylinder, because it is the only non-zero coordinate of the circular plane's centre and is the same for all of its points.

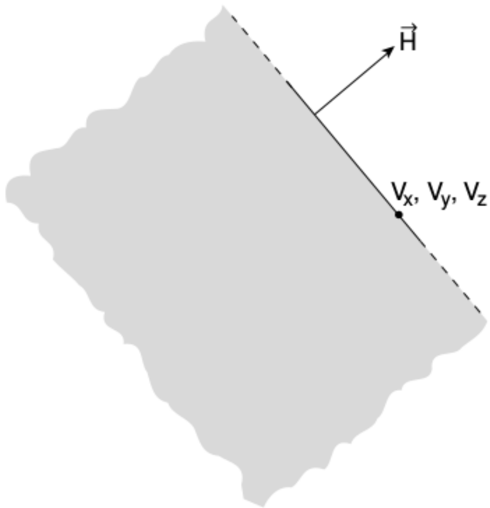

Figure 4.3: Infinite half-space delimited by a generic plane (PLA). [28]

To simulate each cylindrical-shell, or ring, type item two cylinders were used. These bodies share all but one defining numbers. The one that differs is R and the space between the two bodies represents the desired item.

4.3.2 Truncated Right Angle Cones. Code: TRC

A right angle cone is a solid cone with circular bases perpendicular to its axis. Each TRC, pictured in figure 4.2, is defined by 8 numbers: V_x, V_y, V_z, (coordinates of the centre of the major circular base), H_x, H_y, H_z (components of a vector corresponding to the TRC height, directed from the major to the minor base), $R^{(1)}$ (radius of the major base), $R^{(2)}$ (radius of the minor base). In the simulation all cones defined had axes parallel to the z- coordinate axis and were centred around z, so for all cones:

- The position of the centre of the circular planes lies on the z-axis,$V_x = V_y = 0$.
- The cone height vector is parallel to the z-axis, $H_x = H_y = 0$.
- The z-component of the height vector equals the length of the detector component simulated .
- The V_z coordinate is referred to as the "face position" of the cone, because it is the only non-zero coordinate of the circular plane's centre and is the same for all of its points.

To simulate each cone-shell type item two cones were used. These bodies share all but two defining numbers. Those that differ are $R^{(1)}$ and $R^{(2)}$. The space between the two bodies represents the desired item.

4.3.3 Generic infinite half-space. Code: PLA

Each PLA, pictured in figure 4.3, is defined by 6 numbers: H_x, H_y, H_z (x-, y- and z- components of a vector of arbitrary length perpendicular to the plane), V_x, V_y, V_z (coordinates of any point lying on the plane). The half-space "inside the body" is that from which the vector is pointing (i.e., the vector points "outside"). Planes were used with multiple purposes. The detector modules that have prismatoid shape where made either entirely by planes or with the combination of cylinders and planes. Another use of PLA bodies is for the definition of the borders between two consecutive parts, of the same module, that belong in different regions.

4.4 Beams and Particle Sources

This section contains general description of the input file option lines used to define the necessary sources for the experiment proton beam simulation.

4.4.1 Particle Beam. Code: BEAM

With this option the user defines several beam characteristics: type of particle, energy, divergence and profile. When used with the option SPECSOUR it defines the maximum energy/momentum.

4.4.2 Beam Position. Code: BEAMPOSit

Defines the coordinates of the centre of the beam spot (i.e., the point from which transport starts) and the beam direction. Also allows to define some spatially extended sources.

4.4.3 Special Sources. Code: SPECSOUR

This option allows, with an input of up to 18 double precision parameters depending on the option specified by the type defining card, the production of a source from two colliding beams. The collision type is described by the CROSSSYM option, which means symmetric crossing. The rest of the parameters are used to define:

- The particle type (protons are used) for the colliding beams
- The lab momentum of each beam
- The crossing angle of the beams

- The standard deviation of the Gaussian sampling of the interaction position around the interaction point in all dimensions.

Chapter 5

Simulation Design

This chapter analyses only the details for the reproduction of the ATLAS detector geometry in the simulation environment [1]. The function and role of each part of the detector are discussed in chapter 3. The entire detector of the experiment, so the one side is a mirrored copy of the other. The z-direction is along the beam line axis and the LHC slope is not taken into account for the simulation design. All geometry figures of this chapter are not on scale. They are intended for understanding the layout of different parts of the detector and contain some details helpful for this purpose.

5.1 The beampipe

The beam pipe was designed with the parameters shown in table 5.1. The dimensions and positions in this table refer to the parts of the pipe that are in the positive part of the z-axis. The other half of the beam pipe is a mirrored copy of the one described with respect to the $x - y$ plane.

In the simulation the design was made utilizing cylinders, cones and planes parallel to the $x-y$ plane. Every cylindrical part uses two cylinders of the same length but different radii and their relative complement is the space where the beam pipe part physically exists. Similarly with conic parts. Planes are used for separating purposes because the software manual suggests so. The beam pipe can be divided in 9 sectors that have either different shape their immediate neighbours, or are made of a different material. Examples of some beam pipe parts can be seen in figures 5.1 and 5.2. In these figures the hatched part is the beam pipe, $z - Start$ and $z - End$ for each sector are in table 5.1. Conic parts may flare or shrink while moving to

[1] In the following sections, unless stated otherwise, *cm* are used as the unit for all length measurements.

Sector	z-axis Start	z-axis End	Length	R_i	R_o	Thickness
1	0.0	355.0	355.0	2.9	2.98	0.08
2	355.0	365	10	2.9	2.98	0.08
3	365.0	1046.5	681.5	2.9	2.98	0.08
4	1046.5	1050.7	4.2	2.9(4.0)	2.98(4.1)	0.08 (0.1)
5	1050.7	1434.2	383.3	4.0	4.1	0.1
6	1434.2	1441.6	7.4	4.0(6.0)	4.1(6.15)	0.1(0.15)
7	1441.6	1865.0	423.4	6.0	6.15	0.15
8	1865.0	1888.0	23.0	6.0(1.7)	6.15(3.0)	1.3
9	1888.0	2094.0	20.6	1.7	3.0	1.3

Table 5.1: Beam pipe dimensions used for the simulation. All dimensions are in cm. In brackets are the ending dimensions for the parts that have different thicknesses and radii at the starting and ending points.

Sector	**1**	**2**	**3**	**4**	**5**	**6**	**7**	**8**	**9**
Shape	Cylindrical	Cylindrical	Cylindrical	Conic	Cylindrical	Conic	Cylindrical	Conic	Cylindrical
Material	Beryllium(Be)	Aluminum(Al)	St. Steel	St. Steel	St. Steel	St. Steel	St. Steel	St. Steel	Copper(Cu)

Table 5.2: Additional details for the beam pipe sectors.

bigger z's, the upper cone of figure 5.2 represents the first instance and the lower cone the second one. Table 5.2 contains some additional details for the design of each sector.

5.2 The inner detector

The inner detector consists of three different parts. The Pixel Detectors, the Silicon Microchip Tracker (SCT) and the Transition Radiation Tracker (TRT). All parts are cylindrical so cylinders were used for the simulation design, in the same way as for the beam pipe design.

Figures 5.3 - 5.8 show simple designs of the bodies used in the simulation, the designs are not on scale and the hatched part of the figures shows the detector part.

5.2.1 Pixel Detectors

The pixel detector has a barrel part, of cylindrical shape, and two end caps, one on each side of the interaction point. The barrel has three layers and each end-cap has three disks. All parts are made of Silicon.

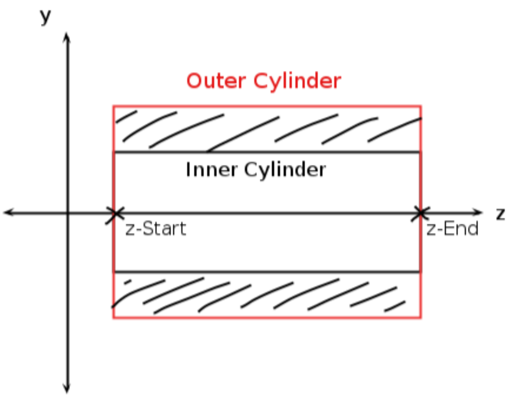

Figure 5.1: Example of the design of a cylindrical beam pipe sector.

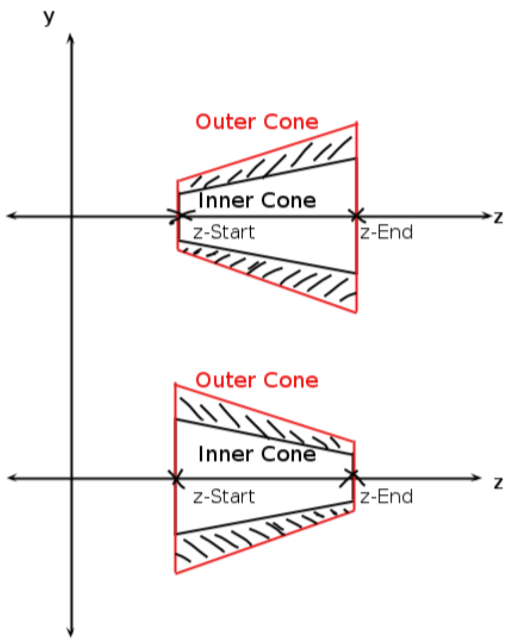

Figure 5.2: Example of the design of conic beam pipe sectors.

Each one of the parts of the detector is simulated to have a thickness of $0.06cm$ and be made of silicon (Si).

The barrel layers extend on the z-axis (along the beam line) for $|z| \leq 40.05cm$ and ,to achieve symmetry, are centred at the interaction point. So the face of the cylinder is positioned at $z = -40.05cm$. Details for the simulated barrel pixel detector are in table 5.3.

As said before, on each side of the interaction point, along the z-axis, there are three end-cap disks. Their thickness extends along z and they have a ring-like shape. Table 5.4 contains the information about the design of the end-cap disks. Face is the perpendicular to the z-axis circular plane that is closer to the interaction point for the positive-z disks and the one that is further form the interaction point for the negative-z disks. The numbering of the end-caps is done in a way that makes the disk pairs 1-2, 3-4 and 5-6 symmetrical with respect to the interaction point.

5.2.2 Silicon Microchip Tracker

The SCT also has a barrel part and an end-cap part. The barrel consists of four cylindrical layers and the in the end-cap region there are a total of 18 disks (9 on each side of the interaction point). Each one of the parts of the detector is simulated to have a thickness of $0.088cm$ and be made of silicon (Si).

The barrel layers extend on the z-axis (along the beam line) for $|z| \leq 74.9cm$

Barrel Layer	Length (z)	R
0	80.1	5.05
		5.11
1	80.1	8.85
		8.91
2	80.1	12.25
		12.31

Table 5.3: Pixel barrel detector details.

and ,to achieve symmetry, are centered at the interaction point. So the face of the cylinder is positioned at $z = -74.9cm$. Details for the simulated barrel SCT are in table 5.5.

On each side of the interaction point, along the z-axis, there are nine end-cap disks. Their thickness extends along z and they have a ring-like shape. Table 5.6 contains the information about the simulated end-cap disks. Face is the perpendicular to the z-axis circular plane that is closer to the interaction point for the positive-z disks and the one that is further form the interaction point for the negative-z disks. The numbers are assigned to the end-caps so that the symmetrical disk pairs are: 1-18, 2-17, 3-16, 4-15, 5-14, 6-13, 7-12, 8-11 and 9-10.

5.2.3 Transition Radiation Tracker

The barrel part of the Transition Radiation Tracker consists of three cylindrical modules on each side of the interaction point, and the first one has an inner and an outer module. These modules are simulated as cylinders made of Xenon. The specific dimensions that were used are shown in table 5.7. Face is the perpendicular to the z-axis circular plane that is closer to the interaction point for the positive-z cylinders and the one that is further form the interaction point for the negative-z cylinders. Studying the table, one can see that the barrel cylinders do not osculate and have varying distances from each other.

In each of the end-cap regions of the TRT there are 20 independent wheels. These wheels are of two different types, 12 of type-A and 8 of type-B. The difference between the two wheel types lies in the spacing of the straw layers that make up each wheel. For simplicity in the simulation all the wheels were considered identical and without in between spacing, and entirely made of Xenon. The total geometry was simulated as two hollow cylinders, one on each side of the interaction point. Details for the geometry of this parts are in table 5.8.

Disk	Face position (z)	Thickness(z)	R
1	-49.5	0.06	8.88
			14.96
2	49.44	0.06	8.88
			14.96
3	-58.0	0.06	8.88
			14.96
4	57.94	0.06	8.88
			14.96
5	-65.0	0.06	8.88
			14.96
6	64.94	0.06	8.88
			14.96

Table 5.4: Pixel detector End-cap details.

Barrel Layer	Length (z)	R
3	149.8	29.9
		29.988
4	149.8	37.1
		37.188
5	149.8	44.3
		44.388
6	149.8	51.4
		51.488

Table 5.5: SCT barrel detector details.

Disk	Face position (z)	Thickness(z)	R
1	-85.38	0.05	33.76
			56.0
2	-93.4	0.05	27.5
			56.0
3	-109.15	0.05	27.5
			56.0
4	-129.99	0.05	27.5
			56.0
5	-139.97	0.05	27.5
			56.0
6	-177.14	0.05	27.5
			56.0
7	-211.52	0.05	33.76
			56.0
8	-250.5	0.05	40.282
			45.53
9	-272.02	0.05	43.877
			56.0
18	85.33	0.05	33.76
			56.0
17	93.35	0.05	27.5
			56.0
16	109.1	0.05	27.5
			56.0
15	129.94	0.05	27.5
			56.0
14	139.92	0.05	27.5
			56.0
13	177.09	0.05	27.5
			56.0
12	211.47	0.05	33.76
			56.0
11	250.45	0.05	40.282
			45.53
10	271.97	0.05	43.877
			56.0

Table 5.6: SCT detector End-cap details.

Module Type	Face position(z)	Length (z)	R
Type-1 inner	40.0	31.21	56.3
	40.0		62.4
	-71.21		56.3
	-71.21		62.4
Type-1 outer	0.75	70.46	62.5
	0.75		69.4
	-71.21		62.5
	-71.21		69.4
Type-2	0.75	70.46	69.7
	0.75		86.0
	-71.21		69.7
	-71.21		86.0
Type-3	0.75	70.46	86.3
	0.75		106.6
	-71.21		86.3
	-71.21		106.6

Table 5.7: TRT barrel details.

Module Type	Face position(z)	Length (z)	R
Type A+B	84.8	186.2	64.4
	84.8		100.4
	-217.0		64.4
	-217.0		100.4

Table 5.8: TRT end-cap details.

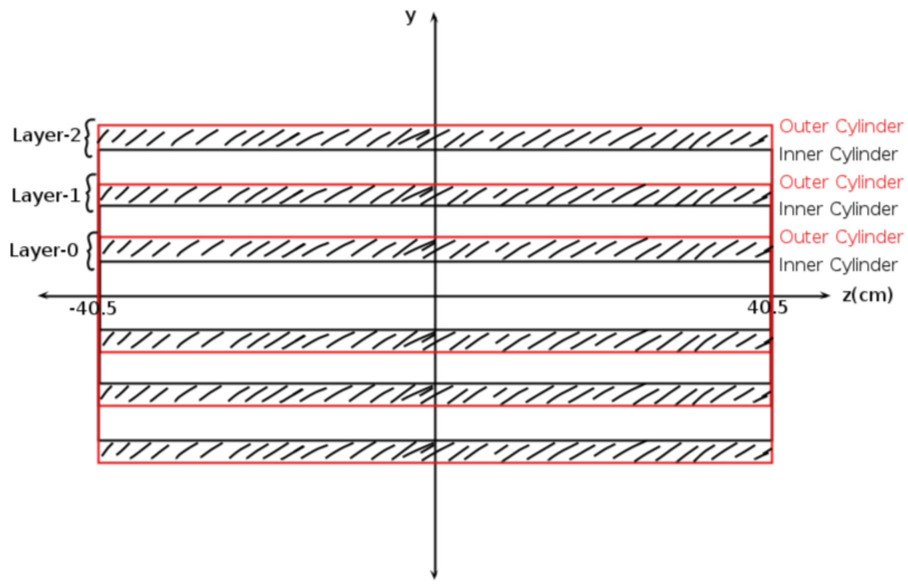

Figure 5.3: Figure of the barrel part of the pixel detector.

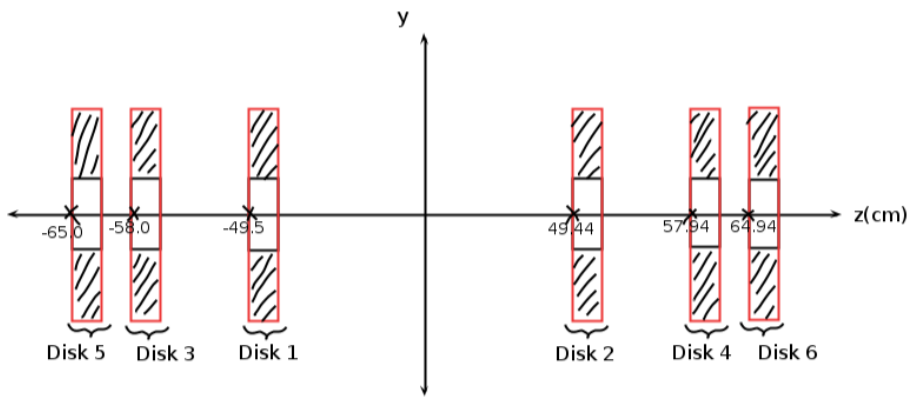

Figure 5.4: Figure of the end-cap part of the pixel detector outer cylinders are red and inner cylinders are black.

5.3 The calorimeters

The ATLAS calorimeters are:

1. Liquid Argon Electromagnetic Calorimeter
   - Two barrels (EMB).
   - Two end-cap wheels (EMEC).
2. Tile Calorimeter
   - One central barrel.
   - Two extended barrels, one on each side of the interaction point, along the z-axis.

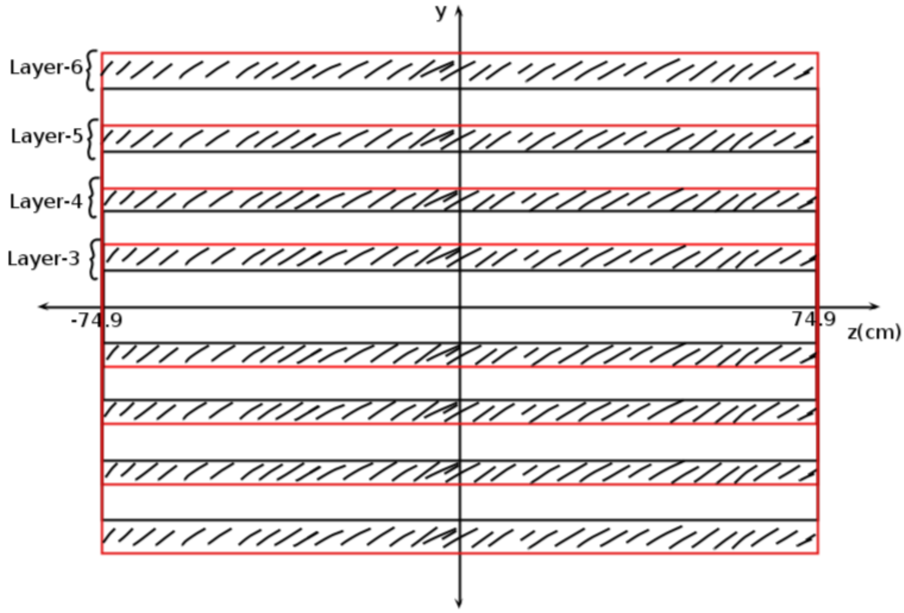

Figure 5.5: Figure of the barrel part of the SCT outer cylinders are red and inner cylinders are black.

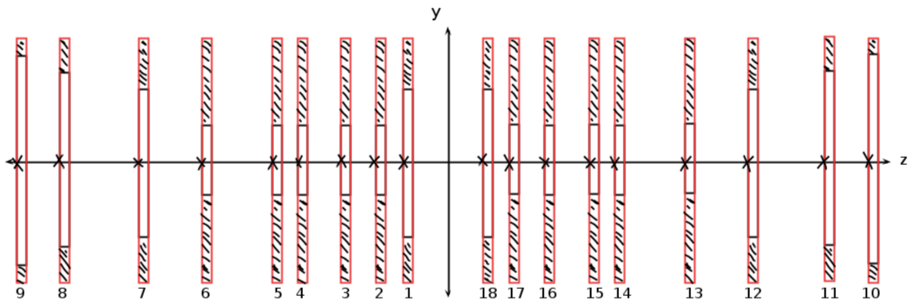

Figure 5.6: Figure of the end-cap part of the SCT outer cylinders are red and inner cylinders are black.

3. Hadronic End-Cap Calorimeters (HEC)

   - Four wheels.

4. Forward Calorimeters

   - Six forward calorimeter wheels (FCAL).
   - Two shielding plugs behind each of the third forward calorimeters.

The different parts of the calorimetry system was designed using cylinders, following the same principles as with the beam pipe parts simulation design. In all tables of this section (5.9-5.13) for each module in the radii column the first number is the inner radius and the one under it the outer radius.

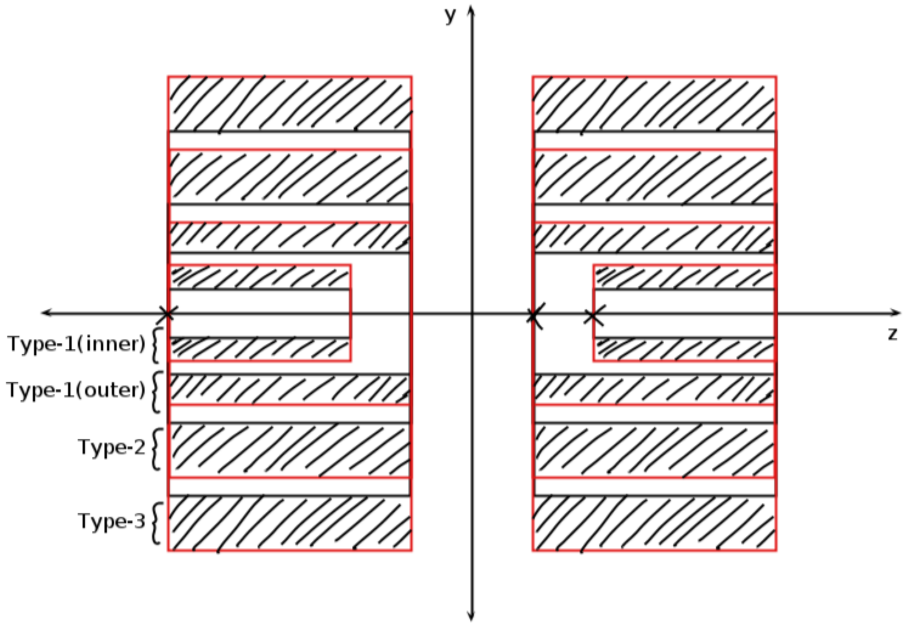

Figure 5.7: Figure of the barrel part of the TRT outer cylinders are red and inner cylinders are black.

5.3.1 LAr Electromagnetic Calorimeters

The detectors are made of two distinct devices, the calorimeter and the presampler. The barrel part consists of two half barrels each extended along the z-axis for $0.2cm < |z| < 320.2cm$. On the inside of the LAr EM calorimeter is the presampler layer. For the simulation three cylinders on each side of the interaction point were used to generate the desired geometry, which is shown in figure 5.9. The details for their definition in FLUKA are given in table 5.9. The calorimeter thickness (radial direction) is $60cm$ and the presampler thickness (radial direction) is $1.1cm$.

The end-cap section comprises two LAr Em end-cap wheels and two presampler end-cap wheels (all wheels are coaxial). Their thickness, respectively, is $63.0cm$ and $0.5cm$, and extends along z . Table 5.10 contains the information about the simulated end-cap wheels. Face is the perpendicular to the z-axis circular plane that is closer to the interaction point for the positive-z wheels and the one that is further form the interaction point for the negative-z wheels.

5.3.2 Tile Calorimeter

This part of the detector has three barrels and is made of steel. One is centered around the interaction point (central barrel) and extends for $|z| < 282.0cm$ and the other two are positioned on each side of the central barrel and extend along $321.0cm < |z| < 611.0cm$. All three barrels are coaxial and have thickness (radial

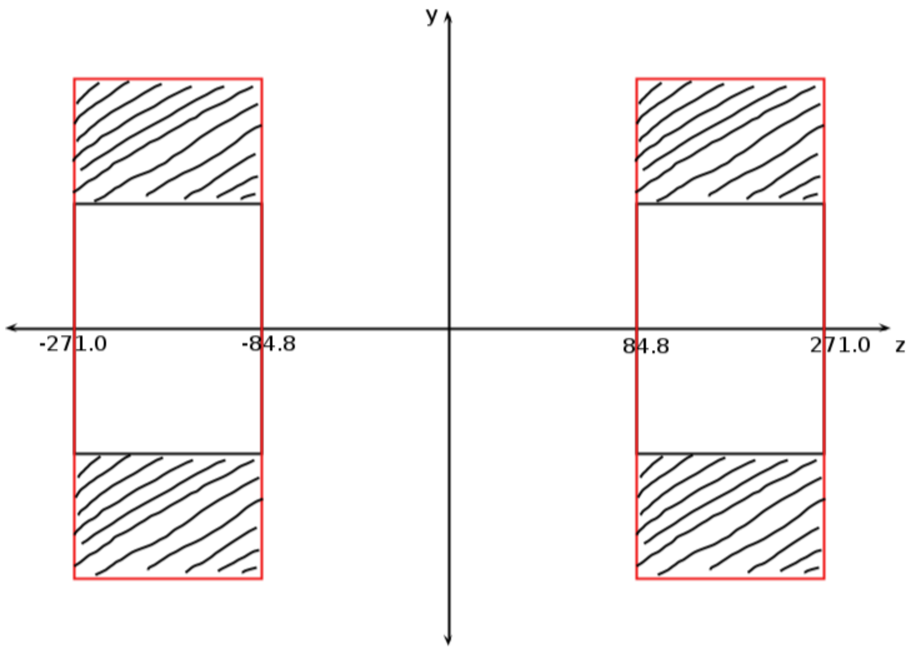

Figure 5.8: Figure of end-cap part of the TRT outer cylinders are red and inner cylinders are black.

direction) 201.2cm.

To simulate each barrel, two cylinders were used. Figure 5.11 is a sketch of the simulated geometry and table 5.11 contains the details for the definition of the bodies and regions used in FLUKA.

5.3.3 Hadronic End-Cap Calorimeters

There are two hadronic end-cap calorimeters, they are coaxial wheels, one on each side of the interaction point and they are both made of Copper(Cu). Front wheels are those closer to, and rear those farther from the interaction point. Those wheels are made of copper plates. The first nine plates of the front wheels have different thickness (radial dimension) from the rest, so two different sections must be used to simulate the front wheels. A sketch of the geometry is given in figure 5.12 and details for the bodies used in the simulation are in table 5.12. Due to requirements of the simulator some of the bodies have different dimensions than the part their name indicates they form, but in the definition of the regions the dimensions for each part are correct because of the use of multiple bodies. For example on the right section the B-cylinder bodies have length 81.65cm, while we need a part with length 53.6cm. Using not only B-cylinders, but also A-cylinders for the definition of the B-part of the front wheel the desired geometry is generated. This can be seen in the figure 5.12, where the A-cylinders for the front wheels are in black and the

Barrel Part	Face position(z)	Length (z)	R	Material
Left Main	-320.2	320.0	140.0 200.0	Lead
Left Presampler	-320.2	320.0	138.9 140.0	Argon
Right Main	0.2	320.0	140.0 200.0	Lead
Right Presampler	0.2	320.0	138.9 140.0	Argon

Table 5.9: Liquid Argon Electromagnetic Calorimeter barrel section details.

End-Cap Part	Face position(z)	Thickness (z)	R	Material
Left Main	-427.1	63.0	33.0 207.7	Lead
Left Presampler	-363.0	0.5	123.2 362.5	Argon
Right Main	364.1	63.0	33.0 207.7	Lead
Right Presampler	362.5	0.5	123.2 362.5	Argon

Table 5.10: Liquid Argon Electromagnetic Calorimeter end-cap section details.

B-cylinders in red, but the hatched parts that indicate the A-part (black) and the B-part (red) do not overlap.

5.3.4 Forward Calorimeters

In this section there are three forward calorimeters of different size, the first one is made of Copper and the other two of Tungsten. A sketch of the geometry is given in figure 5.13 and details for the bodies used in the simulation are in table 5.13.

5.4 The muon spectrometer

The Muon Spectrometer includes:

1. Monitored Drift Tube chambers (MDT)

2. Cathode Strip Chambers (CSC)

Barrel Part	Face position(z)	Length (z)	R
Central	-282.0	564.0	228.8
			430.0
Left Extebded	-611.0	290.0	228.8
			430.0
Right Extended	321.0	290.0	228.8
			430.0

Table 5.11: Tile Calorimeter details.

End-Cap Part	Face position(z)	Length (z)	R
First nine plates of	-455.75	28.05	37.2
front left wheel			203.0
Rest plates of	-509.35	81.65(53.6)	47.5
front left wheel			203.0
Rear left wheel	-609.5	96.1	47.5
			203.5
First nine plates of	427.7	28.05	37.2
front right wheel			203.0
Rest plates of	427.7(455.75)	81.65(53.6)	47.5
front right wheel			203.0
Rear right wheel	513.4	96.1	47.5
			203.5

Table 5.12: Hadronic End-Cap Calorimeter details. The numbers outside the parentheses are the dimensions of the bodies in the last column and the numbers inside the parentheses are the final dimensions of the calorimeter region for the particular part defined.

Calorimeter part	Face position(z)	Length (z)	R	Material
Forward Calorimeter 1 Left	-515.4	44.41	7.23 44.94	Copper
Forward Calorimeter 2 Left	-561.12	44.41	7.88 44.94	Tungsten
Forward Calorimeter 3 Left	-609.33	44.41	8.57 44.97	Tungsten
Forward Calorimeter 1 Right	470.99	44.41	7.23 44.94	Copper
Forward Calorimeter 2 Right	516.71	44.41	7.88 44.94	Tungsten
Forward Calorimeter 3 Right	564.92	44.41	8.57 44.97	Tungsten

Table 5.13: Forward Calorimeter details.

Sector	Azimuthal Position (degrees)
1 - Large	0
2 - Small	22.5
3 - Large	45
4 - Small	67.5
5 - Large	90
6 - Small	112.5
7 - Large	135
8 - Small	157.5
9 - Large	180
10 - Small	202.5
11 - Large	225
12 - Small	247.5
13 - Large	270
14 - Small	292.5
15 - Large	315
16 - Small	337.5

Table 5.14: MDT sectors' azimuthal position.

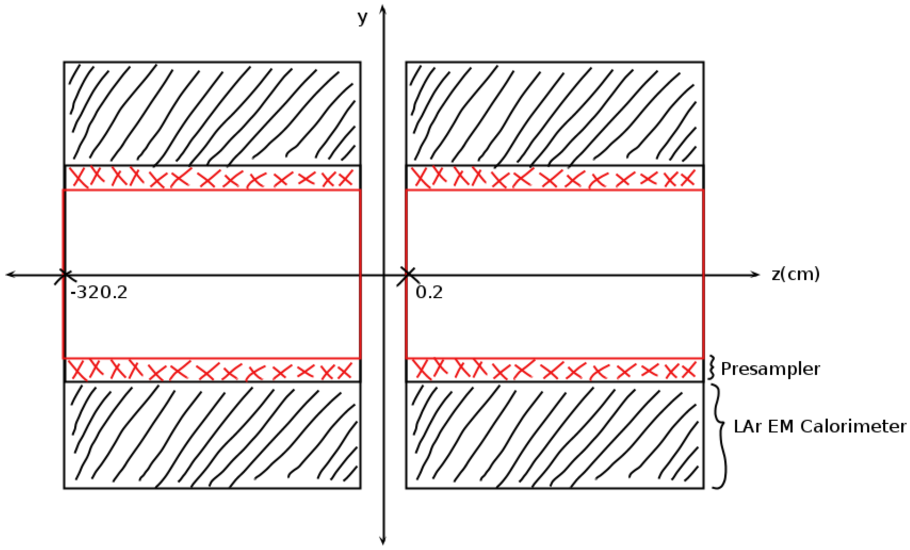

Figure 5.9: Figure of the barrel LAr E/M Calorimeter.

3. Resistive Plate Chambers (RPC)

4. Thin Gap Chambers (TGC)

The layout of the Muon spectrometer is shown in figures 5.15, 5.16, 5.17, 5.18 and 5.19.

5.4.1 Monitored Drift Tube Chambers - MDT

The MDT chambers form two distinct parts of the muon spectrometer, the barrel part and the end-cap part.

Barrel

The barrel chambers are of cuboid shape and cylindrically arranged in three layers around the beam axis. To simulate each one of them six PLA bodies were used. There are three main sets of chambers arranged in sectors around the beam line:

1. Barrel Inner (BI)

2. Barrel Middle (BM)

3. Barrel Outer (BO)

There is an auxiliary set of chambers, the BEE (Barrel End-cap Extra) chambers. They are installed on the cryostats of the end-cap toroids and are constructed like barrel chambers, although they serve in the end-cap system.

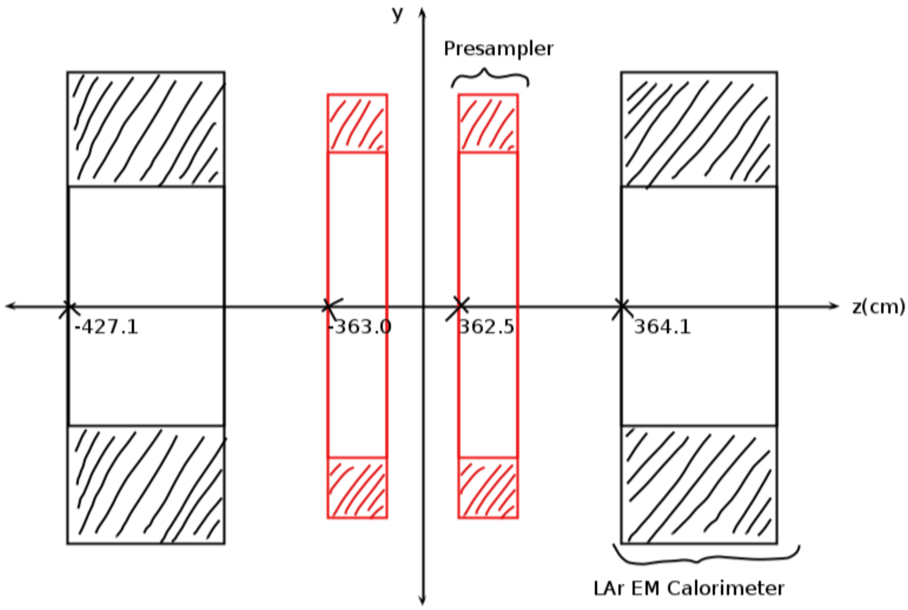

Figure 5.10: Figure of the end-caps of the LAr E/M Calorimeter.

Each layer is split into 16 sectors, 8 with large and 8 with small modules. The small and large sectors alternate along the azimuthal direction. Even numbered sectors have small modules and odd numbered sectors have large modules. The length of the modules lies in the z-direction, their hight along the radial ($R-$) direction and their width along the azimuthal ($\phi-$) direction. Figure 5.15 is a rough and not on scale representation of the MDT barrel modules along with the RPCs that complement some of them, the numbers indicate the sectors. In this figure starting from the interaction point (origin of the coordinate system) and moving outward the layer succession is: BOS, BOL, BML, BMS, BOL and BOS. The hatched modules are those that differ from the rest modules of the same layer, there are more details in the following sections.

<u>Barrel Inner Small</u>

All sectors are the same. Each consists of 7 standard and 1 special chambers. For simplicity, and because the space between successive chambers is small compared to their length, it is ignored and the chambers are considered to be back to back.
The dimension calculations are the following:

- A standard chamber's length is $91.6cm$, so the standard module that has 7 successive chambers is: $7 \cdot 91.6cm = 641.2cm$ long.
- A standard chamber has 2 layers of 4 tubes separated by a $6.5cm$ spacer so the standard module's height is: $2layers \cdot 4^{tubes}/_{layer} \cdot 30^{mm}/_{tube} + 65mm = 24.65cm$.

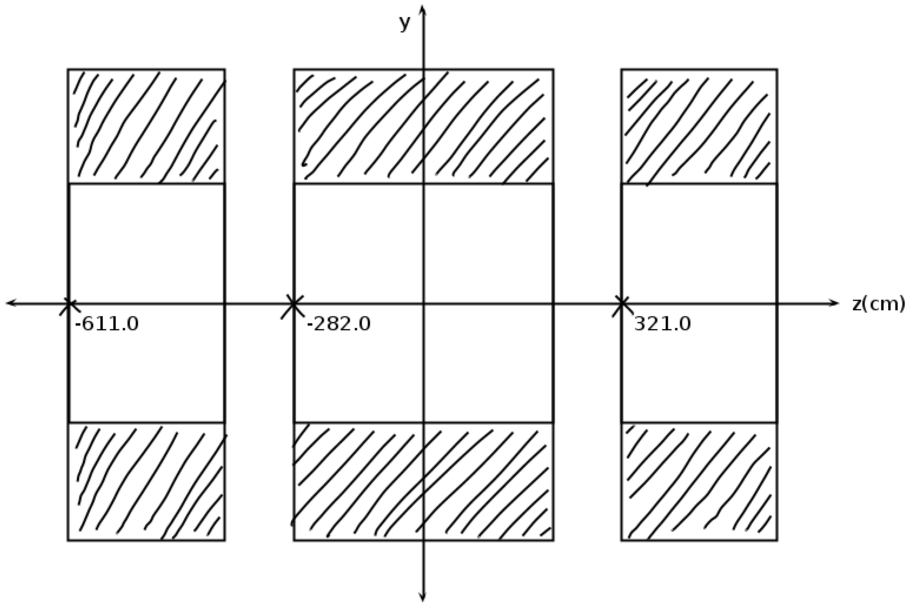

Figure 5.11: Figure of the Tile Calorimeter.

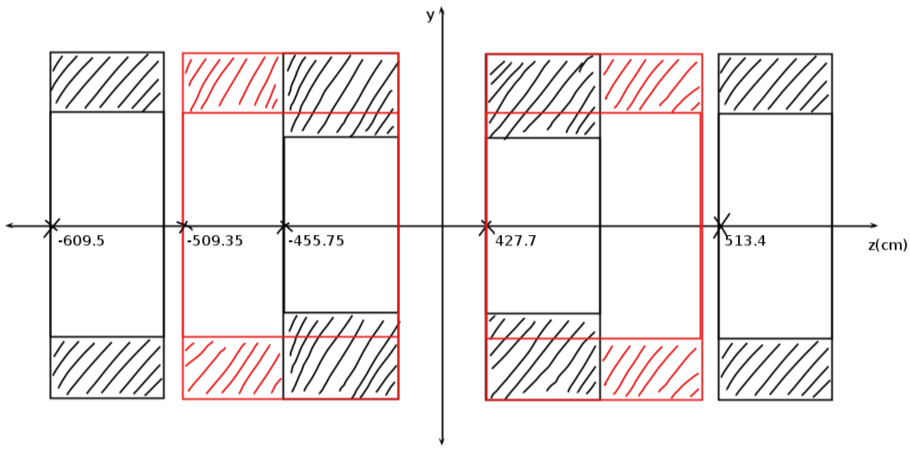

Figure 5.12: Figure of the Hadronic End-Cap Calorimeter.

- A special chamber has 1 layer of 3 tubes so the special module's height is: $1layer \cdot 3^{tubes}/_{layer} \cdot 30^{mm}/_{tube} = 9.0cm$.

Module details are given in table 5.15.

Barrel Inner Large - Standard Modules

Sectors 1-9 and 13 have standard BIL modules, while sectors 11 and 15 are different. Each standard module consists of 6 standard chambers. For simplicity, and because the space between successive chambers is small compared to their length, it is ignored and the chambers are considered to be back to back.

The dimension calculations are the following:

- A standard chamber's length is $109.6cm$, so the standard module that has 6

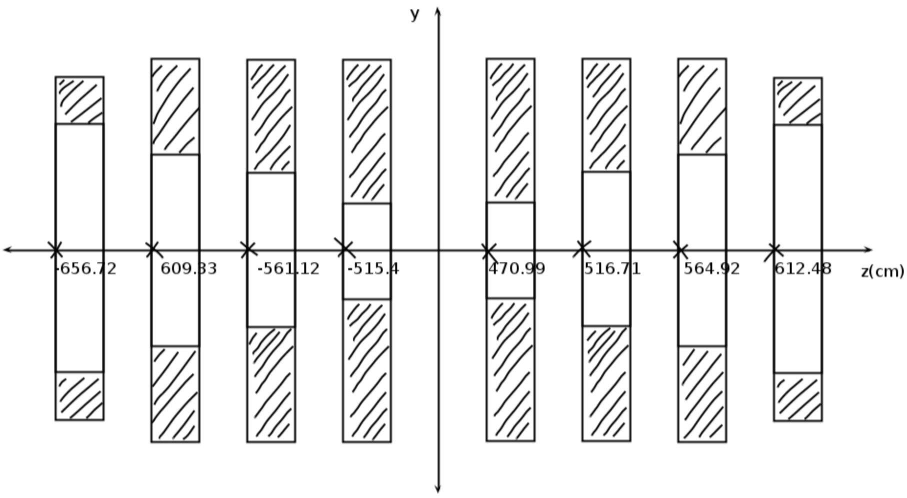

Figure 5.13: Figure of the Forward Calorimeters.

successive chambers is: $6 \cdot 109.6cm = 657.6cm$ long.

- A standard chamber has 2 layers of 4 tubes separated by a $17.0cm$ spacer so the standard module's height is: $2layers \cdot 4^{tubes}/_{layer} \cdot 30^{mm}/_{tube} + 170mm = 41.0cm$.

Module details are given in table 5.16.

Barrel Inner Large - Special Modules

Sectors 11 and 15 are different than the rest because of their position on the feet and the rails of the detector. There are two types of special modules BIMs and BIRs. Each sector has two BIMs and two BIRs (one on each side of the interaction point). These modules are not in the azimuthal position dictated by the sector they belong to, but are slightly moved to the side, as shown in table 5.26.

For simplicity, and because the space between successive chambers is small compared to their length, it is ignored and the chambers are considered to be back to back.

The dimension calculations are the following:

- A standard chamber's length is $109.6cm$, so the standard module that has 5 successive chambers is: $5 \cdot 109.6cm = 548.0cm$ long.

- A standard chamber has 2 layers of 4 tubes separated by a $17.0cm$ spacer so the standard module's height is: $2layers \cdot 4^{tubes}/_{layer} \cdot 30^{mm}/_{tube} + 170mm = 41.0cm$.

Module details are given in tables 5.17 and 5.18.

Barrel Middle Small - Standard Modules

Sectors 2-10 and 16 have standard BIL modules, while sectors 12 and 14 are different. Each standard module consists of 6 standard chambers. After very two chambers there is a gap of $30cm$ which is too big not to be considered, the rest of the spaces are small and not taken into consideration. So each sector is simulated to have three identical modules, every module is made of two chambers.
The dimension calculations are the following:

- A standard chamber's length is $149.7cm$, so the standard module that has 2 successive chambers is: $2 \cdot 149.7cm = 299.4cm$ long.
- A standard chamber has 2 layers of 3 tubes separated by a $17.0cm$ spacer so the standard module's height is: $2layers \cdot 3^{tubes}/_{layer} \cdot 30^{mm}/_{tube} + 170mm = 35.0cm$.

Module details are given in table 5.19. Note that in the third column the total length of all the modules, with the spaces in between, is given.

Barrel Middle Small - Special Modules

Sectors 12 and 14 are different than the rest because of their position on the feet of the detector. The special modules are referred to as BMFs (Barrel Middle Feet). Between successive chambers there is a gap of $120cm$ which is too big not to be considered. So each sector is simulated to have three identical modules, every module is made of one chamber.
The dimension calculations are the following:

- A standard chamber's, and a standard module's, length is $193.7cm$.
- A standard chamber has 2 layers of 3 tubes separated by a $17.0cm$ spacer so the standard module's height is: $2layers \cdot 3^{tubes}/_{layer} \cdot 30^{mm}/_{tube} + 170mm = 35.0cm$.

Module details are given in table 5.20. Note that in the third column the total length of all the modules, with the spaces in between, is given.

Barrel Middle Large

All sectors have standard BML modules. Each standard module consists of 6 chambers. There are two types of chambers that differ only in their length, so in the simulation every sector has only one module that is as long as the sum of the lengths of the individual chambers.
For simplicity, and because the space between successive chambers is small compared to their length, it is ignored and the chambers are considered to be back to back.
The dimension calculations are the following:

- Each module has one standard chamber of length $168.0cm$ and 5 standard chambers with length $144.0cm$, so the standard module is: $2 \cdot 5 \cdot 144.0cm + 168.0cm = 888.0cm$ long.

- All chambers have 2 layers of 3 tubes separated by a $31.7cm$ spacer so the standard module's height is: $2layers \cdot 3^{tubes}/_{layer} \cdot 30^{mm}/_{tube} + 317mm = 49.7cm$.

Module details are given in table 5.21.

Barrel Outer Small - Standard

Sectors 2-10 and 16 have standard BOS modules, while sectors 12 and 14 are different. Each standard module consists of 6 standard chambers.

For simplicity, and because the space between successive chambers is small compared to their length, it is ignored and the chambers are considered to be back to back.

The dimension calculations are the following:

- A standard chamber's length is $217.7cm$, so the standard module that has 6 successive chambers is: $6 \cdot 217.7cm = 1306.2cm$ long.

- A standard chamber has 2 layers of 3 tubes separated by a $31.7cm$ spacer so the standard module's height is: $2layers \cdot 3^{tubes}/_{layer} \cdot 30^{mm}/_{tube} + 317mm = 49.7cm$.

Module details are given in table 5.22.

Barrel Outer Small - Special

Sectors 12 and 14 are different than the rest because of their position on the feet of the detector. The special modules are referred to as BOFs and BOGs. Also modules of sector 14 have one less chamber than those of sector 12.

For simplicity, and because the space between successive chambers is small compared to their length, it is ignored and the chambers are considered to be back to back.

The dimension calculations are the following:

- Sector 12 has 5 chambers of length $121.6cm$, 2 chambers of length $217.7cm$, 1 chamber of length $144.0cm$ and 1 chambers of length $64.1cm$ so the sector 12 special module is: $5 \cdot 121.6cm + 2 \cdot 217.7cm + 144.0cm + 64.1cm = 1251.5cm$ long.

- Sector 14 has 4 chambers of length $121.6cm$, 2 chambers of length $217.7cm$, 1 chamber of length $144.0cm$ and 1 chambers of length $64.1cm$ so the sector 12 special module is: $4 \cdot 121.6cm + 2 \cdot 217.7cm + 144.0cm + 64.1cm = 1129.9cm$ long.

- All chambers have 2 layers of 3 tubes separated by a $31.7cm$ spacer so the all modules' height is: $2layers \cdot 3^{tubes}/_{layer} \cdot 30^{mm}/_{tube} + 317mm = 49.7cm$.

Module details are given in table 5.23.

Barrel Outer Large

All sectors have standard BOL modules. Each standard module consists of 6 chambers.
For simplicity, and because the space between successive is small compared to their length, it is ignored and the chambers are considered to be back to back.
The dimension calculations are the following:

- A chamber's length is $217.7cm$, so the module that has 6 successive chambers is: $6 \cdot 217.7cm = 1306.2cm$ long.

- All chambers have 2 layers of 3 tubes separated by a $31.7cm$ spacer so the standard module's height is: $2layers \cdot 3^{tubes}/_{layer} \cdot 30^{mm}/_{tube} + 317mm = 49.7cm$.

Module details are given in table 5.24.

Barrel End-cap Extra

All sectors have standard BEE modules. Each standard module consists of 2 chambers.
For simplicity, and because the space between successive is small compared to their length, it is ignored and the chambers are considered to be back to back.
The dimension calculations are the following:

- A chamber's length is $145.7cm$, so the module that has 2 successive chambers is: $2 \cdot 145.7cm = 291.4cm$ long.

- All chambers have 1 layer of 4 tubes so the modules' height is: $1layer \cdot 4^{tubes}/_{layer} \cdot 30^{mm}/_{tube} = 12.0cm$.

Module details are given in table 5.25.

Using the details for each module as presented above and taking into account the geometric characteristics of the detector layout, formulas were extracted for the calculation of the dimensions of the respective bodies, as described in Appendix I. [2]

[2] The calculations were performed using matlab, with double precision calculations, and LibreOffice Calc.

Sector	Chamber	Length(z)	Radial Position	Height(R)	Width(ϕ)	R_i	R_o
2-16	1-7	641.2	455.0	24.65	182.0	442.675	467.325
	8	49.6	462.0	9.0	100.0	457.5	466.5

Table 5.15: Barrel Inner Small module details.

Sector	Chamber	Length(z)	Radial Position	Height(R)	Width(ϕ)	R_i	R_o
1-9,13	1-6	657.6	494.9	41.0	282.0	474.4	515.5

Table 5.16: Barrel Inner Large standard module details for sectors 1-9 and 13.

Sector	Chamber	Length(z)	Radial Position	Height(R)	Width(ϕ)	R_i	R_o
11, 15	1-5	548.0	537.3	41.0	168.5	516.8	557.8

Table 5.17: Barrel Inner Middle, Large special module details for sectors 11 and 15.

Sector	Chamber	Length(z)	Radial Position	Height(R)	Width(ϕ)	R_i	R_o
11, 15	1-6	549.6	605.6	41.0	168.5	585.1	626.1

Table 5.18: Barrel Inner Rail, special Large module details for sectors 11 and 15.

Sector	Chamber	Length(z)	Radial Position	Height(R)	Width(ϕ)	R_i	R_o
2-10,16	1-6	958.2	809.5	35.0	322.0	827.0	792.0

Table 5.19: Barrel Middle Small standard module details, for sectors 2-10 and 16.

Sector	Chamber	Length(z)	Radial Position	Height(R)	Width(ϕ)	R_i	R_o
12, 14	1-3	821.1	809.5	35.0	322.0	827.0	792.0

Table 5.20: Barrel Middle Feet, Small special module details, for sectors 12 and 14 .

Sector	Chamber	Length(z)	Radial Position	Height(R)	Width(ϕ)	R_i	R_o
1-15	1-6	888.0	713.9	49.7	370.0	689.05	738.75

Table 5.21: Barrel Middle Large module details.

Sector	Chamber	Length(z)	Radial Position	Height(R)	Width(ϕ)	R_i	R_o
2-10,16	1-6	1306.2	1056.9	49.7	392.0	1032.05	1081.75

Table 5.22: Barrel Outer Small standard module details, for sectors 2-10 and 16.

Sector	Chamber	Length(z)	Radial Position	Height(R)	Width(ϕ)	R_i	R_o
12	1-4, 1-5	1251.5	1056.9	49.7	392.0	1042.65	1081.75
14	1-4, 1-4	1129.9	1056.9	49.7	392.0	1042.65	1081.75

Table 5.23: Barrel Outer Feet, Small special module details, for sectors 12 and 14 .

Sector	Chamber	Length(z)	Radial Position	Height(R)	Width(ϕ)	R_i	R_o
1-15	1-6	1306.2	950.0	49.7	511.0	925.15	974.85

Table 5.24: Barrel Outer Large module details.

Sector	Chamber	Length(z)	Radial Position	Height(R)	Width(ϕ)	R_i	R_o
2-16	1-2	291.4	441.5	12.0	106.0	435.5	447.5

Table 5.25: Barrel End-cap Extra module details.

End Caps

The end-cap chambers have prismoid shape, most with two of the faces being trapezoids and some having only parallelogram faces. They are cylindrically arranged in three main layers and an extra layer, around the beam axis. To simulate them a combination of cylinders (RCC bodies) and planes (PLA bodies) were used. Each module is positioned to be parallel to the $z = 0$ plane. All the modules of a layer have the same thickness and z-position, so one cylinder for all modules and 4 planes for each one can produce the desired geometry. Also the geometry on the left of the interaction point is a mirrored copy of that on the right, so for modules belonging to the same sector of the same layer, but are on different sides of th interaction point, the same planes can be used.

1. End-Cap Inner (EI)
2. End-Cap Middle (EM)
3. End-Cap Outer (EO)
4. End-Cap Extra (EE)

Each layer is split into 16 sectors, 8 with large and 8 with small modules. The small and large sectors alternate along the azimuthal direction. Even numbered sectors have small modules and odd numbered sectors have large modules. The length

Sector	Module	Azimuthal Position (degrees)
11	BIM	213.75
15	BIM	326.25
11	BIR	236.25
15	BIR	303.75

Table 5.26: 11 and 15 sectors' azimuthal position for modules BIM and BIR.

of the modules lies in the z-direction, their hight along the radial (R-) direction and their width along the azimuthal ($\phi-$) direciton.

For each sector the positions and dimensions of each module were calculated as presented in this section. In figure 5.18 a standard layout of a large layer end cap modules is presented for the small sector layers this layout is rotated by 22.5 deg around the origin of the coordinate system (2-D). This figure is valid for all but one end cap layers. The inner large end cap layer has some special modules in sectors 11, 13 and 15 because they are positioned around the feet of the detector.

The height of each simulated part is calculated as the difference between the radial position of the center of tube that is closer to the beam axis (inner radius R_i) and that of the center of the tube farthest from the beam axis (outer radius R_o).

End-Cap Inner Small

All sectors are the same. Each consists of 2 standard chambers placed along the radial direction. For simplicity, and because the space between successive chambers is small compared to their height, it is ignored and the chambers one is considered to be directly above the previous.
The dimension calculations are the following:

- A standard chamber has 2 layers of 4 tubes seperated by a $12.1cm$ spacer so the standard module's length is: $2layers \cdot 4^{tubes}/_{layer} \cdot 30^{mm}/_{tube} + 121mm = 36.1cm$.

Module details are given in table 5.27.

End-Cap Inner Large - Standard and Special Modules

Chambers 1-3 are the same for all sectors. The first two chambers are prismoids with trapezoidal faces and the third is a orthogonal parallelepiped (the innermost and outermost tubes have the same length). Chambers 1-2 are simulated together as a bigger one and the third is placed directly above them without taking into account the distance between succesive chambers along the radial direciton. The 4$^{\text{th}}$ chamber is a standard one for sectors 1-9. The radial distance between the 3$^{\text{rd}}$ and 4$^{\text{th}}$ chambers is $3cm$ and is simulated as is. Chamber 4 is different for sectors 11-15. In sector 13 it has standard shape but its width is slightly smaller than that of the standard 4$^{\text{th}}$ chambers. Because sectors 11 and 15 are on the feet of the detector the 4$^{\text{th}}$ chamber is devided radialy in three parts, each of those has different height and different widths. Also for sectors 13 and 15 chamber 4 is not centered.
The dimension calculations are the following:

- All standard chambers have 2 layers of 4 tubes seperated by a $12.1cm$ spacer so the standard module's length is: $2layers \cdot 4^{tubes}/_{layer} \cdot 30^{mm}/_{tube} + 121mm =$

$36.1cm$.

Module details are given in table 5.28.

End-Cap Extra Small

All sectors are the same. Each consists of 2 standard chambers placed along the radial direction. For simplicity, and because the space between successive chambers is small compared to their height, it is ignored and the chambers one is considered to be directly above the previous.
The dimension calculations are the following:

- A standard chamber has 2 layers of 3 tubes seperated by a $12.1cm$ spacer so the standard module's length is: $2layers \cdot 3^{tubes}/_{layer} \cdot 30^{mm}/_{tube} + 121mm = 30.1cm$.

Module details are given in table 5.33.

End-Cap Extra Large

All sectors are the same. Each consists of 2 standard chambers placed along the radial direction. For simplicity, and because the space between successive chambers is small compared to their height, it is ignored and the chambers one is considered to be directly above the previous.
The dimension calculations are the following:

- A standard chamber has 2 layers of 3 tubes seperated by a $12.1cm$ spacer so the standard module's length is: $2layers \cdot 3^{tubes}/_{layer} \cdot 30^{mm}/_{tube} + 121mm = 30.1cm$.

Module details are given in table 5.34.

End-Cap Middle Small

All sectors are the same. Each consists of 5 standard chambers placed along the radial direction. For simplicity, and because the space between successive chambers is small compared to their height, it is ignored and the chambers one is considered to be directly above the previous.
The dimension calculations are the following:

- A standard chamber has 2 layers of 3 tubes seperated by a $17.0cm$ spacer so the standard module's length is: $2layers \cdot 3^{tubes}/_{layer} \cdot 30^{mm}/_{tube} + 170mm = 35.0cm$.

Module details are given in table 5.29.

End-Cap Middle Large

All sectors are the same. Each consists of 5 standard chambers placed along the

radial direction. For simplicity, and because the space between successive chambers is small compared to their height, it is ignored and the chambers one is considered to be directly above the previous.
The dimension calculations are the following:

- A standard chamber has 2 layers of 3 tubes seperated by a 17.0cm spacer so the standard module's length is: $2layers \cdot 3^{tubes}/_{layer} \cdot 30^{mm}/_{tube} + 170mm = 35.0cm$.

Module details are given in table 5.30.

End-Cap Outer Small

All sectors are the same. Each consists of 6 standard chambers. Chambers 1-3 form one part of the end-cap placed along the radial direction and chambers 4-6, also placed one above the other, form a second part. The two parts are positioned at different points on the z-axis and have different lenghts. For simplicity, and because the space between successive chambers is small compared to their height, it is ignored and the chambers one is considered to be directly above the previous.
The dimension calculations are the following:

- For the first part a standard chamber has 2 layers of 3 tubes seperated by a 12.1cm spacer, so the standard module's length is: $2layers \cdot 3^{tubes}/_{layer} \cdot 30^{mm}/_{tube} + 121mm = 30.1cm$.
- For the second part a standard chamber has 2 layers of 3 tubes seperated by a 17.0cm spacer, so the standard module's length is: $2layers \cdot 3^{tubes}/_{layer} \cdot 30^{mm}/_{tube} + 170mm = 35.0cm$.

Module details are given in table 5.31.

End-Cap Outer Small

All sectors are the same. Each consists of 6 standard chambers. Chambers 1-3 form one part of the end-cap placed along the radial direction and chambers 4-6, also placed one above the other, form a second part. The two parts are positioned at different points on the z-axis and have different lenghts. For simplicity, and because the space between successive chambers is small compared to their height, it is ignored and the chambers one is considered to be directly above the previous.
The dimension calculations are the following:

- For the first part a standard chamber has 2 layers of 3 tubes seperated by a 12.1cm spacer, so the standard module's length is: $2layers \cdot 3^{tubes}/_{layer} \cdot 30^{mm}/_{tube} + 121mm = 30.1cm$.

Sector	Chamber	Face position(z)	Length(z)	W_i	W_o	Height	R_i	R_o
2-16	1-2	708.5	36.1	92.46	163.38	234.0	213.6	447.6

Table 5.27: End-Cap Inner Small module details.

Sector	Chamber	Face position(z)	Length(z)	W_i	W_o	Height	R_i	R_o
1-15	1-2	749.45	36.1	134.79	244.13	216.0	212.1	428.1
1-15	3	749.45	36.1	208.18	208.18	24.0	428.1	452.1
1-9	4	749.45	36.1	257.6	338.48	162.0	455.2	617.2
13	4	749.45	36.1	242.6	326.49	162.0	455.2	617.2
11, 15	4a	749.45	36.1	71.89	80.8	18.0	455.2	473.2
11, 15	4b	749.45	36.1	151.27	187.21	72.0	473.2	545.2
11, 15	4c	749.45	36.1	235.14	271.08	72.0	545.2	617.2

Table 5.28: End-Cap Inner Large module details.

- For the second part a standard chamber has 2 layers of 3 tubes seperated by a 17.0cm spacer, so the standard module's length is: $2layers \cdot 3^{tubes}/_{layer} \cdot 30^{mm}/_{tube} + 170mm = 35.0cm$.

Module details are given in table 5.32.

5.4.2 Cathode Strip Chambers - CSC

The CSC modules have prismoid shape and are arranged in 16 sectors around the beam line. Figure 5.14 shows the layout of all 32 (16 for positive$z$ and 16 for negative z) parts. There are two types of modules, that for convenience in this study are referred to as $(2k)$-modules and $(2k-1)$-modules, the $(2k)$ are arranged in even numbered sectors and $(2k-1)$ in odd numbered sectors. All modules are tilted at an angle $|\omega| = 11.9^o$ of the $z = 0$ plane, with the top part (highest along R) being closer to the $z = 0$. For the design of each CSC six PLA bodies were used. All modules of the same type started as one, centered around the origin of the coordinate system. After that they were positioned as desired via the following process:

1. Vector multiplication with the appropriate rotation matrix for the ω tilt.

2. Vector multiplication with the appropriate transfer matrix for the $R-$positioning.

Sector	Chamber	Face position(z)	Length(z)	W_i	W_o	Height	R_i	R_o
2-16	1-5	1370.3	35.0	75.41	376.14	960.0	173.5	1133.5

Table 5.29: End-Cap Middle Small module details.

Sector	Chamber	Face position(z)	Length(z)	W_i	W_o	Height	R_i	R_o
1-15	1-5	1429.4	35.0	110.83	594.59	936.0	173.5	1109.5

Table 5.30: End-Cap Middle Large module details.

Sector	Chamber	Face position(z)	Length(z)	W_i	W_o	Height	R_i	R_o
2-16	1-3	2268.75	30.1	131.96	263.03	432.0	293.5	725.5
2-16	4-6	2107.1	35.0	245.97	405.76	528.0	676.0	1204.0

Table 5.31: End-Cap Outer Small module details.

Sector	Chamber	Face position(z)	Length(z)	W_i	W_o	Height	R_i	R_o
1-15	1-3	2218.95	30.1	193.2	411.87	432.0	298.5	730.5
1-15	4-6	2065.7	35.0	369.93	624.54	504.0	652.0	1156.0

Table 5.32: End-Cap Outer Large module details.

Sector	Chamber	Face position(z)	Length(z)	W_i	W_o	Height	R_i	R_o
2-16	1-2	1012.55	30.1	204.68	291.75	288.0	587.0	875.0

Table 5.33: End-Cap Extra Small module details.

Sector	Chamber	Face position(z)	Length(z)	W_i	W_o	Height	R_i	R_o
1-15	1-2	1117.15	30.1	298.04	431.34	264.0	540.0	804.0

Table 5.34: End-Cap Extra Large module details.

Sector	Module	Radial extent	Maximum Width	Minimum Width	Thickness	$\|z\|-$position	R_o
2-16	Small	109.73	73.55	40.29	27.0	686.9	208.1
1-15	Large	114.96	113.95	61.01	27.0	777.2	208.1

Table 5.35: CSC small and large module details. The table contains the simulated dimensions of the modules, rows 3-6, and the outer radius and $z-$position of modules after they are placed in the desired place and given the 11.9^o tilt.

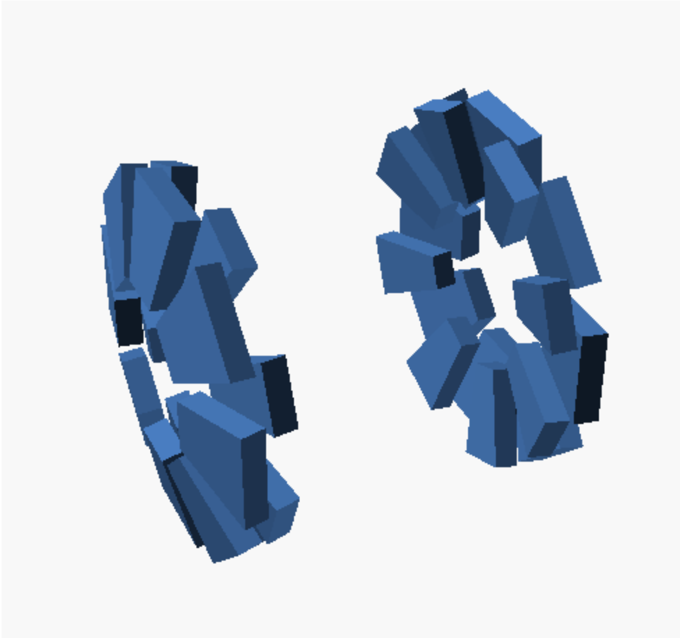

Figure 5.14: $3D$ figure of the CSC layout.

3. Vector multiplication with the appropriate rotation matrix for the positioning at sectors.

4. Vector multiplication with the appropriate transfer matrix for the $z-$positioning.

5.4.3 Resistive Plate Chambers - RPC

The RPCs complement the middle and outer barrel MDT modules. They are thin ($R-$direction) cuboids, positioned to be parallel and within a distance of $10cm$ from the MDT module they accompany. Also the rest of their dimensions matches those of the MDT module. All sectors of the middle layer MDTs have two layers of RPCs, one under (1^{st} layer) and one over (2^{nd} layer) the MDTs. The small sectors of the outer layer barrel MDTs have one RPC layer under the MDT modules and the large sectors have one layer over the MDT modules. All RPC modules have the same thickness, $H = 1.28cm$. They were simulated using six PLA bodies for each one. In table 5.36 only the inner radius is given. They share the rest of the defining parameters, besides the thickness, with the MDT chamber they complement.

5.4.4 Thin Gap Chambers - TGC

There are five layers of TGCs on each side of the interaction point, so ten layers in total and they can be either double-gap or triple-gap chambers.

- Two layers are in the region of the End-Cap Inner layer of the MDTs. The

Complemented MDT	Layer	R_i
BMS	Under	780.72
	Over	837.0
BMF	Under	780.2
	Over	837.0
BML	Under	677.77
	Over	748.75
BOS	Under	1020.77
BOFG	Under	1031.37
BOL	Over	984.85

Table 5.36: Inner radius position of RPC modules.

Layer	Chamber type	R_i	R_o	Thickness (z)	$\|z\|-$position
FI	doublet	217.0	443.4	10	693.3-703.3
EI	doublet	470.0	619.0	10	732.0-742.0
M1	triplet	190.0	1068.2	15	1336.5-1351.5
M2	doublet	252.6	1191.7	10	1468.3-1478.3
M3	doublet	261.0	1191.7	10	1510.3-1520.3

Table 5.37: Details for the desing of the TGC layout.

first is in front of the small MDT EI modules while the other is above the small modules and in front of the large ones. These two layers are respectively named FI and EI and are both made of doublets.

- One layer is in the region of the End-Cap Middle layer of the MDTs and in front of the small end-cap MDT modules, the M1 layer. It is made of triplets.
- Two layers are in the region of the End-Cap Middle MDT layer and on the back of the large end-cap MDT modules, the M2 and M3 layers. They are made of double-gap layers.

FI and EI grouped together make up the inner (I) layer and M1, M2 and M3 the middle (M) layer. The difference of the two types of chambers is that the double-gaps (doublets) have two gas gaps while the triple-gaps (triplets) have tree. The TGCs, when assembled and put in position, have, approximately, the shape of a thin disk. The M1, M2 and M3 layers have two parts, an inner and an outer one (placed consecutively on the $R-$direction) but were approximated by one large part. To simulate this shape, for every layer two cylindrical bodies were used creating very thin on the $z-$direction, but thick on the $R-$direction, hollow cylinders. The design details are in table 5.37.

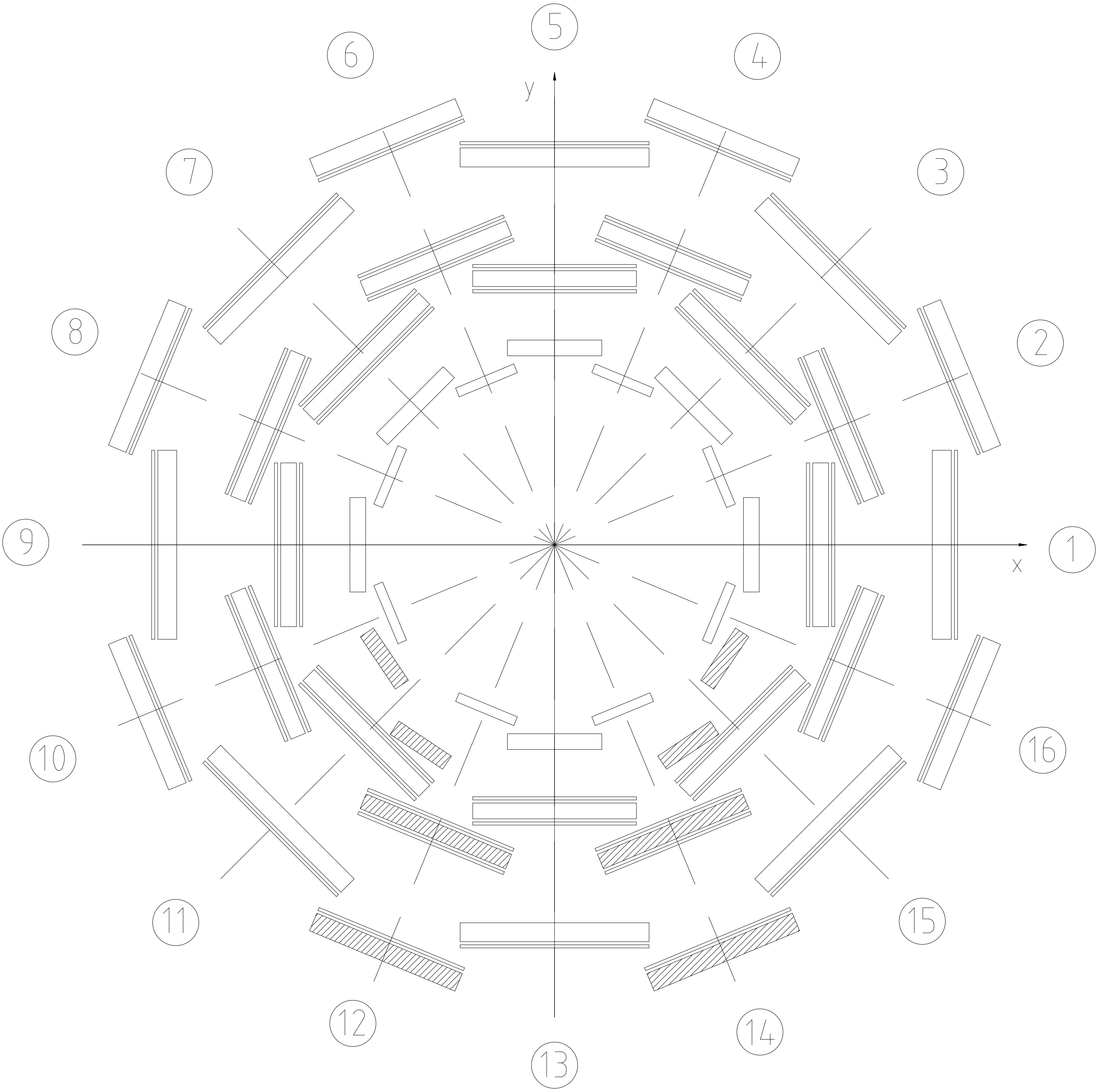

Figure 5.15: $x - y$ view of the barrel part of the Muon Spectrometer.

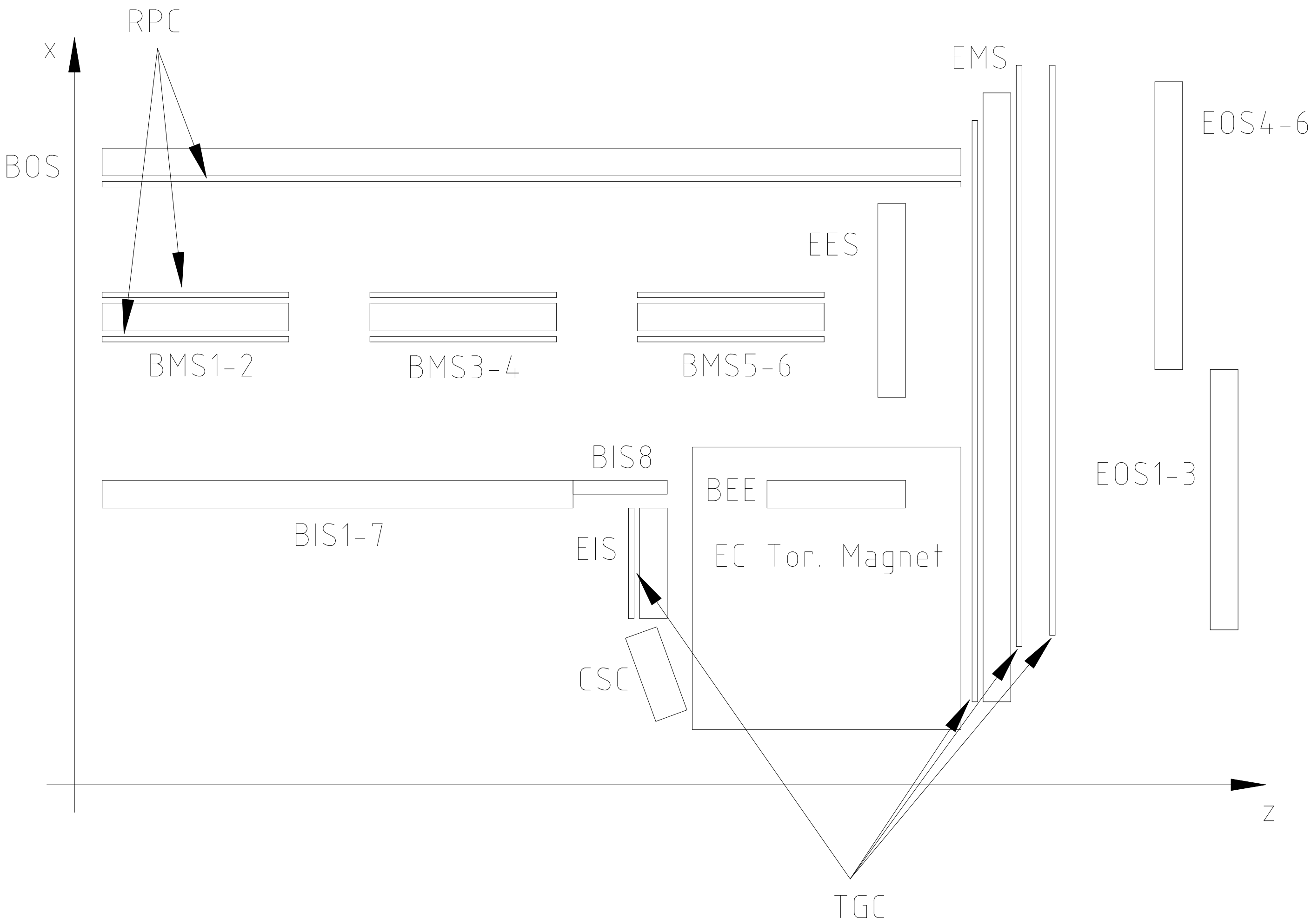

Figure 5.16: $x - z$ view of the small sectors of the Muon Spectrometer.

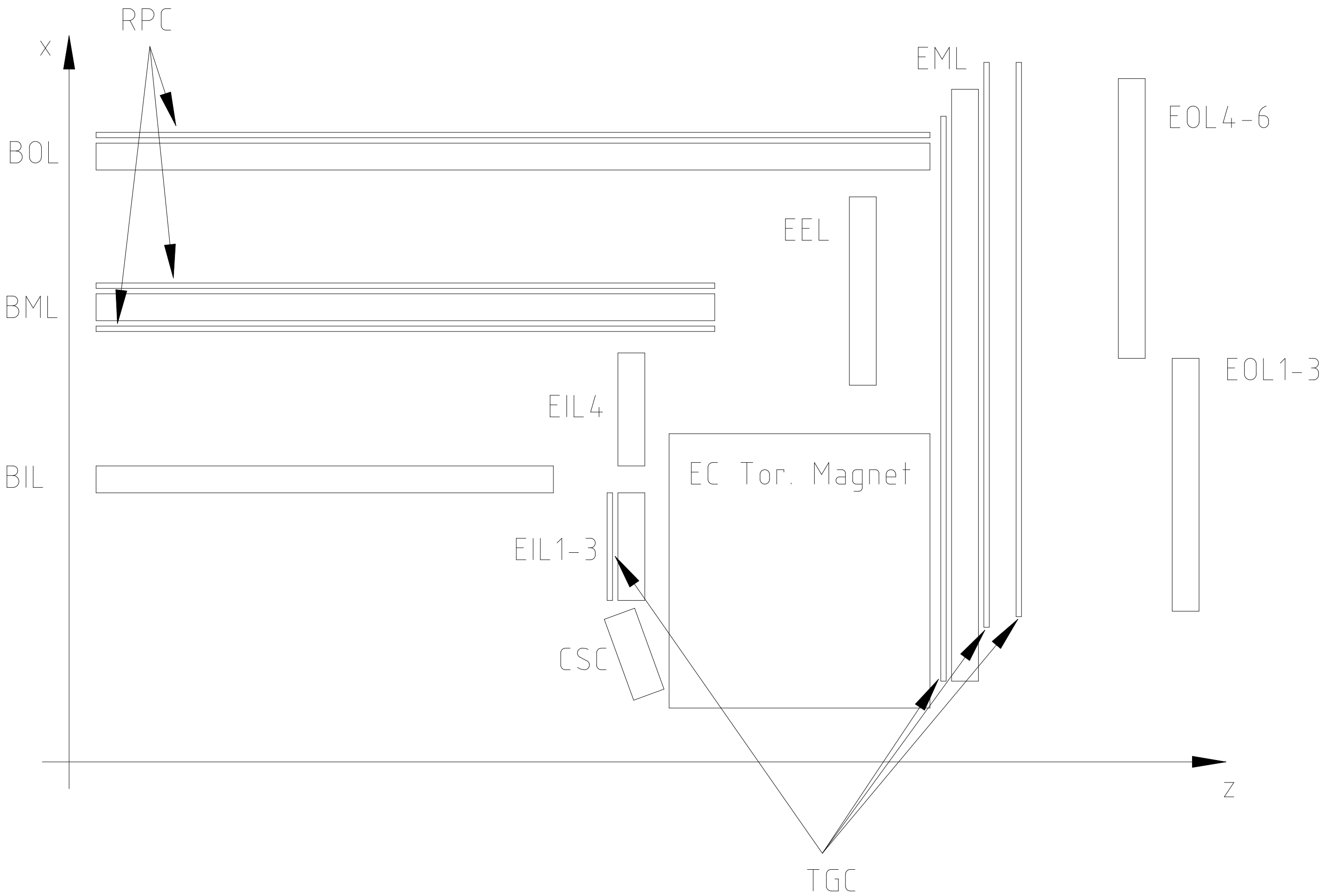

Figure 5.17: $x - z$ view of the large sectors of the Muon Spectrometer.

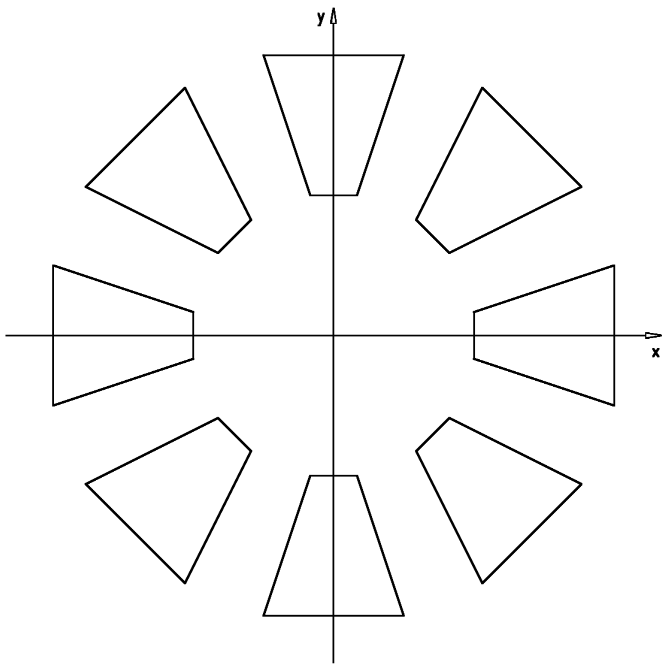

Figure 5.18: $x - y$ view of a standard end cap section of the Muon Spectrometer.

Part	R_i	R_o	Thickness (z)	$\|z\|$-position
Disk	13.8	98.2	5.0	349.0-354.0
Tube	14.0	18.0	96.0	354.0-450.0
Plug	7.5	18.0	8.0	450.0-458.0

Table 5.38: JM shield details.

5.5 Shielding

The simulation design of the shielding part follows figures 3.6-3.11, with very few simpifications.

5.5.1 The Moderator Shield - JM shield

The moderator shield has three parts on each side of the interaction point. At smaller $|z|$ is the disk, followed by a tube and then a plug, all made of polyboron. For the simulation design RCC and PLA bodies were used. The details for the JM shield are in the table 5.38.

5.5.2 Calorimeter Shielding Plugs

Behind the calorimeter system there are three copper plugs on each side of the interaction point, so there is a total of six plugs. The plugs on the left side are a

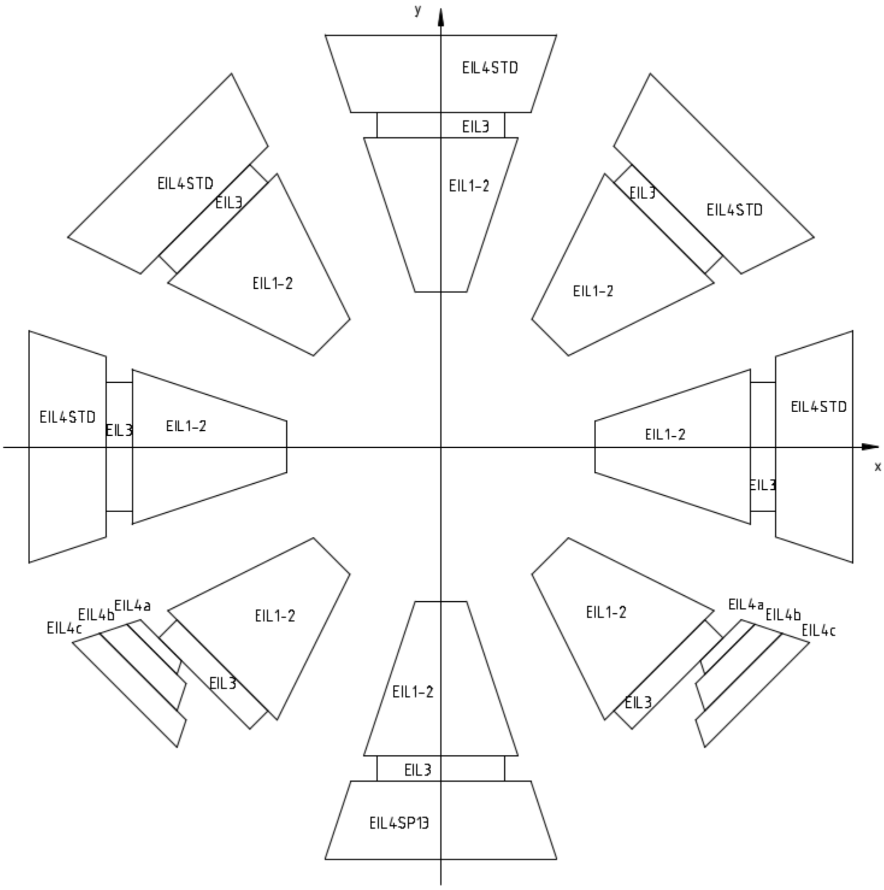

Figure 5.19: $x - y$ view of Inner Large end cap section of the Muon Spectrometer that includes special modules.

Part	R_i	R_o	Length (z)	$\|z\|$−position
Plug 1 cone	59.0	120.0-193.5	12.0	631.5-643.5
Plug 1 cylinder	50.0	208.9	5.0	643.5-648.5
Plug 2	47.5	67.5	13.0	616.2-629.2
Plug 3	9.74	44.87	44.24	612.48-656.72

Table 5.39: Calorimeter shielding plugs details.

Part	R_i	R_o	Length (z)	$\|z\|$−position
Disk	42.8	423.0	13.0	675.5-688.5
Tube	42.8	52.8	180.0	688.5-868.8
Tube plug	12.85-16.52	42.8	193.0	675.5-868.5
Cone conic part	52.8	125.1-76.37	17.5	688.5-706.0
Cone cylinder	52.8	76.37	8.0	706.0-714.0
Hub	52.8	76.0	73.0	714.0-787.0

Table 5.40: Details for the design of the JD-shield.

Part	R_i	R_o	Length (z)	$\|z\|$-position
Central Bore Tube	87.25	91.25	497.4	789.6-1287.0
Brass Plug	Table 5.42	82.25	494.4	789.6-1284.0
Additional Plug	24.48	86.25	8.0	1287.0-1295.0
JTV front ring	91.5	140.5	16.0	798.5-814.5
JTV back ring	91.5	129.5	8.0	1267.5-1275.5
JTV back wall	91.5	350.0	8.0	1283.0-1291.0
JTV front wall	152.5	350.0	8.0	803.5-811.5

Table 5.41: JT shield details.

$\|z\|$-position	R_i	Length (z)
789.6-869.1	55.15	79.5
869.1-1261.0	16.53-24.48	391.9
1261.0-1284.0	58.21	23.0

Table 5.42: Description of the complex shape of the inner surface of the JTT brass-plug. The second row indicates a conical shape and the base and apex radii are given.

Core Part	R_i	R_o	Length (z)	$\|z\|$-position
1^{st} **and** 2^{nd}	24.64-35.39	147.0 (1^{st}) 199.0 (2^{nd})	565.0	1295.0-1860.0
3^{rd}	150.0	199.0	200.0	1860.0-2100.0

Table 5.43: JF shield details.

Part	R_i	R_o	Length (z)	$\|z\|$-position
Monobloc	46.0	148.5	223.0	1862.0-2085.0
TAS col.	3.0	25.0	180.0	1905.0-2085.0
Washer	150.5	261.0	200.0	2100.0-2300.0
Support tube	127.5	147.5	2700.0	2300.0-5000.0
Concrete structure 1^{st} **part**	147.5	360.0	100.0	2300.0-2400.0
2^{nd} **part**	147.5	1200.0	1600.0	2400.0-3000.0

Table 5.44: JN shield details.

R_i	R_o	Length (z)	Face position (z)
1200.0	2000.0	6000.0	-3000.0

Table 5.45: Cavern details.

mirrored copy of those on the right side. Plug 1 starts of with conical shape that after a point continues as a cylinder. Plugs 2 and 3 a hollow cylinders. Details for the design of all three plugs in table 5.39.

5.5.3 Disk Shielding - JD Shield

The JD-shield consists of five parts. First the JD-disk, which is a disk made of steel. The JD-tube follows, a hollow cylinder made of stainless steel, inside of which a copper plug of conic shape is placed. The inner border of the plug is on the surface defined by pseudorapidity $\eta = \pm 4.65$. Below the CSC chambers are the cone and the hub, the hub has cylindrical shape, while the cone, as indicated by its name, conic followed by a thin cylindrical part. They are both made of copper and have two layers of cladding, the lower being polyethylene of $5cm$ thickness for the cone and $7cm$ thickness for the hub and the top one lead of $3cm$ thickness for both the cone and the hub. Details for the design of the disk shielding in table 5.40.

5.5.4 Toroid Shielding

The shielding of end-cap toroid region can be divided in five parts:

1. Stainless steel central bore tube, that has the shape of a hollow cylinder. Te inside surface of the bore tube is covered by a$5cm$ polyethylene cladding layer.

2. A brass plug (JTT brassplug) and an additional plug inside the bore tube. The brass plug is cylindrical on the outside, but has a more complex shape in the inside, it starts as s cylinder continues as a cone and then the last part is a cylinder again. The conic part of the inner surface is along pseudorapidity $\eta = \pm 4.65$. The additional plug is a hollow cylinder.

3. Two rings, with different dimensions, made of borated polyethylene, one on the front and one on the back side of the end-cap toroid. (JTV rings)

4. A disk on the back of the end-cap toroid (JTV back wall), that is made of polyethylene doped with lithium.

5. A disk in front of the magnet (JTV front wall), that is made of borated polyethylene.

The design is described in tables 5.41 and 5.42.

5.5.5 Forward Shield - JF shield

The forward shield starts at the back of the end-cap toroid and continues even after the beginning of the JN shield, surrounding th JN monobloc. It has a ductile iron core of cylindrical outer shape but conical inside. The inner conic surface is defined to be along pseudorapidity $\eta = \pm 4.65$. The outer radius of the core steps from $147.0cm$ at its the start (1^{st} part), to $199.0cm$ at distance $18.0m$ (2^{nd} part) from the interaction point. Then at $18.6m$ the inner radius gets constant and equal to $150.0cm$ (3^{rd} part). The core is surrounded by two layers of cladding, the thickness of which changes at distance $18.0m$ from the interaction point. A $5cm$ thick borated polyethylene layer followed by a $3cm$ thick steel layer surrounds the 1^{st} part core and then the borated polyethylene layer is $8cm$, while the steel layer is $3cm$ thick for the 2^{nd} and 3^{rd} parts. Design details for the core in table 5.43.

5.5.6 Nose Shielding - JN shield

The nose shield can be divides into five parts. The JN monobloc has cylindrical shape and is made of ductile iron. In the monobloc is the copper TAS collimator, which also has cylindrical shape. Then the shield continues with a large ductile iron disk, washer, followed by a steel support tube that is surrounded by a thick concrete structure. Details for the design of this part of the shield in table 5.44.

5.5.7 Cavern

The ATLAS cavern was simulated as a hollow cylinder made of concrete. The dimensions are given in table 5.45.

5.6 Toroid Magnets

The ATLAS toroid magnet system is composed of three magnets, one barrel and two end-cap toroids. Each magnet consists of eight coils arranged azimuthally as indicated in table 5.46 and shown in figure 5.20.

5.6.1 Barrel Toroid

The barrel toroid has eight coils arranged around the beam axis. The design details for one coil are in table 5.48. The simulation design for the 8-coil bunch uses:

- Four cylinders, two of them defining the inner and outer radii of the magnet and the other two defining the R-thickness of each coil.

	Azimuthal Position (degrees)
End-Cap Toroid	0
	45
	90
	135
	180
	225
	270
	315
Barrel Toroid	22.5
	67.5
	112.5
	157.5
	202.5
	247.5
	292.5
	337.5

Table 5.46: Azimuthal position of the barrel and end-cap toroid coils.

Length (z)	$\|z\|-$position	z-thickness	R_i	R_o	$R-$thickness	$\phi-$thickness
452.0	815.0-1267.0	40.0	107.5	535.0	40.0	26.8

Table 5.47: End-cap toroid design details for one coil.

Length (z)	$z-$position	z-thickness	R_i	R_o	$R-$thickness	$\phi-$thickness
2530.0	-12.65.0-1265.0	38.6	470.0	1005.0	38.6	28.8

Table 5.48: Barrel toroid design details for one coil.

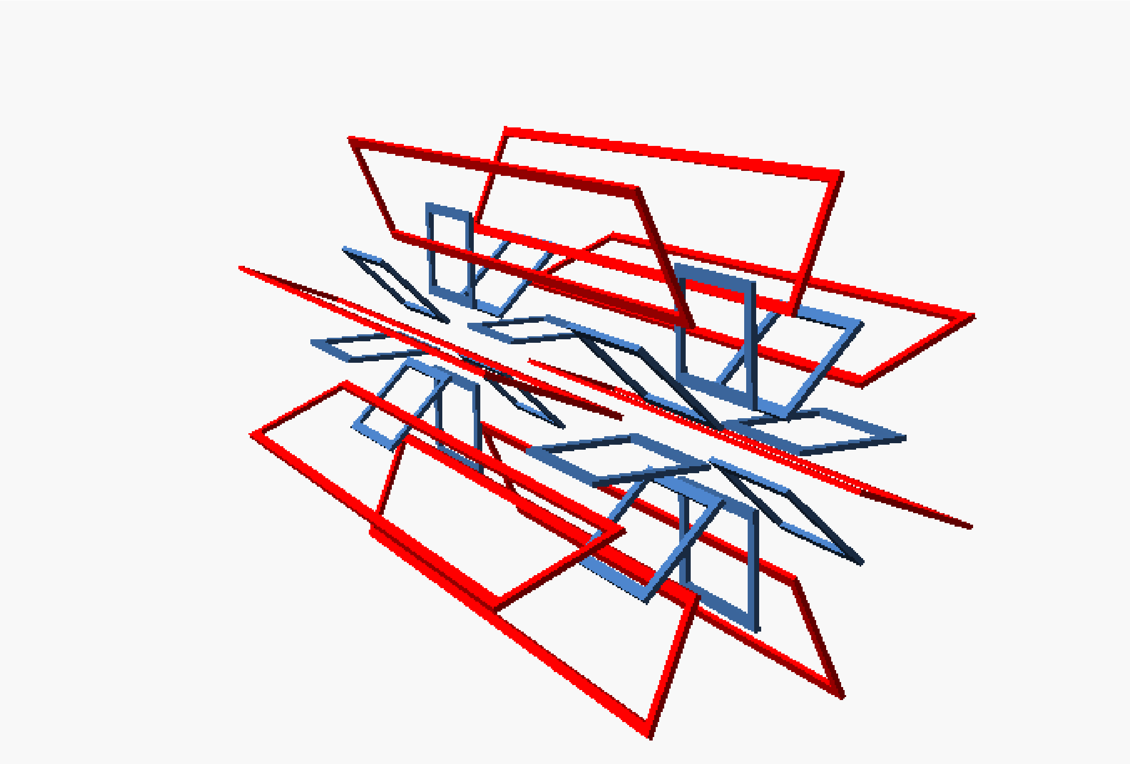

Figure 5.20: $3D$ figure of the toroid magnet layout.

- Two planes, parallel to z=0 plane, defining the z-thickness.
- Two planes, for each coil, that define the $\phi-$thickness. Beacuse of the symmetric arrangment of the coils only 8 palnes were needed.

5.6.2 End-Cap Toroids

There are two end-cap toroids, one on each side (left, right) of the interaction point. Each magnet has 8 coils arranged symmetricaly around the ATLAS beam line. The design details for one coil are in table 5.47. The rest of the coils are identical but rotated around $z-$axis. Each 8-coil bunch was designed using the same principles as for the barrel toroid.

5.7 The proton beams

The BEAM and SPECSOUR cards were used for the beam definitions. Two proton beams, each with $7TeV$ momentum collide at the I.P. with $285\mu rad$ crossing angle ($142.5\mu rad$ half crossing angle).

5.8 Scoring

USRBIN cards were used to measure photon and neutron fluences in a quarter of the detector.

Chapter 6

Simulation Results

6.1 Background Radiation Impact and Estimators

Particle interactions at very high energies result in large quantities of radiation emission. A big part of this radiation may be ionizing and give rise to multiple issues, such as

- Wear and aging of the detector's materials and electronics
- Distortion on the data signals
- Personnel safety issues

Close to I.P. the backgrounds are dominated by particles from the p-p collisions and at higher radii by neutrons from high energy hadron cascades in the calorimeters

Simulating the ATLAS experiment conditions helps estimate the background radiation levels and limit the negative effects. A general picture of the radiation background can be obtained by studying particle fluences and fluxes at several points in the detector. For this thesis photon and neutron fluences were measured at a quadrant of the detector with a binning of approximately $3cm$.

It is worth noting that increasing the beam luminosity and/or its energy will lead to higher particle fluences and thus higher levels of background radiation.

6.2 Background Radiation Prediction from the Developed FLUKA Simulation

The simulation results for particle fluence are expressed in $\frac{particles}{cm^2}$ per primary weight, which translates to $\frac{particles}{cm^2}$ per p-p collision. To obtain fluence rates ($\frac{particles}{cm^2}$ per second), the results were normalized with the event rate. Assuming a luminosity $L = 10^{34}cm^{-2}s^{-1}$ and a proton inelastic interaction cross section $\sigma_{inel.} = 60.3mb$, leads to an event rate of $N = L \cdot \sigma_{inel.} = 60.3 \times 10^7 \frac{p-p\ collisions}{s}$.

The I.D. region is the closest one to the interaction point, so high particle fluence rates are expected. The neutrons in this region come either directly from the proton interactions at the I.P. and the beam pipe material or are a result of back-splash from the calorimeter surfaces. This can be observed in the neutron fluence rate map of figure 6.1 where it is obvious that at the end-cap calorimeter region the fluence rates rise by a factor of 10 of the logarithmic scale. It is also worth noting that the JM-shield prevents these back-splash neutrons from entering the I.D. region, thus offering effective neutron moderation. Neutrons with high energy, while interacting with the beam pipe and inner detector materials cause high energy photon emission. In this region the photon fluence rates, shown in figure 6.2 are mainly due to particle interactions with the beampipe and I.D. materials and π^0 decay.

An increase in rates appears at the calorimeter region which can be explained by the initiation of hadronic and electromagnetic showers in the detectors. After that the rates drop at the CSC regions as well as in the middle and outer MDT end-cap regions.

Both figures 6.3 and 6.4 show that in the concrete cavern, neutron and photon fluence rates drop at very low levels, which indicates the effectiveness of this particular part of the shielding.

Comparing the simulation results with those of [2], given in figures 6.5-6.8 one can observe two things. Firstly the contours of fluence rates are very close, which indicates similar behaviour for the simulation design of this thesis and [2]. Another important remark is the big difference in the fluence rate levels, in logarithmic scale there is a ratio of 10 between the results produced in the two simulations. This may be due various reasons such higher beam momentum and luminosity and/or different interaction cross sections.

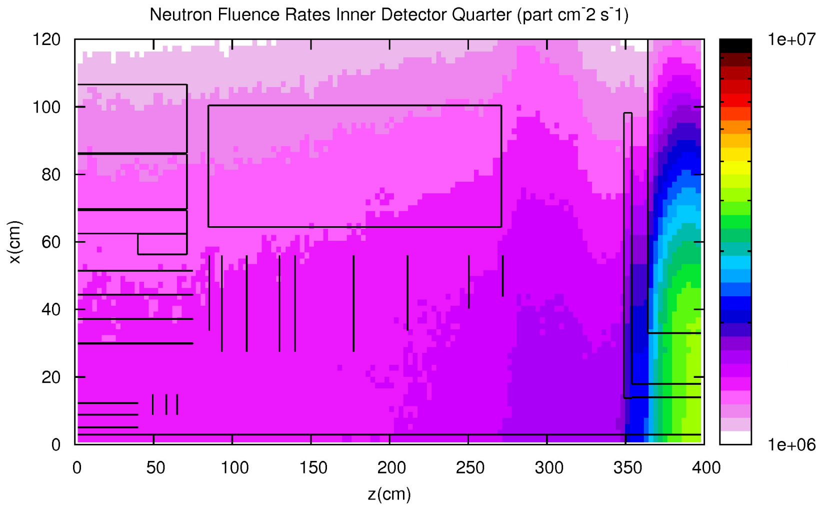

Figure 6.1: Neutron fluence rates map for the Inner Detector region.

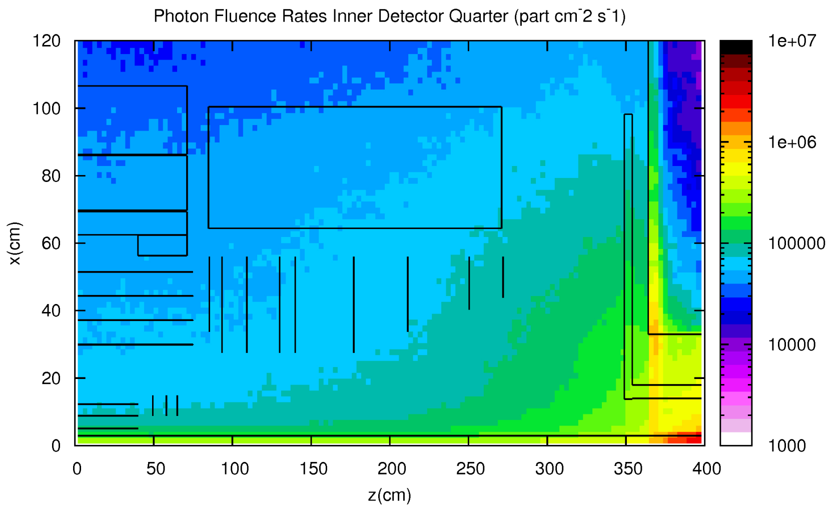

Figure 6.2: Photon fluence rates map for the Inner Detector region.

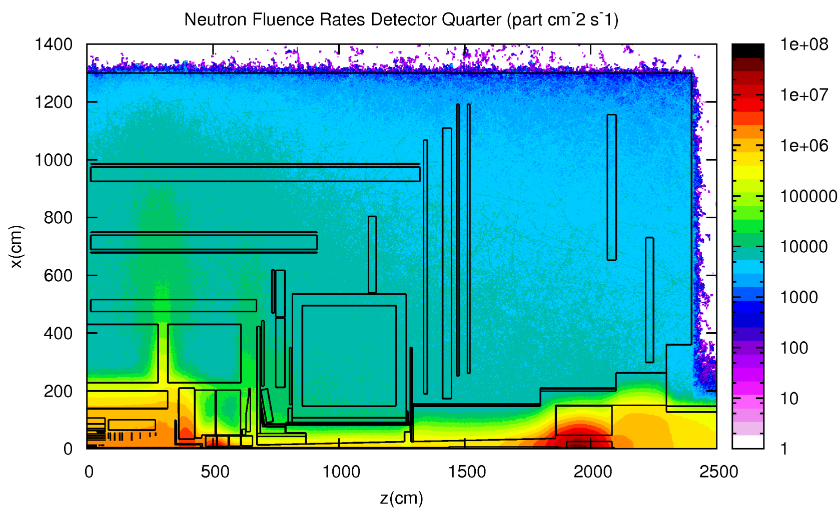

Figure 6.3: Neutron fluence rates map for a quarter if the total detector geometry.

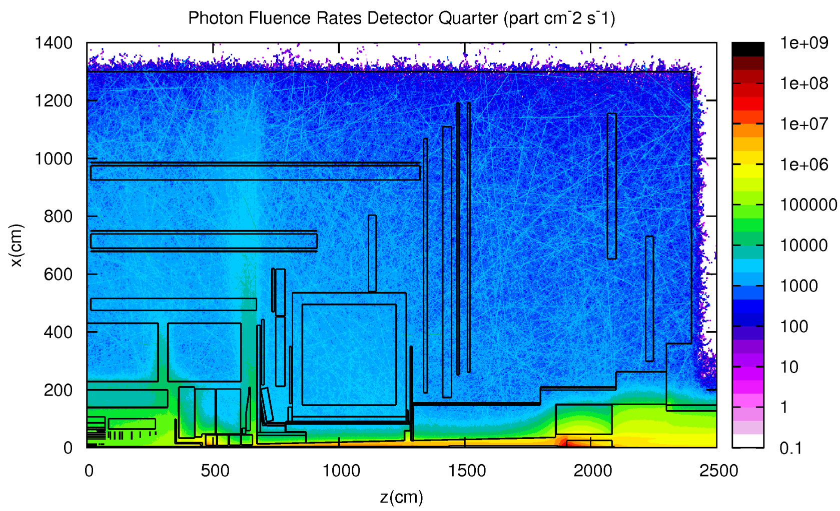

Figure 6.4: Photon fluence rates map for a quarter if the total detector geometry.

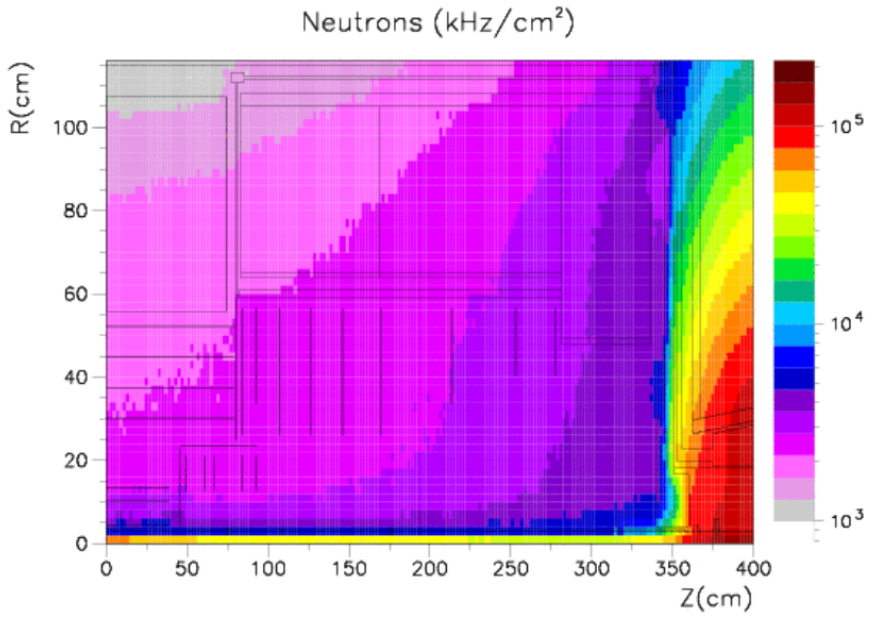

Figure 6.5: Neutron fluence rates map for the Inner Detector region. [2]

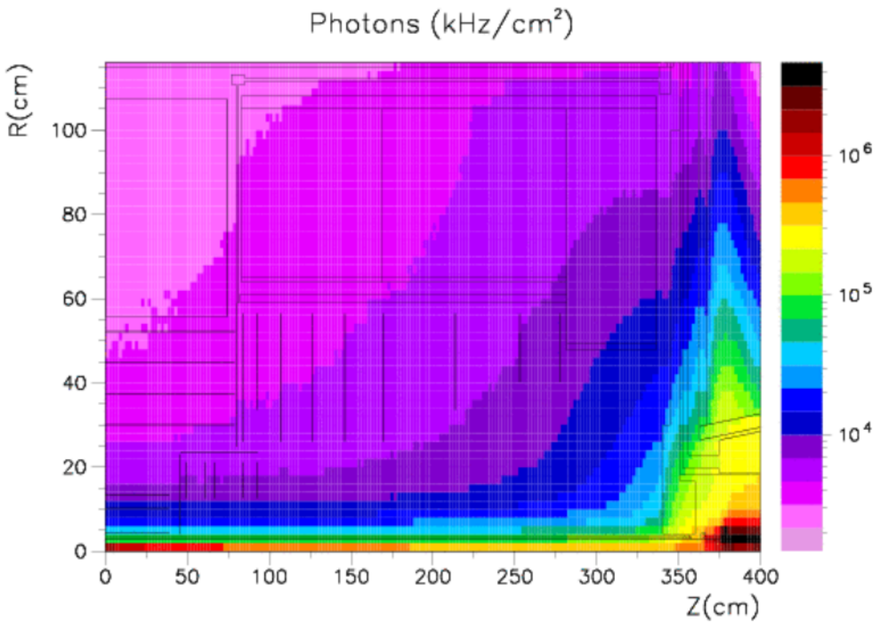

Figure 6.6: Photon fluence rates map for the Inner Detector region. [2]

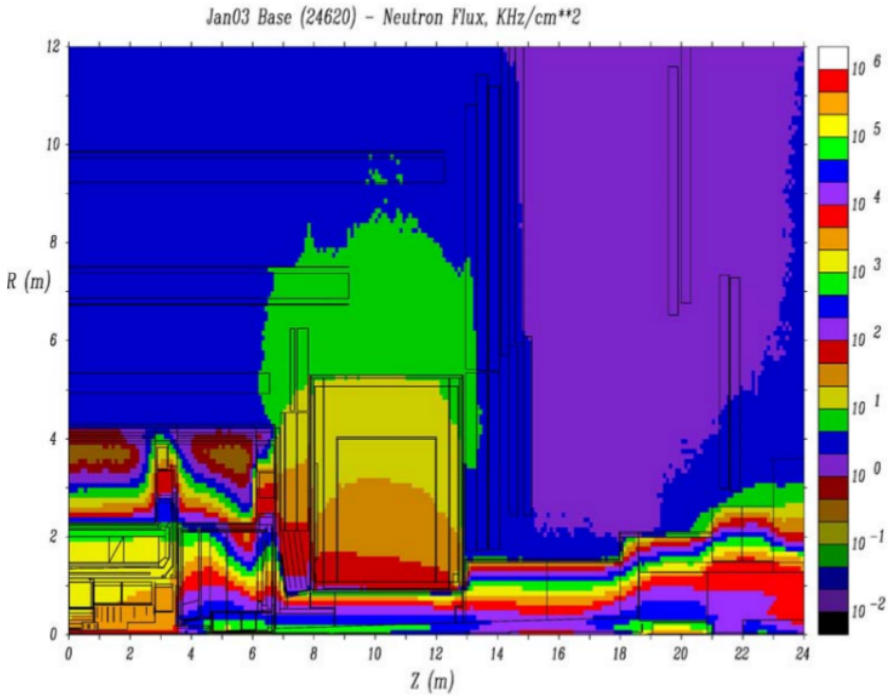

Figure 6.7: Neutron fluence rates map for a quarter if the total detector geometry. [2]

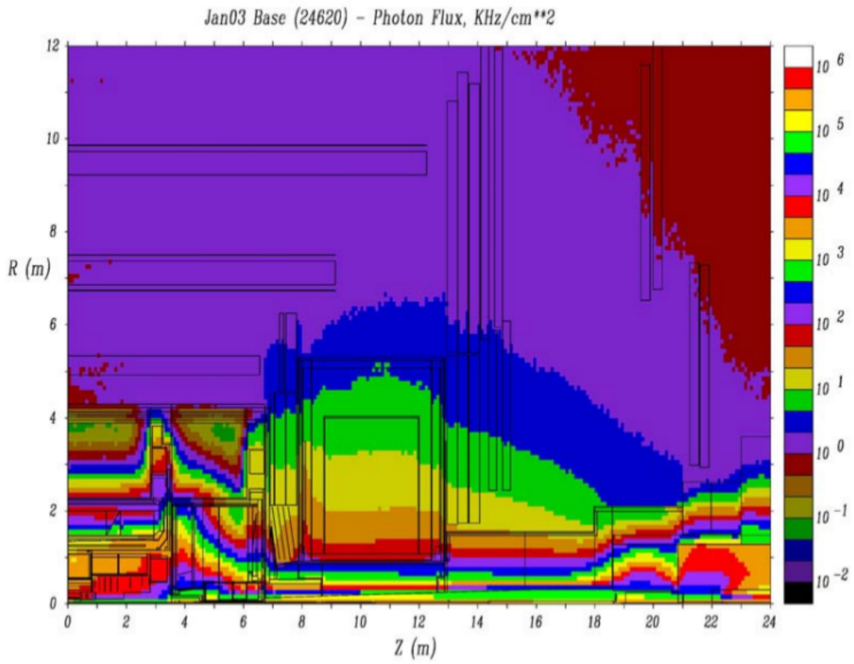

Figure 6.8: Photon fluence rates map for a quarter if the total detector geometry. [2]

Chapter 7

Conclusion

The results obtained from the simulation have the expected form. In order to get better more accurate predictions and a more spherical view of the radiation background:

- use of additional estimators, such as charged hadron fluences, dose and particle energy spectrums
- simulation runs with smaller bins and/or more primaries
- increase of the geometry design and material description accuracy and replacement of older modules with new ones where necessary

are proposed.

Appendix I

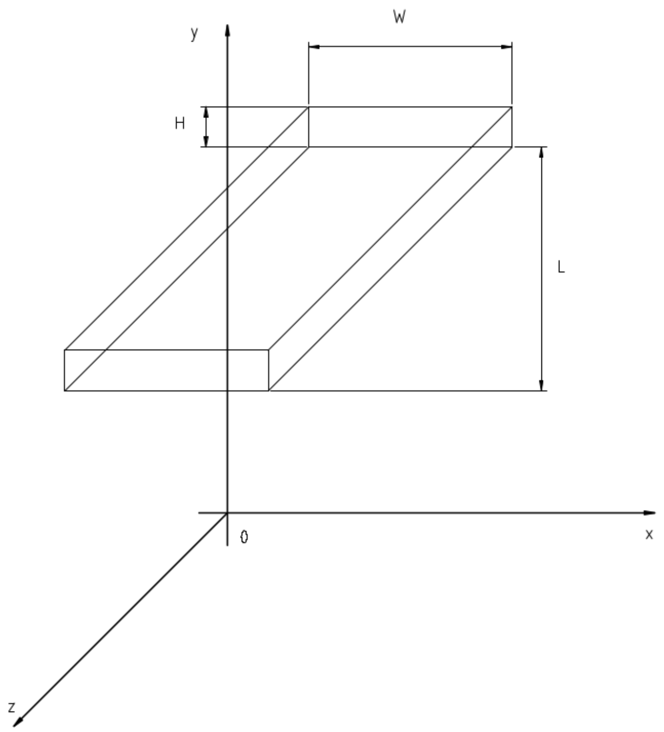

Figure 7.1: Rectangular parallelepiped design.

Assume a orthogonal parallelepiped with:

- 2 sides parallel to plane $x = 0$
- 2 sides parallel to plane $y = 0$
- 2 sides parallel to plane $z = 0$

as shown in figure 7.1. The design the MDT barrel chambers for the different sectors dictates that 2 sides are always parallel to the plane $z = 0$ and these two sides for all sectors of the same module type are on the same plane. So for modules of the same type two planes are needed, instead of sixteen. These two have normal vectors $\mathbf{n} = [0, 0, 1]^T$ and have a distance of L, the length of the module. The front plane includes the point $A_1(0, 0, z_f)$ and the back plane the point $A_2(0, 0, z_f + L)$, where z_f the position of the face of the module.

The rest of the planes needed to define the parallelepiped are a little more complicated in their parameter calculations. The position of a module in the desired sectors can be obtained by rotating it around the z-axis. Rotation of such a parallelepiped around z-axis changes the normal vectors of all planes but the two parallel to $z = 0$. So for simplicity the calculations can be performed in 2-dimensions and are accurate in 3-dimensions as well. The xy-plane views before and after the rotation can be seen in 7.2a and 7.2b respectively. The module is positioned in the necessary radial distance from the "Interaction Point", the origin of the coordinate system, R_i and its width, W is centred on the $x-$axis. Planes (represented by lines in the 2-D projection) 1 and 3 are parallel to $y = 0$ so their normal vector is $\boldsymbol{n_1} = [0, 1, 0]^T$, which becomes $\boldsymbol{n_1} = [0, 1]^T$ in 2-D and planes 2 and 4 are parallel to $x = 0$ with normal vector $\boldsymbol{n_2} = [1, 0, 0]^T$, which becomes $\boldsymbol{n_1} = [1, 0]^T$ in 2-D. The vertices $B(R_i, {}^W\!/\!_2)$ and $C(R_o, -{}^W\!/\!_2)$ are used for defining planes 1,4 and 2,3 respectfully. The rectangle in figure 7.2b is that one in 7.2a rotated counterclockwise about the origin through an angle θ, so the rotation matrix is,

$$R = \begin{bmatrix} cos(\theta) & -sin(\theta) \\ sin(\theta) & cos(\theta) \end{bmatrix}$$

The rotated vectors are:

- $\boldsymbol{n'_1} = R \cdot \boldsymbol{n_1} = [-sin\theta, cos\theta]^T$
- $\boldsymbol{n'_2} = R \cdot \boldsymbol{n_2} = [cos\theta, sin\theta]^T$
- $\boldsymbol{B'} = R \cdot \boldsymbol{B} = \left[-\frac{W}{2}sin\theta + R_i cos\theta, \frac{W}{2}cos\theta + R_i sin\theta\right]^T$
- $\boldsymbol{C'} = R \cdot \boldsymbol{C} = \left[\frac{W}{2}sin\theta + R_o cos\theta, -\frac{W}{2}cos\theta + R_o sin\theta\right]^T$

In three dimensions the z-coordinate does not change with the rotation, so:

- $\boldsymbol{n'_1} = R \cdot \boldsymbol{n_1} = [-sin\theta, cos\theta, 0]^T$
- $\boldsymbol{n'_2} = R \cdot \boldsymbol{n_2} = [cos\theta, sin\theta, 0]^T$
- $\boldsymbol{B'} = R \cdot \boldsymbol{B} = \left[-\frac{W}{2}sin\theta + R_i cos\theta, \frac{W}{2}cos\theta + R_i sin\theta, z_f\right]^T$
- $\boldsymbol{C'} = R \cdot \boldsymbol{C} = \left[\frac{W}{2}sin\theta + R_o cos\theta, -\frac{W}{2}cos\theta + R_o sin\theta, z_f\right]^T$

where z_f is desired position in z.

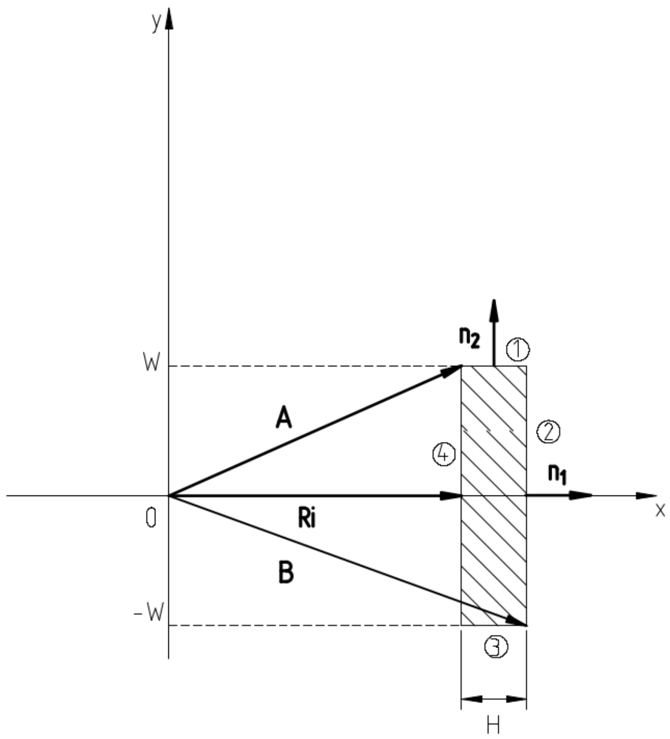

(a) x-y view of rectangular parallelepiped before rotation around z-axis.

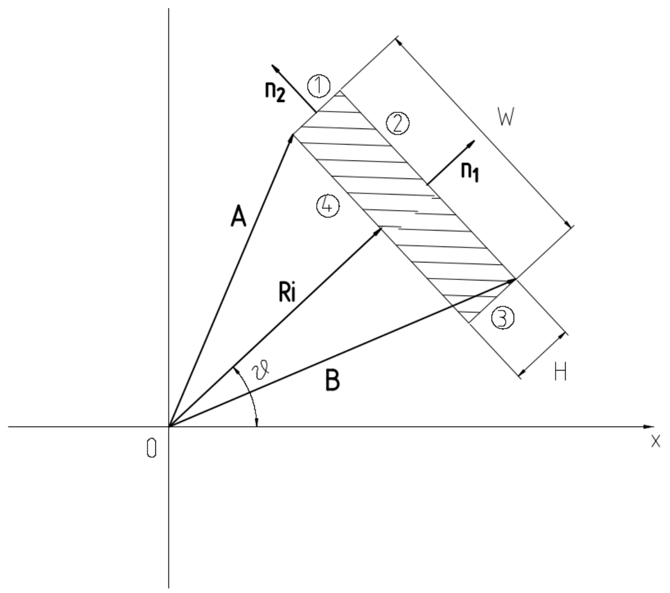

(b) x-y view of rectangular parallelepiped after rotation around z-axis.

Figure 7.2: Before and after the rotation.

Appendix II

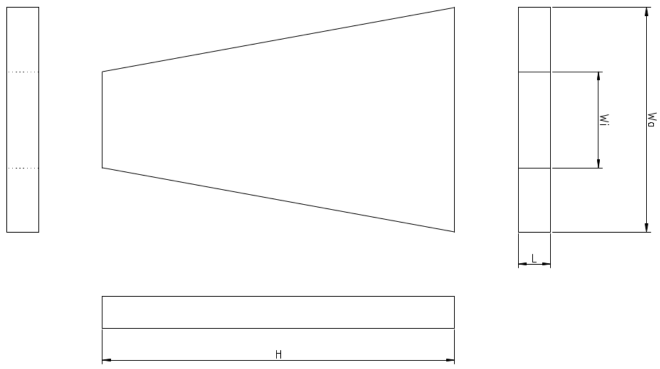

Figure 7.3: Simple mechanical design of a standard MDT end cap module as simulated.

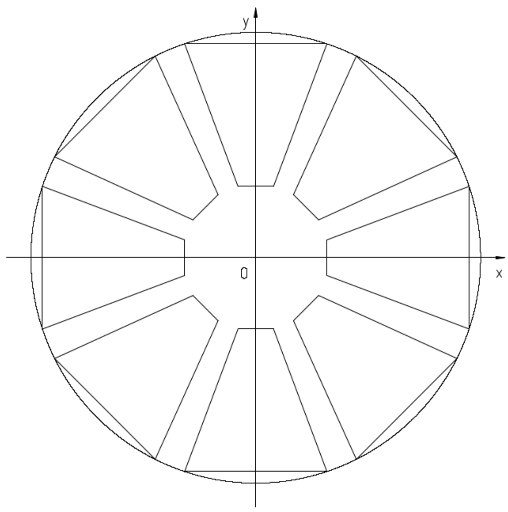

Figure 7.4: Example of MDT end cap module layout.

All modules in an end cap region, with a few exceptions, have the same design and position on the $z-$axis and along the radial dimension. The only thing that changes is that modules belonging to different sectors have different azimuthal positions. An example of the layout of an end cap region is in figure **??**. In this figure one can see

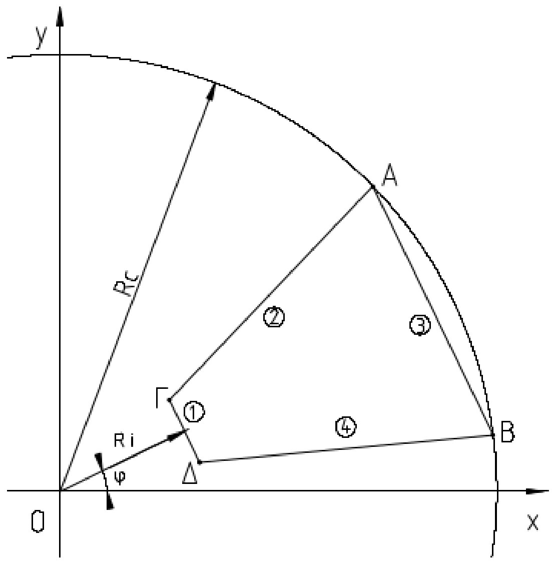

Figure 7.5: Projection on the $z = 0$ plane of an MDT end cap module at azimuthal position ϕ.

that it is enough to design only one module and then calculate all desired parameters with respect to the rotation angle. Then for each angle, some simple calculations give the design parameters. Also all modules are "contained" by a circle in this 2-D figure , which in reality is a cylinder of radius R_c.

The basic module is designed as shown in figure **??** and placed at the correct radial position but at random azimuthal, figure REF. For the two parallel to $z = 0$ faces of the end caps, the faces of a cylinder with $z-$dimension equal to the E.C. length are used. The rest of the planar sides are defined by planes "cutting" the cylinder. To define each plane a normal vector and a point are needed. To simplify the calculations the projection of a module at the $z = 0$ plane is used, as seen in figure **??**.

The cylinder radius is the distance of the farthest point of the module projection from the axis origin. These points are A and B. Since $AB = W_o$ and $\Gamma\Delta = W_i$:

- $A(x_A, y_A) = \left(R_o cos\phi - \frac{W_o}{2} sin\phi, R_o sin\phi + \frac{W_o}{2} cos\phi\right)$
- $B(x_B, y_B) = \left(R_o cos\phi + \frac{W_o}{2} sin\phi, R_o sin\phi - \frac{W_o}{2} cos\phi\right)$
- $\Gamma(x_\Gamma, y_\Gamma) = \left(R_i cos\phi + \frac{W_i}{2} sin\phi, R_i sin\phi - \frac{W_i}{2} cos\phi\right)$
- $\Delta(x_\Delta, y_\Delta) = \left(R_i cos\phi - \frac{W_i}{2} sin\phi, R_i sin\phi + \frac{W_i}{2} cos\phi\right)$

so $R_c = \sqrt{R_o^2 + \frac{W_o^2}{4}}$.

A unit normal vector to planes 1 and 3 is $\hat{n}_{13} = (cos\phi, sin\phi)$. For planes 2 and 4 normal unit vectors are those that are perpendicular to $\boldsymbol{\Delta A}$ and $\boldsymbol{\Gamma B}$ respectively.

$$\boldsymbol{\Delta A} = \big((R_o - R_i)cos\phi - \tfrac{1}{2}(W_o - W_i)sin\phi, (R_o - R_i)sin\phi + \tfrac{1}{2}(W_o - W_i)cos\phi\big) \implies |\boldsymbol{\Delta A}| = \sqrt{(R_o - R_i)^2 + \tfrac{1}{4}(W_o - W_i)^2}$$

The unit vector parallel to $\boldsymbol{\Delta A}$ is $\hat{\boldsymbol{\Delta A}} = \frac{\boldsymbol{\Delta A}}{|\boldsymbol{\Delta A}|} = (x_2, y_2)$, so the unit normal vector to plane 2 is $\hat{n}_2 = (-y_2, x_2)$, x_2 and y_2 can be calculated from the equations above for each ϕ.

Following the same process for the normal vector to plane 4, $\hat{n}_4$:

$$\boldsymbol{\Gamma B} = \big((R_o - R_i)cos\phi + \tfrac{1}{2}(W_o - W_i)sin\phi, (R_o - R_i)sin\phi - \tfrac{1}{2}(W_o - W_i)cos\phi\big) \implies |\boldsymbol{\Gamma B}| = \sqrt{(R_o - R_i)^2 + \tfrac{1}{4}(W_o - W_i)^2}$$

The unit vector parallel to $\boldsymbol{\Gamma B}$ is $\hat{\boldsymbol{\Gamma B}} = \frac{\boldsymbol{\Gamma B}}{|\boldsymbol{\Gamma B}|} = (x_4, y_4)$, so $\hat{n}_4 = (-y_4, x_4)$, x_4 and y_4 can be calculated from the equations above for each ϕ.

Summarizing the parameters needed for each plane:

- Plane 1: $\hat{n}_{13}$ and point Γ
- Plane 2: $\hat{n}_2$ and point A
- Plane 3: $\hat{n}_{13}$ and point A
- Plane 4: $\hat{n}_4$ and point Γ

Appendix III

As stated in chapter RefToCh6 there are two types of C.S. Chambers and a CSC region contains 8 modules of each type arranged in 16 sectors around the beam axis. A rough schematic is shown in figure RefFig, this figure can be used only as assistance for understanding the layout around the axis but in reality it is a layout of the module projections on a plane parallel to $z = 0$, in reality the module positioning is more complex and described subsequently in this appendix.

For the design a process similar to that of MDT EC design was followed, as the modules have the same shape, the difference is that CSC modules are tilted an have no sides parallel to $z = 0$ plane. In order to implement the $|\omega| = 11.9^o$ tilt angle the following process was developed.

1^{st} Step: Initialization

Suppose the prismoid module centred around the axis' origin and placed at azimuthal position $\theta = 0^o$ as shown in figure RefFig. For each type the parameters change but the process is exactly the same. The polyhedron has eight vertices and six sides. The position of each vertex in the cartesian coordinate system is:

- $\mathbf{A_1} = \begin{bmatrix} \frac{R_e}{2} & \frac{W_o}{2} & f & 1 \end{bmatrix}^T$ [1]
- $\mathbf{A_2} = \begin{bmatrix} \frac{R_e}{2} & \frac{W_o}{2} & -f & 1 \end{bmatrix}^T$
- $\mathbf{B_1} = \begin{bmatrix} \frac{R_e}{2} & -\frac{W_o}{2} & f & 1 \end{bmatrix}^T$
- $\mathbf{B_2} = \begin{bmatrix} \frac{R_e}{2} & -\frac{W_o}{2} & -f & 1 \end{bmatrix}^T$
- $\mathbf{C_1} = \begin{bmatrix} -\frac{R_e}{2} & -\frac{W_i}{2} & f & 1 \end{bmatrix}^T$
- $\mathbf{C_2} = \begin{bmatrix} -\frac{R_e}{2} & -\frac{W_i}{2} & -f & 1 \end{bmatrix}^T$
- $\mathbf{D_1} = \begin{bmatrix} -\frac{R_e}{2} & \frac{W_i}{2} & f & 1 \end{bmatrix}^T$

[1] The "1" at the end of the vectors are used for multiplication with the 4×4 translation and rotation matrices that define position transformation in the 3-D space.

* $\mathbf{D_2} = \begin{bmatrix} -\frac{R_e}{2} & \frac{W_i}{2} & -f & 1 \end{bmatrix}^T$

The parameters are defined as follows, R_e is the radial extension of a module, W_i is the the inner width, the smaller width of the module, W_o is the outer width, the larger width of the module and f is the thickness of a module, in the simulation each part has $2f$ thickness because in reality two modules are placed back to back at each sector.

After this step the result is 8 vertex positions.

<u>2^{nd} Step: 1^{st} Rotation, around $y-$axis for tilted modules</u>

The desired tilt angle is $\omega = 11.9^o$. Modules placed at positive z values (referred to as right modules and indicated with an R subscript) rotate around the $y-$axis by ω degrees and modules placed at negative z values (referred to as left modules and indicated with an L subscript) rotate around the $y-$axis by $-\omega$ degrees.

The rotation matrices are:

* $R_{1R} = \begin{bmatrix} cos\omega & 0 & sin\omega & 0 \\ 0 & 1 & 0 & 0 \\ -sin\omega & 0 & cos\omega & 0 \\ 0 & 0 & 0 & 1 \end{bmatrix}$

* $R_{1L} = \begin{bmatrix} cos\omega & 0 & -sin\omega & 0 \\ 0 & 1 & 0 & 0 \\ sin\omega & 0 & cos\omega & 0 \\ 0 & 0 & 0 & 1 \end{bmatrix}$

The azimuthal position of the modules is still $\theta = 0^o$. After this step the result is 16 vertex positions, 8 for a module that will be placed at positive z values and 8 for a module that will be placed at negative z values.

<u>3^{rd} Step: 1^{st} Translation, along $x-$axis</u>

The modules are translated and placed at the x position of the $\theta = 0^o$ sector. If R_o is the desired radial position of the vertex farthest from the $x = 0$ plane and x_2 its value after the second step, the translation matrix is:

$$T_{1x} = \begin{bmatrix} 1 & 0 & 0 & R_o - x_2 \\ 0 & 1 & 0 & 0 \\ 0 & 0 & 1 & 0 \\ 0 & 0 & 0 & 1 \end{bmatrix}$$

The azimuthal position of the modules is still $\theta = 0^o$. After this step the result is 16 vertex positions, 8 for a module that will be placed at positive z values and 8 for a module that will be placed at negative z values.

<u>4^{th} Step: 2^{nd} Translation, along $z-$axis</u>

The modules are translated and placed at the z position of the $\theta = 0^o$ sector. If z_d

is the desired position of the vertex closest to the $z = 0$ plane and z_3 its value after the third step, the translation matrix is:

$$T_{2z} = \begin{bmatrix} 1 & 0 & 0 & 0 \\ 0 & 1 & 0 & 0 \\ 0 & 0 & 1 & z_d - z_3 \\ 0 & 0 & 0 & 1 \end{bmatrix}$$

The azimuthal position of the modules is still $\theta = 0^o$. After this step the result is 16 vertex positions, 8 for a module that placed at positive z values and 8 for a module that placed at negative z values.

<u>5^{th} Step: 2^{nd} Rotation, around $z - axis$ for 16 sectors on each side</u>

Change in the azimuthal position of the module by rotating around the $z-$axis by θ, places it at its final position. This step is repeated 8 times for each side (positive z and negative z) and 8 times for each type of module, each time starting at $\theta = 0^o$ (which means that each time the resulting vertices from the fourth step are rotated). If θ is the desired azimuthal position of current the sector, the rotation matrix is:

$$R_{2z} = \begin{bmatrix} cos\theta & -sin\theta & 0 & 0 \\ sin\theta & cos\theta & 0 & 0 \\ 0 & 0 & 1 & 0 \\ 0 & 0 & 0 & 1 \end{bmatrix}$$

After each iteration the result is 16 vertex positions, 8 for a module that placed at positive z values and 8 for a module that placed at negative z values. So by the end of the repeating loop the output is the position of 256 vertices, that by 8 they define one module.

After finding the positions of the vertices of a module in order to design it in the simulation one must define six planes, one for each side of the module. For each plane one point and a unit normal, to the plane vector is needed.

- Vector $\mathbf{n_1} = \mathbf{D_1A_1} \times \mathbf{D_1D_2}$ is normal to plane 1.
- Vector $\mathbf{n_2} = \mathbf{C_1B_1} \times \mathbf{C_1C_2}$ is normal to plane 2.
- Vector $\mathbf{n_3} = \mathbf{A_1A_2} \times \mathbf{A_1B_1}$ is normal to plane 3.
- Vector $\mathbf{n_4} = \mathbf{D_1D_2} \times \mathbf{D_1C_1}$ is normal to plane 4.
- Vector $\mathbf{n_5} = \mathbf{A_2D_2} \times \mathbf{A_2B_2}$ is normal to plane 5.
- Vector $\mathbf{n_6} = \mathbf{D_1A_1} \times \mathbf{D_1C_1}$ is normal to plane 6.

The normal vectors can become unitary by using the relation $\widehat{\mathbf{n_i}} = \frac{\mathbf{n_i}}{|\mathbf{n_i}|}$. Summarizing the parameters needed for each plane:

- Plane 1: $\widehat{n}_1$ and point D_1
- Plane 2: $\widehat{n}_2$ and point C_1
- Plane 3: $\widehat{n}_3$ and point A_1
- Plane 4: $\widehat{n}_4$ and point D_1
- Plane 5: $\widehat{n}_5$ and point A_2
- Plane 6: $\widehat{n}_6$ and point D_1

Appendix IV

Some figures of the detector geometry from the flair editor follow.

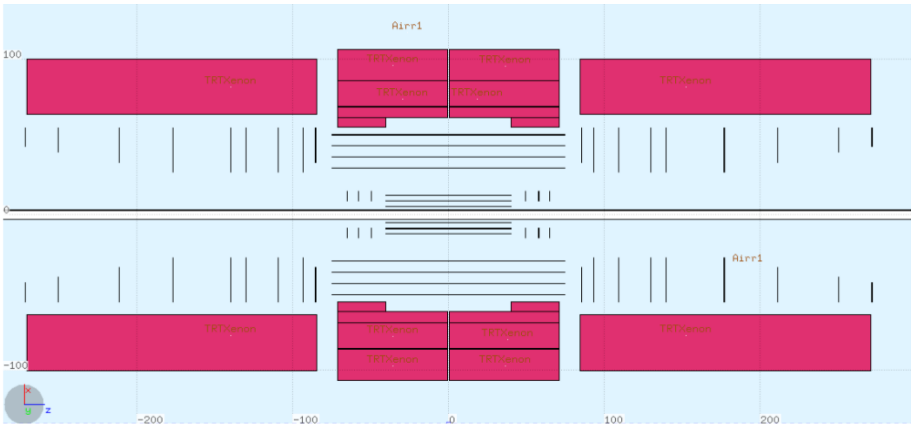

Figure 7.6: $x-z$ view of the inner detector.

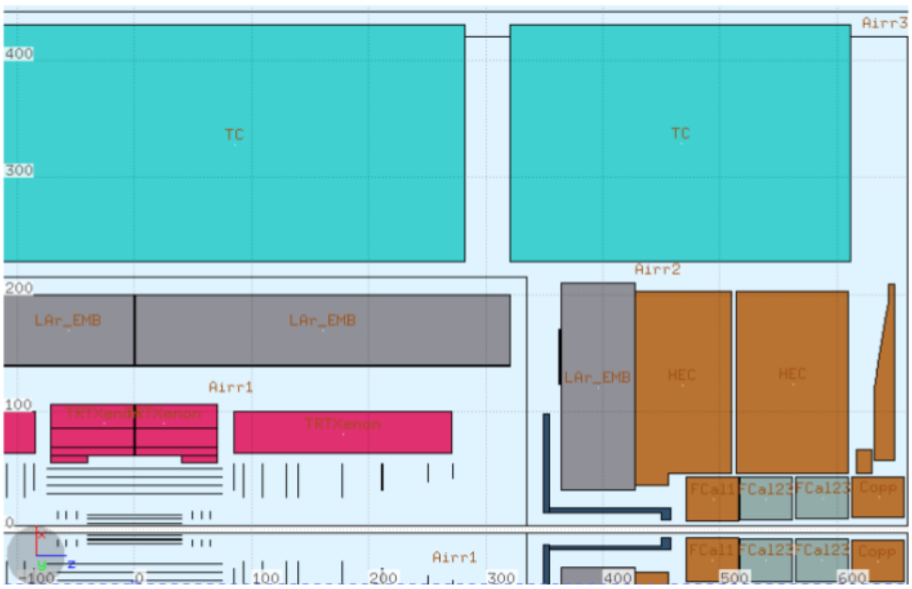

Figure 7.7: $x-z$ view of a quarter of the calorimetry system.

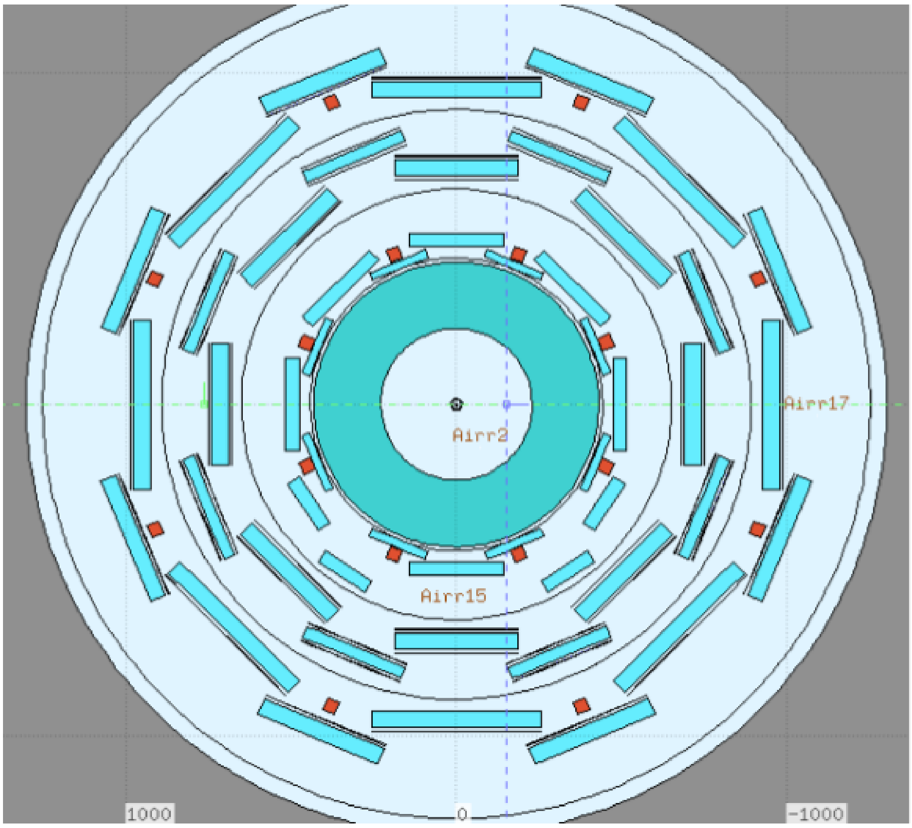

Figure 7.8: $x - y$ view of the barrel barrel part of the muon spectrometer.

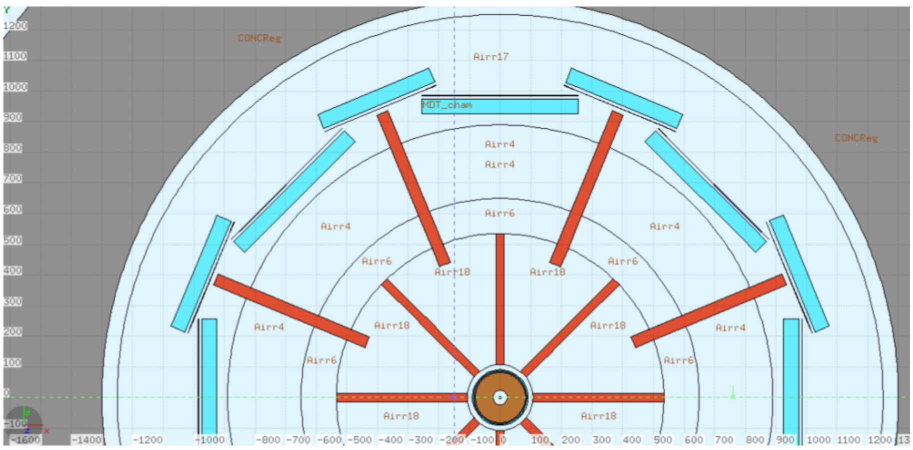

Figure 7.9: $x - y$ view of a half of the toroid magnet system.

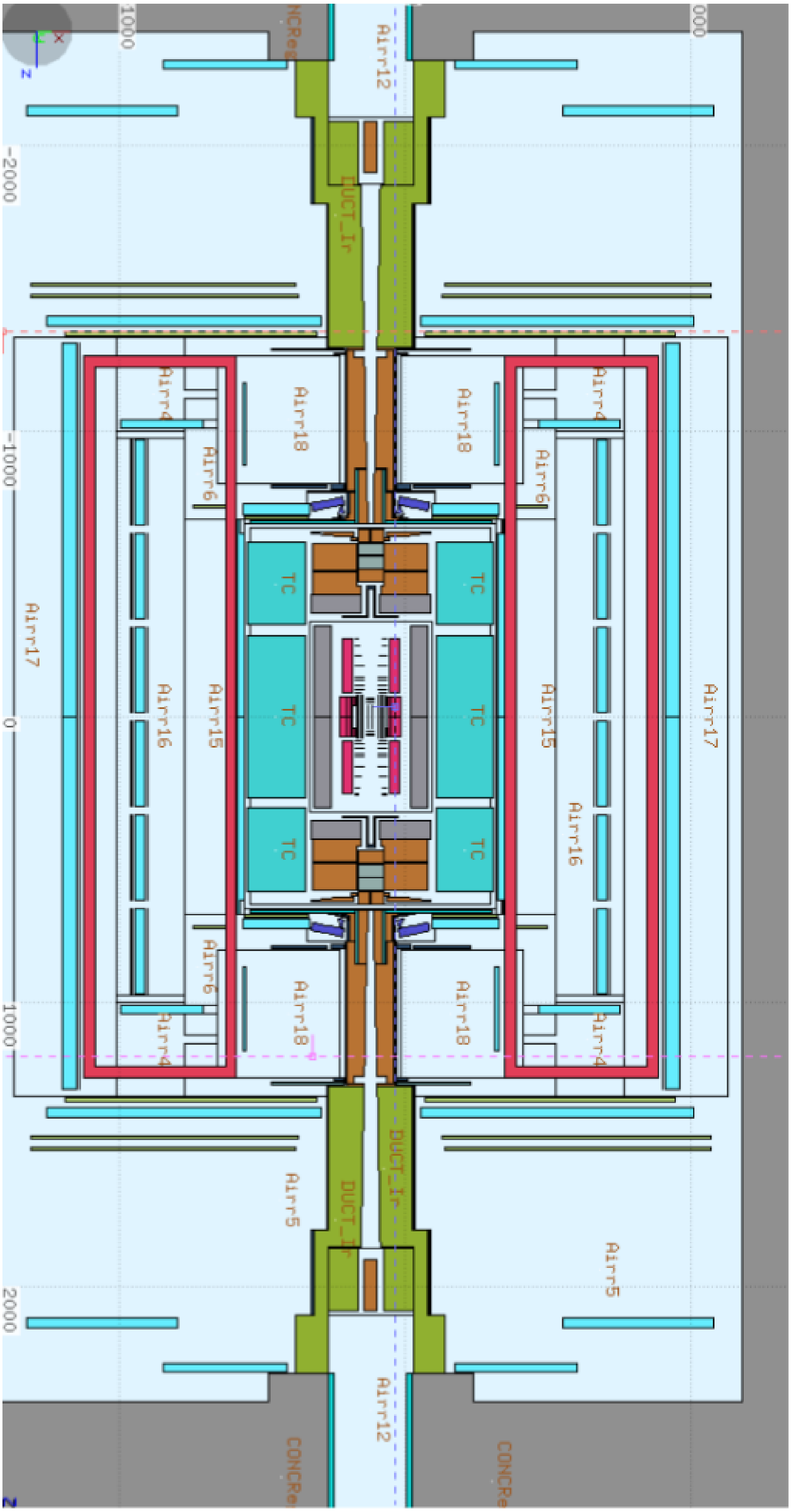

Figure 7.10: $x-z$ view of the entire detector.

Bibliography

[1] The ATLAS Collaboration. *Measurement of the inelastic proton-proton cross section at* $\sqrt{s} = 7TeV$ *with the ATLAS detector.*

[2] S.Baranov, M.Bosman, I.Dawson, V.Hedberg, A.Nisati and M.Shupe. *Estimation of Radiation Background, Impact on Detectors, Activation and Shielding Optimization in ATLAS*. ATL-GEN-2005-001 13 Jan. 2005.

[3] The ATLAS Collaboration *The ATLAS Experiment at the CERN Large Hadron Collider*. JINST 2008.

[4] The ATLAS Collaboration *ATLAS Inner Detector Technical Design Report Volume I.*

[5] The ATLAS Collaboration *ATLAS Liquid Argon Calorimeter Technical Design Report.*

[6] The ATLAS Collaboration *ATLAS Tile Calorimeter Technical Design Report.*

[7] The ATLAS Collaboration *ATLAS Muon Spectrometer Technical Design Report.*

[8] The ATLAS Collaboration *ATLAS Barrel Toroid Technical Design Report.*

[9] The ATLAS Collaboration *ATLAS End-cap Toroid Technical Design Report.*

[10] Stefaan Tavernier. *Experimental Techniques in Nuclear and Particle Physics*. Springer.

[11] Claus Grupen and Boris Shwartz. *Particle Detectors*. Cambridge Monographs on Particle Physics, Nuclear Physics and Cosmology.

[12] Brian R. Martin. *Nuclear and Particle Physics An Introduction*. Wiley.

[13] B. R. Martin and G. Shaw. *Particle Physics*. Wiley.

[14] Samuel S.M. Wong. *Introductory Nuclear Physics*. Wiley-VCH.

[15] Kenneth S. Krane. *Introductory Nuclear Physics*. Wiley.

[16] David Griffiths. *Introduction to Elementary Particles*. Wiley-VCH.

[17] Raymond A. Serway, Clement J. Moses and Curt A. Moyer. *Σύγχρονη Φυσική*. Πανεπιστημιακές Εκδόσεις Κρήτης.

[18] Ευάγγελος Ν. Γαζής. *Σύγχρονη Πειραματική Φυσική*. Εκδόσεις Συμμετρία.

[19] Thomas G. McCarthy. *Measurement of the Top Quark Mass in the All-Hadronic Top-Antitop Decay Channel Using Proton-Proton Collision Data from the ATLAS Experiment at a Centre-of-Mass Energy of 8 TeV*. Doctor of Science Thesis.

[20] T. S. Virdee *Physics requirements for the design of the ATLAS and CMS experiments at the Large Hadron Collider*. Imperial College London, London SW7 2BZ, UK

[21] CERN's Accelerator Complex Image:
`https://cds.cern.ch/record/1621583`

[22] Detector Image:
`http://cdsweb.cern.ch/record/1095924`

[23] Inner Detector Image:
`https://cds.cern.ch/images/CERN-GE-0803014-01`

[24] Calorimeters Image:
`http://cdsweb.cern.ch/record/1095927`

[25] Muon Spectrometer Image:
`http://cdsweb.cern.ch/record/1095929`

[26] ATLAS shielding:
`http://atlas.web.cern.ch/Atlas/GROUPS/Shielding/shielding.htm`

[27] N. Metropolis and S. Ulam *The Monte Carlo Method*. Journal of the American Statistical Association, Vol. 44, No. 247. (Sep. 1949), pp. 335-341.

[28] A. Ferrari, P. R. Sala, A. Fasso, J. Ranft *Fluka: a multi-particle transport code*. CERN European Organization for Nuclear Research, Geneva 2011.

[29] The accelerator complex:
`http://cds.cern.ch/record/1997193`, Jan. 2012.

[30] The Large Hadron Collider,
`http://cds.cern.ch/record/1998498`, Jan. 2014.

[31] Cian O'Luanaigh, *Heavy metal: Refilling the lead source for the LHC*, http://cds.cern.ch/record/1997797, Feb. 2013.

[32] How a detector works, http://cds.cern.ch/record/1997219, Jan. 2012.

[33] Xabier Cid Vidal, Ramon Cid Manzano, *Taking a closer look at LHC*, http://www.lhc-closer.es/taking_a_closer_look_at_lhc/1.home